University of Southampton

Faculty of Environmental and Life Sciences

Ocean and Earth Science

Multi-Proxy Investigations into Mediterranean Outflow Water Variability and Sedimentary Processes on the West Iberian Margin Through the Late Pleistocene

by

Matthew David Nichols

ORCID ID 0000-0001-7219-4594

Thesis for the degree of Doctor of Philosophy

December 2020

University of Southampton

Abstract

Faculty of Environmental and Life Sciences

Ocean and Earth Science

Doctor of Philosophy

Multi-Proxy Investigations into Mediterranean Outflow Water Variability and Sedimentary Processes on the West Iberian Margin Through the Late Pleistocene

by

Matthew David Nichols

Mediterranean Outflow Water (MOW) adds salt and density to open ocean intermediate waters and is therefore an important motor of Atlantic meridional overturning circulation (AMOC) and climate variability. However, the variability in strength and depth of MOW on geological timescales is poorly documented. West Iberian Margin sediments provide important reference records in palaeoceanographic studies, climate events in the marine realm recorded here can be correlated to both the Antarctic and Greenland ice cores as well as to European terrestrial records. These sediments, therefore, provide an opportunity to document MOW variability in high-resolution, underpinned by strong age control.

Here, I present new detailed records, with excellent age control, of MOW variability from ~416 ka to present from rapidly accumulated marine sediments recovered from the West Iberian Margin during Integrated Ocean Drilling Program (IODP) Expedition 339. The records of X-ray fluorescence (XRF), physical grain size, and paleocurrent information from the anisotropy of magnetic susceptibility (AMS) indicate (i) a close relationship between the orientation of principle AMS axes and glacial-interglacial cycles and (ii) two distinct regimes of MOW behaviour over the last ~416 kyr in grain-size and AMS variability at orbital (mainly precession) and suborbital timescales. It is inferred that late Pleistocene variability in MOW strength and depth were strongly climate influenced and that changes in circum-Mediterranean rainfall climate were likely a primary control.

A suite of environmental and rock magnetic records from IODP Site U1391 sediments are presented. Different forms of magnetite with varying grain size are inferred as being the dominant magnetic phase in the sediments. From ~130 ka to present, the grain size and concentration of magnetite were strongly controlled by northern high latitude variability. During some stadials in this interval an additional high coercivity component is present, possibly representing haematite derived from North African dust. In sediments older than ~130 ka, evidence of reductive diagenesis is seen across environmental and rock magnetic proxies, and is particularly strong in sediments deposited during marine isotope stages (MIS) 9 and 11. These

conditions likely result from a combination of increased productivity and changes in sedimentation rates, associated with vertical migration of the Mediterranean outflow water.

XRF (i.e., ln(Zr/Rb)) and magnetic grain size (i.e., κ_{ARM}/κ) proxy records from IODP Site U1391 sediments are identified as best representing different physical size fractions of sediment, 33 – 43 μm and 8 – 19 μm (and likely sizes below 5 μm), respectively. Utilising the high-resolution grain size records as proxy of MOW strength in combination with strong chronology; frequency and phasing analysis uncover the relative importance of different climate forcings on MOW. Evidence suggests that spring insolation forcing of MOW strength variability at Site U1391 between ~370 and 60 ka, likely linked with intensification of late-winter North Atlantic storm track activity at precession minima. There is also evidence that this mechanism is impacted upon by the interference of meltwater pulses with North Atlantic circulation.

Table of Contents

Table of Tables

Table of Figures

Research Thesis: Declaration of Authorship

Print name: Matthew David Nichols

Title of thesis: Multi-Proxy Investigations into Mediterranean Outflow Water Variability and Sedimentary Processes on the West Iberian Margin Through the Late Pleistocene

I declare that this thesis and the work presented in it are my own and has been generated by me as the result of my own original research.

I confirm that:

1. This work was done wholly or mainly while in candidature for a research degree at this University;
2. Where any part of this thesis has previously been submitted for a degree or any other qualification at this University or any other institution, this has been clearly stated;
3. Where I have consulted the published work of others, this is always clearly attributed;
4. Where I have quoted from the work of others, the source is always given. With the exception of such quotations, this thesis is entirely my own work;
5. I have acknowledged all main sources of help;
6. Where the thesis is based on work done by myself jointly with others, I have made clear exactly what was done by others and what I have contributed myself;
7. Parts of this work have been published as:

Nichols, M. D., Xuan, C., Crowhurst, S., Hodell, D. A., Richter, C., Acton, G. D., et al. (2020). Climate-induced variability in Mediterranean Outflow to the North Atlantic Ocean during the late Pleistocene. Paleoceanography and Paleoclimatology, 35, e2020PA003947. https://doi.org/10.1029/2020PA003947

Signature: ..... Date: .....

Declaration of Contributions

Chapter 2 was published in Paleoceanography and Paleoclimatology. All listed authors were involved in the discussion of scientific concepts and editing the manuscript. I conceptualised the study, took the majority of the bulk and cube samples, conducted the majority of measurements, data processing and analysis, and produced the figures. Chuang Xuan advised on data processing and quality control, and took some shipboard cube samples. Simon Crowhurst measured the U1385 XRF data and some of the U1391 grain size data.

For chapter 3 I measured the majority of u-channel environmental magnetic data, ~50% of the rock magnetic data, did the data processing, quality control, data analysis, produced the figures and wrote the manuscript. Deanna Vella (Masters Student) measured ~50% of rock magnetic data. Chuang Xuan provided the measurement protocols, discussion of data interpretation, and, alongside Paul Wilson, discussion of scientific concepts and manuscript editing.

For chapter 4 I conceptualised the study and phasing phenomenon, measured ~75% of the remaining grain size distributions, did the data analysis and figure creation, and wrote the manuscript. Simon Crowhurst measured ~25% of the remaining grain size distributions and measured the SS% data. Chuang Xuan advised on data and phasing analysis and, alongside Paul Wilson, was involved in discussion of scientific concepts and manuscript editing.

Acknowledgements

Firstly, I would like to thank Chuang. He has always been friendly, approachable, supportive and knowledgeable. He has given me many hours of his time to explain concepts, discuss ideas, debug code, and give detailed feedback, for which I am very grateful. I hope we can have more games of badminton and pub trips in the future.

I want to thank Paul for all of his guidance, vital insight, and valuable feedback throughout the PhD. He always asked the searching questions to put me on the right track.

I would like to thank Yuxi for teaching me how to do all the magnetic measurements, for always smiling and being helpful in the lab.

I want to thank Simon for providing tremendous amounts of help with the grain size work, giving insight and advice into numerous topics, and, not least, for putting up with a lot of emails. I really appreciated his support.

I am very grateful for the help of many others through the course of my PhD. In particular I would like to thank Tim, for palaeomagnetic and PhD advice, and football-pizza evenings along the way; Sarge, for the jokes and anecdotes, and for help with the grain size sample preparation process (keeping it much more fun than it had any right to be); BOSCORF staff, for help and advice with collecting the XRF data; Deanna and Martin for collecting some rock magnetic and XRF data, respectively.

I am grateful to my office-mates, Vicki, Max and Gwen (i.e., Synergy) in 164/16, for keeping the work-days fun, decorating the office, their general support and numerous useful science discussions.

To all my other friends that I made at the start and through the course of PhD, you have made my years in Southampton enjoyable. There are too many to name here, but in particular Rach, Amy J, Duncan, Koko, Ben C, Alex T, Sarah H, Amy E, David R and Tereza.

My housemate Joe lived with me for the best part of 4 years in Southampton. Thanks for keeping me running, and providing excellent beer and board game suggestions.

The final thank you is for my family, Mum, Dad, Susie (+ Ross and Sophie), and Amy for giving so much encouragement and support over the years

Definitions and Abbreviations

AF ..... Alternating Field

AMOC..... Atlantic meridional overturning circulation

AMS..... Anisotropy of Magnetic Susceptibility

ARM ..... Anhysteretic Remnant Magnetisation

CCSF ..... Core composite depth below sea floor

CWT..... Continuous wavelet transform

DC..... Direct current

ENACWsp ..... Eastern North Atlantic Central Water sub-polar

ENACWst..... Eastern North Atlantic Central Water sub-tropical

FORC ..... First-order reversal curve

IODP ..... Integrated Ocean Drilling Program (2003-2013) or International Ocean Discovery Program (2013-present)

IRM..... Isothermal Remnant Magnetisation

ITCZ ..... Inter tropical convergence zone

κ..... Magnetic susceptibility

Ka ..... Kilo annum (thousand years ago)

Kyr..... Period of a thousand years

LIW..... Levantine Intermediate Water

Ma..... Mega annum (million years ago)

MD ..... Multi domain

MOW..... Mediterranean Outflow Water

NADW ..... North Atlantic Deep Water

NRM ..... Natural Remnant Magnetisation

ODP ..... Ocean Drilling Program

PSD..... Pseudo-single domain

SD..... Single domain

SS ..... Sortable silt

SIRM..... Saturating isothermal remnant magnetisation

WTC ..... Wavelet Coherence

XRF ..... X-ray fluorescence

XWT..... Cross-wavelet transform

Chapter 1 Introduction

1.1 Thesis Summary

This thesis predominantly focusses on investigating the evolution of the Mediterranean outflow water (MOW) on the west Iberian Margin over the course of the last ~416 ka. Studies of the Mediterranean exchange with the Atlantic have largely only covered the last glacial-interglacial cycle due to availability of deep sediment archives. Therefore, questions remain concerning the nature of MOW variability in strength and depth in earlier glacial-interglacial cycles, the climatic causes and effects of this variability, and its effects on the sediments of the west Iberian Margin.

West Iberian Margin sediments are recognised as important reference sections in palaeoclimatic studies. In addition to MOW changes, environmental magnetic proxies allow for inferences regarding the presence of ice-rafted debris (IRD), Saharan dust, millennial scale variability, and redox changes in the context of Atlantic palaeoceanography.

1.1.1 Chapter 1: Introduction

This chapter provides the background information and context for the topics covered in this thesis. The research carried out here is based upon marine sediment samples and so in section 1.2 the background to ocean drilling and recovery of palaeoclimate archives is briefly described. I go on to discuss the palaeoclimatic significance and previous research conducted using materials from on the west Iberian Margin. In section 1.4 the modern state of the Mediterranean Outflow water (MOW) is described, followed by research covering its evolution through the Pliocene to the present day, before the relationship of MOW with North Atlantic circulation. Finally, I describe and explain the fundamentals of the techniques and proxies used in this research project.

1.1.2 Chapter 2: Climate-induced variability in Mediterranean Outflow to the North Atlantic Ocean during the late Pleistocene

In Chapter 2 a high-resolution chronology is constructed for Site U1391 sediments covering the last ~416 kyr, by correlation to Site U1385 and transfer of its well-established age model. The evolution of the MOW on the west Iberian Margin is then investigated through the application of environmental magnetic, x-ray fluorescence (XRF) and grain size proxies at Sites U1391 and U1385. Interpretation of these proxies leads to the presentation of multiple regimes of behaviour of the MOW.

A modified version of this chapter was published as Nichols, M. D., Xuan, C., Crowhurst, S., Hodell, D. A., Richter, C., Acton, G. D., Wilson, P. A. (2020). Climate-induced variability in Mediterranean Outflow to the North Atlantic Ocean during the late Pleistocene. Paleoceanography and Paleoclimatology, 35, e2020PA003947. https://doi.org/10.1029/2020PA003947

1.1.3 Chapter 3: Environmental Magnetic Investigations on West Iberian Margin Sediments: Provenance and Processes

This chapter presents the environmental and rock magnetic results of investigations into sedimentary processes on the west Iberian Margin. Varying forms and sizes of magnetite are found to be the dominant phases of remanence carriers. Theories of the causes of magnetic grain size variability on the west Iberian Margin are tested and built upon. Evidence of MOW related oxidation state changes are presented which manifest themselves in correlations between changes in magnetic minerology and x-ray fluorescence ratios. Additionally, this chapter also discusses around the source of haematite and identification of ice-rafted debris layers in west Iberian Margin sediments.

1.1.4 Chapter 4: Grain size variabilities in Pleistocene sediments from the west Iberian Margin: implications on climate processes

In this Chapter, I build upon the grain size investigations of the previous two chapters, introducing a higher resolution mean grain size record and sortable silt % data, and explore the range of physical grain sizes that the X-ray fluorescence and magnetic grain size proxies represent. Utilising the high-resolution grain size records and strong age control, I also investigate phase relationships between changes in physical grain size and insolation to shed light on climatic processes that could have forced MOW strength changes. The analysis reveals that late-winter/spring precipitation is more important than summer monsoonal freshwater run-off for MOW strength changes for majority of the time between ~370 and 60 ka.

1.1.5 Chapter 5: Conclusions and future work

This chapter summarises and links the conclusions of each chapter and provide thoughts for how best to extend and/or confirm some of the findings in potential future studies.

1.2 Ocean drilling and sediment archives of palaeoclimate

The International Ocean Discovery Program (IODP), previously the Ocean Drilling Program (ODP) and Integrated Ocean Drilling Program, has been recovering and investigating ocean sediment archives for over fifty years. Our knowledge of Cretaceous and Cenozoic palaeoclimate and palaeoceanography have advanced enormously as a result of this effort. In particular our understanding of the relationships between tectonically induced changes, orbital variations, glaciations, sea level change and millennial scale variability have progressed. Scientific objectives have focussed broadly on the differences between our current icehouse world and warm greenhouse worlds in deep time, and the drivers of rapid and abrupt climate changes (Becker, 2014). Techniques in recovering undisturbed sediments have improved, including advanced piston coring (APC) and multi-hole investigations using a splice, has further enhanced the quality of palaeoclimate records.

From November 2011 to January 2012 IODP Expedition 339 drilled 6 sites on the southwest Iberian Margin and within the Gulf of Cadiz (Figure 1.1) with the aim of uncovering the evolution of the Mediterranean Outflow Water (MOW) and its influence on global climate. An additional Site, U1385, was drilled with the goal of building a Pleistocene palaeoclimate reference record (Expedition 339 Scientists, 2012). Gulf of Cadiz sediments comprise a complex contourite depositional system which extends to the west Iberian Margin. Contourites are marine sedimentary sequences deposited under the, at least semi-permanent, influence of bottom oceanic currents (Stow et al., 2002), in this case MOW. Sedimentation rates in the contourites are often significantly higher (i.e. >10 cm/kyr) compared to normal background rates (Expedition 339 Scientists, 2012; Hernandez-Molina et al., 2014).

This thesis predominantly focusses on IODP Site U1391 (water depth 1085 m), located in the contourite sequence on the west Iberian Margin. Site U1391 was selected for the study of MOW for multiple reasons. It is more distal from the Straits of Gibraltar than many other studies, particularly the other records generated form Exp. 339, therefore giving an alternative perspective on MOW evolution. The close correlation of proxies with IODP Site U1385 allow the transfer of a robust age model and provides a 'control' site, under the influence of a different water mass, to test MOW changes against. Three holes (i.e., A, B and C) were drilled at Site U1391, with holes A and B extending down to approximately ~354 m below sea floor and hole C covering between 340 m and ~671 m below sea floor. These recovered sediments range from the mid Pliocene to the Holocene (Expedition 339 Scientists, 2013c)

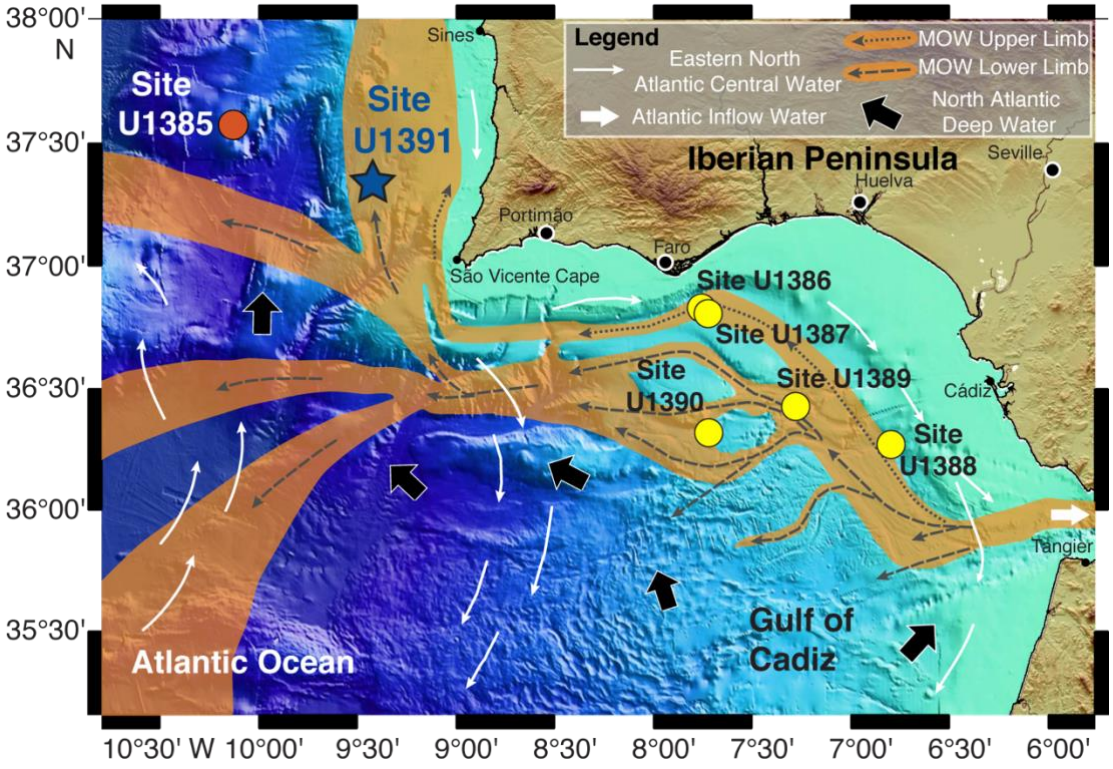

Figure 1.1. Location of IODP Sites U1391 (1085 mbsl) and U1385 (2585 mbsl) and other Expedition 339 sites on the Southwest Iberian Margin. Flow paths of MOW and other water bodies are shown (modified from Expedition 339 Scientists, 2012; Hernandez-Molina et al., 2014).

1.3 West Iberian Margin sediments

The west Iberian Margin has been a focus of extensive ocean drilling and research due its unique climate records documented in the sediments. Nick Shackleton's seminal papers in 2000 and 2004 noted that the planktic and benthic $\delta^{18}O$ records of MD95-2042 on the south-west Iberian Margin closely resemble the temperature records from Greenland and Antarctic ice cores, respectively (Shackleton et al., 2004; Shackleton et al., 2000). Additionally, sediments in the area provide direct, high-resolution links to European terrestrial records due to the direct contribution of sediments from the nearby Tagus River (Sánchez Goñi et al., 1999; Tzedakis et al., 2009). The clear and unequivocal links these records provide between the marine, terrestrial and cryosphere realms, combined with continuous high sedimentation rates through glacial and interglacial climates (~10 cm/kyr), allow for excellent age control and for the construction of a reference section (Hodell et al., 2015). This confluence of features is partly due to the hydrography of the region, as depicted in Figure 1.2. The seasonally variable Portugal Current system occupies the surface down to ~100 m water depth. Seasonal shifts in strength of the Azores High pressure

system promote direction of flow change with the northward flowing Iberian Poleward Current dominant during winter and the southward flowing Portugal Current dominant during summer (Relvas et al., 2007). Below this surface system there are two components of the Eastern North Atlantic Central Water (ENACW): a northward flowing subtropical component (ENACWst) at ~200–300m and a southward flowing colder nutrient-rich subpolar component (ENACWsp) at ~300–400 m (Arístegui et al., 2006). MOW flows northward beneath ENACWsp from ~600 down to ~1,500 m. North Atlantic Deep Water (NADW) dominates below MOW and flows southward. Antarctic Bottom Water (AABW) occupies depths below the NADW, but can increase in volume, shoaling to reach ~2,500 mbsl during glacials (Hodell et al., 2013).

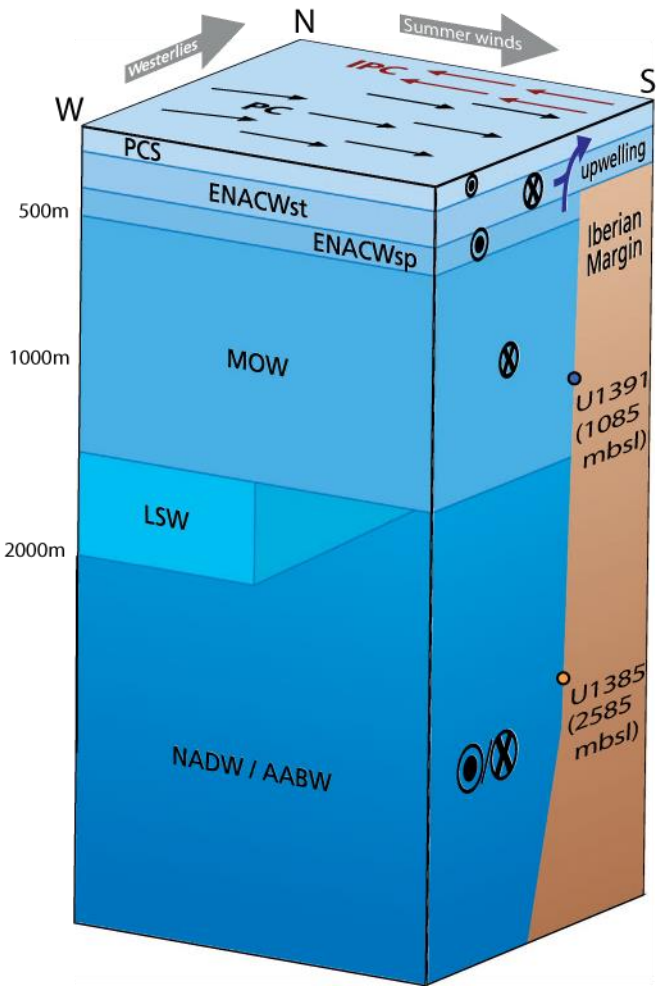

Figure 1.2. Schematic depiction of Iberian Margin water masses (adapted from Datema et al 2017) with the positions of Sites U1391 and U1385. IPC = Iberian Poleward Current, PC = Portuguese Current, PCS=Portugal Current System, ENACWst = Eastern North Atlantic Central Water sub-tropical, ENACWst = Eastern North Atlantic Central Water sub-polar, MOW = Mediterranean Outflow Water, LSW = Labrador Sea Water, NADW = North Atlantic Deep Water (present at inter-glacials), AABW = Antarctic Bottom Water (present at glacials).

1.4 Mediterranean outflow water

1.4.1 Modern Mediterranean outflow water oceanography

The Mediterranean-Atlantic exchange exerts strong control on Mediterranean oceanography as well as the structure of the northeast Atlantic. Modified Atlantic water (MAW), sourced from the Azores current in the North Atlantic, flows through the Strait of Gibraltar at the surface across toward the eastern edge of the Mediterranean and is a large supply of relatively fresh water, compensating for the net evaporation with the Mediterranean basin (Figure 1.3)

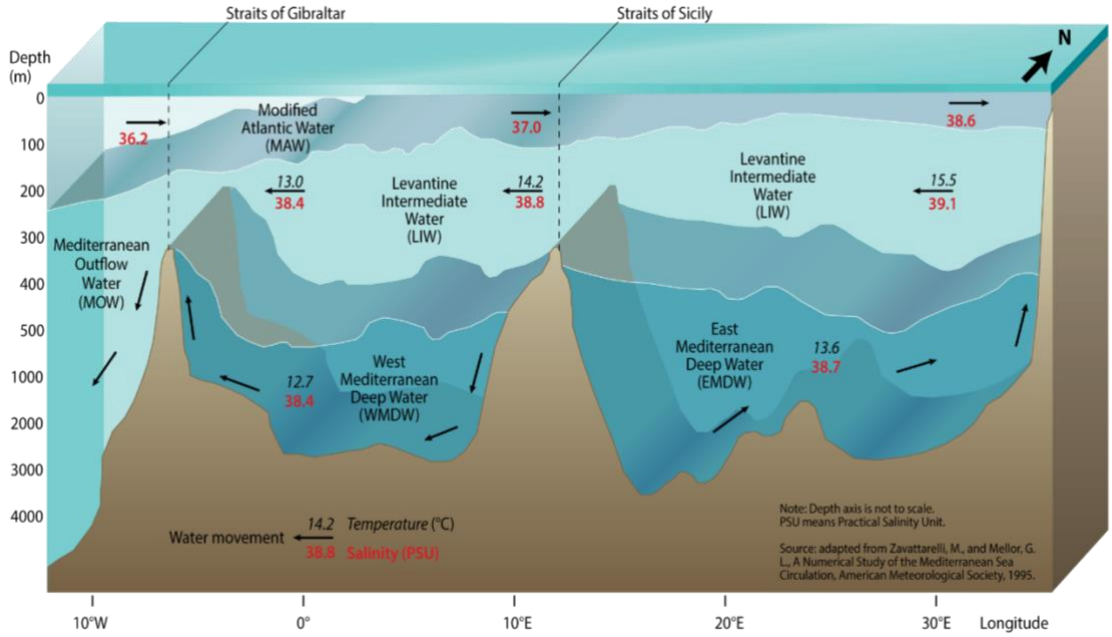

Figure 1.3. Schematic depiction of the vertical distribution of Mediterranean water masses, modified from GRID-Arendal (2013), which was adapted from Zavattarelli & Mellor (1994).

On short timescales (years), the composition of MOW is highly variable. Any combination of four water masses, Levantine Intermediate Water (LIW), Tyrrhenian Deep Water (TDW), Winter Intermediate Water (WIW), and Western Mediterranean Deep Water (WMDW), can contribute to changes in MOW composition (Millot, 2009). TDW is formed from mixtures of eastern Mediterranean deep waters and a number of other water bodies found in the Tyrrhenian sea, WIW is formed in the western basin and found above the LIW, and WMDW is generated in the Gulf of Lions, Tyrrhenian and Balearic Seas (Millot, 2009). However, it is generally agreed that over glacial-interglacial timescales, LIW is the most prominent contributor (~90%) to compositional change. LIW forms in the eastern Mediterranean when surface water temperatures

are lowered and salinities increase in response to strong outbreaks of cold dry air masses over the region during winter (Rohling et al., 2015). LIW then flows westward to the Strait of Gibraltar. Across the Alboran Sea the WMDW shoals from ~800 up to 284 meters below sea level (mbsl) because of Bernoulli aspiration with the fast-flowing overlying LIW promoting increased buoyancy in WMDW, causing it to be drawn upwards over the Camarinal Sill (the shallowest point in the Strait of Gibraltar). Upon exiting the Strait of Gibraltar, the relatively cold and saline MOW flows downslope at 0.67 ± 0.26 Sv and splits into an upper limb and a lower limb (Millot, 2009; Tsimplis & Bryden, 2000). These limbs are formed in response to gradual entrainment of Atlantic water into the outflowing MOW plume. The outer plume undergoes frictional mixing and slows relative to the central core (O'Neill-Baringer & Price, 1999). Ekman veering causes the central unmixed flow to veer downward at a steeper angle and to be injected into the Atlantic at a greater depth than the surrounding outer plume Mediterranean water (Rogerson et al., 2012). While the two limbs have similar salinities, ~38.5 psu, there is a 1.5–3.5°C temperature difference between them causing them to attain different isopycnal depths between ~600 and ~1,500 m. In the Gulf of Cadiz, MOW can be traced flowing to both the west and south; however, a significant proportion turns northwards, due to a combination of the Coriolis force and bathymetry, flowing around the West Iberian Margin (Iorga & Lozier, 1999) (Figure 1.1). Here, further from the Strait of Gibraltar, greater entrainment of Atlantic water means that the two limbs are less distinct than in the Gulf of Cadiz. Thereafter, MOW can be traced as far north as the Norwegian-Greenland Sea (Lozier & Stewart, 2008).

1.4.2 MOW through the Plio-Pleistocene

Following the Messinian salinity crisis and the deposition of extensive evaporites, renewed tectonic activity re-opened the Straits of Gibraltar at around 5.33 Ma, and limited volumes of Mediterranean water began intruding into the North Atlantic. Following this event, it has been suggested that MOW evolution underwent four major phases through to the present day, as evidenced by seismic records and IODP Expedition 339 drill cores (Hernandez-Molina et al., 2014). From ~5.2 – 4.5 Ma there is evidence of slope instability and downslope activity from the Straits of Gibraltar responding to tectonic activity with slumps, debrites and turbidites, but only limited contourite deposition. This indicates a lag between the opening of the Straits of Gibraltar and a consistent outflow; it may have been hampered by more similar salinities between the Mediterranean and the eastern North Atlantic at this time. The second phase occurred from ~4.5 to 3.5 Ma with more persistent contourite sequences indicating MOW circulation in the Gulf of Cadiz, with additional evidence showing MOW as an intermediate and deep-water mass in the

North Atlantic (Maslin et al., 1998). Coincident with more active North Atlantic circulation, additional MOW intensifications have been reported at ~3.8 Ma and 3.5 Ma (Hernández-Molina et al., 2014; Khelifi et al., 2009). Between ~3.2 and 2.1 Ma, the third phase, significant contourite deposition indicates enhanced MOW circulation. Two hiatuses from 3.2 - 3 Ma and 2.4 - 2.1 Ma, suggesting intensified flow, coincide with higher amplitude insolation oscillations linked to the ~400 kyr eccentricity cycle, an early indicator of a relationship between MOW variability and orbital cycles (Maslin et al., 1998). The fourth and final phase, from ~2.1 Ma to present is characterised by higher sedimentation rates and rapid contourite deposition. The mid-Pleistocene transition is thought to be linked to the cause of a regional discontinuity, after which an enhancement of MOW activity appears to occur evidenced by a change in the drift stacking pattern and increased upslope progradation (Hernandez-Molina et al., 2014).

1.4.3 MOW Research in the Late Pleistocene

On millennial to orbital timescales, MOW variability is primarily controlled by the interplay between the dimensions of the Strait of Gibraltar, the density contrast between Atlantic and Mediterranean water masses, and the density structure within the North Atlantic. These factors affect both the strength of outflow and isopycnal equilibration (Rogerson et al., 2005, 2010, 2012). Glacioeustatic sea-level change was the primary control on MOW over the last glacial cycle (Rogerson et al., 2012). The ~120 m sea-level fall (relative to present) associated with the Last Glacial Maximum severely reduced the size of the channel at the Strait of Gibraltar, decreasing exchange between the Mediterranean and Atlantic. The result was a less voluminous but denser and deeper-equilibrating MOW relative to present (Rogerson et al., 2012). Changing density gradients across the Strait of Gibraltar exerted a secondary control on MOW flow strength over the last glacial cycle, modulated by precipitation-evaporation around the circum-Mediterranean region, riverine input, and inflow of Atlantic water along the surface at the Strait of Gibraltar (Rogerson et al., 2012). Freshwater input into the Mediterranean was less pronounced during stadials and precession maxima (insolation minima, i.e., aphelion near the northern summer solstice) than during interstadials and precession minima (insolation maxima, i.e., perihelion near northern summer solstice) because of diminished northward migration of the Intertropical Convergence Zone (ITCZ) and African summer monsoons, and, in winter, steering of storm tracks (Bosmans et al., 2015; Kutzbach et al., 2014) or changes in sea-level pressure at the Azores High (Bosmans et al., 2020). The resultant combination of more saline surface waters and cooler air temperatures acted to enhance Levantine Intermediate Water (LIW) and deep-water formation in the eastern Mediterranean and, in turn, the rate of Mediterranean Outflow and salinity export to

the North Atlantic (Bahr et al., 2015; Rogerson et al., 2012; Toucanne et al., 2012). This mechanism is hypothesized to have helped to reinstate vigorous overturning in the North Atlantic following stadial surface water freshening (Voelker et al., 2006).

Thanks to Integrated Ocean Drilling Program (IODP) Expedition 339 (Mediterranean Outflow) (Expedition 339 Scientists, 2012), several studies have explored MOW evolution deeper into the Pleistocene. Benthic foraminiferal assemblages over the last 900 kyr show distinct glacial-interglacial contrasts at Site U1391, and these have been related to changes in MOW activity (interglacial maxima and glacial minima with peak velocities during marine isotope stage [MIS] 11) (Guo et al., 2017). These findings are consistent with the suggestion that higher salinity MOW and a reduced Atlantic vertical density gradient during glacials drive deeper isopycnal equilibration of MOW and therefore a reduced contribution to Atlantic overturning (Rogerson et al., 2005). At IODP Site U1386 in the Gulf of Cadiz (Figure 1.1), $\delta^{18}O$ and grain size (mean weight percent of the 150–63 μm fraction) reveal three distinct phases of MOW variability back to 570 ka (Kaboth et al., 2017). Significant MOW variability was identified between 570 and 475 ka (Phase III) and from ~130 ka to the present (Phase I). The grain-size record of Site U1386 suggests that MOW was significantly slower in the intervening period between 475 and 130 ka (Phase II). Shifts in MOW water mass sourcing are invoked to explain these changes, but records are needed from sites in different water depths to test this hypothesis, to determine the history of MOW depth equilibration variability and to understand the forcing mechanisms involved.

1.4.4 MOW – AMOC Relationship

The relationship between Mediterranean Outflow Water (MOW) and North Atlantic circulation strength and structure is complex. MOW provides a salt source for intermediate depths of the North Atlantic, but the effects of this input are not well understood. It is widely (but not universally) suggested that the salt supplied by MOW significantly increases the rate of North Atlantic overturning today and had variable impacts during the last glacial cycle (Bahr et al., 2018; Llave et al., 2006; Rogerson et al., 2010, 2012; Swingedouw et al., 2019; Voelker et al., 2006). MOW probably exerts significant circulatory impact following Greenland stadials, forming a crucial part of the negative feedback mechanism that promotes the reinstatement of vigorous North Atlantic deep-water formation and overturning from its weakened cold-interval state (Llave et al., 2006; Voelker et al., 2006). Furthermore, significant reorganizations of shallow and intermediate water mass structure in the North Atlantic may arise in response to changes in MOW-injection depth (Ivanovic et al., 2013a, 2013b) and the strength of the Azores Current, and consequently,

European ice sheet dynamics are sensitive to MOW entrainment into North Atlantic intermediate water masses (Kaboth-Bahr et al., 2018). In contrast to the idea that increased MOW-fed salinity to the North Atlantic enhances overturning circulation, one recent numerical analysis of the impact of sapropel events suggests that the upper AMOC cell may weaken or strengthen, depending on the rate of freshwater input to the Mediterranean (Swingedouw et al., 2019).

1.5 Rock and environmental magnetism

1.5.1 Essentials

Rock magnetism concerns the detailed study of magnetic mineralogy and magnetic properties of, often discrete, hard rock or sediment samples. Environmental magnetic studies involve the investigation of links between the magnetic properties of sediments and the source-to-sink environmental processes that affect them.

At its fundamental level, a magnetic moment arises from two sources of electronic motions: the orbits and the (unpaired) electron spins (see Tauxe, 2018). In many geological materials, the orbital contributions cancel out because they are randomly oriented with respect to one another, and the magnetization arises from the electronic spins. Unpaired electronic spins behave as magnetic dipoles and can respond to an applied field, creating a net magnetisation in the direction of the applied field. Some geological materials do carry a magnetisation without the presence of an applied field. This is caused by strong interactions between neighbouring electron spins working together to produce a net field, that can occur in certain crystal structures but only remains if thermal energy is lower than magnetic energy. This is called a remnant magnetisation that forms the basis of palaeomagnetic studies. How stable this magnetisation is within a particle, and the strength of magnetic field required to change the magnetic moment, is known as the coercivity (Lowrie & Fichtner, 2020; Tauxe et al., 2018).

Within magnetic particles, magnetisations will arrange themselves into the lowest possible stable energy state, which is strongly dependent on the particle size, resulting in three classes of magnetic particles that are related to size. In the smallest magnetic minerals, electron spins are essentially lined up and the particle is uniformly magnetised; this is known as single domain (SD). The largest magnetic minerals have zones of different magnetisation, termed multi-domain (MD), which helps to reduce the overall external field and energy of the particle. In particle sizes between SD and MD, internal magnetisations find more complex configurations to reduce their

energy state, such as flower and vortex structures. They are termed pseudo-single domain (PSD) as they show many similar properties to SD particles (Lowrie & Fichtner, 2020; Tauxe et al., 2018).

In geological magnetic studies there are four main groups of minerals, ferromagnetic, antiferromagnetic, paramagnetic and diamagnetic. In the absence of an applied field ferromagnetic minerals retain a strong remnant magnetisation, for example magnetite and maghemite, and antiferromagnetic minerals retain only a weak remnant magnetisation, for example hematite and goethite. Antiferromagnetic minerals will typically have a significantly higher coercivity than ferromagnetic minerals. Paramagnetic minerals (e.g., clays and silicates) do not retain a remanence; however, in the presence of a magnetic field they will produce an induced magnetisation, proportionate to the strength of the field. Diamagnetic minerals (quartz and carbonates for example) produce only a small negative magnetic moment in response to an applied field (Tauxe et al., 2018).

1.5.2 Magnetic proxies and applications to marine sediments

1.5.2.1 Magnetic Susceptibility

Low-field magnetic susceptibility (χ, mass specific, or κ,volume specific (used in this study)) is one of the most widely used magnetic parameters in the environmental sciences. It is defined as the ratio between an applied magnetic field (H) and the resultant induced magnetisation (M) from a material, χ = dM/dH. Magnetic susceptibility is sensitive to contributions from the entire assemblage of minerals making it a complex parameter to interpret on its own. κ is most sensitive to paramagnetic and ferromagnetic minerals and a stronger response can be acquired from some coarser particles (Liu et al., 2012; Tauxe et al., 2018).

Whilst κ concerns the bulk susceptibility of a sample, it is also possible to measure the directional susceptibility using a technique termed anisotropy of magnetic susceptibility (AMS). This proxy can determine the orientation of grains and the overall fabric of a sediment sample. AMS describes the directional variation of magnetic susceptibility and is expressed as a second-rank tensor converted to a magnitude ellipsoid (King & Rees, 1962). Three eigenvalues are used to represent the maximum, intermediate and minimum axes of the ellipsoid, $\kappa_{max} > \kappa_{int} > \kappa_{min}$ (or $\kappa 1 > \kappa 2 > \kappa 3$) (Hrouda, 1982). The inclination and declination of each principal axis of the ellipsoid can be plotted on lower hemisphere projections and, alongside other calculated parameters, can reveal information about the nature of deposition (Figure 1.4). In the majority of cases where a

current is acting on sediment, the orientation of the κ_{max} axis is parallel to the flow direction (Taira, 1989). AMS parameters and their definitions are summarised in Table 2 in Appendix B.

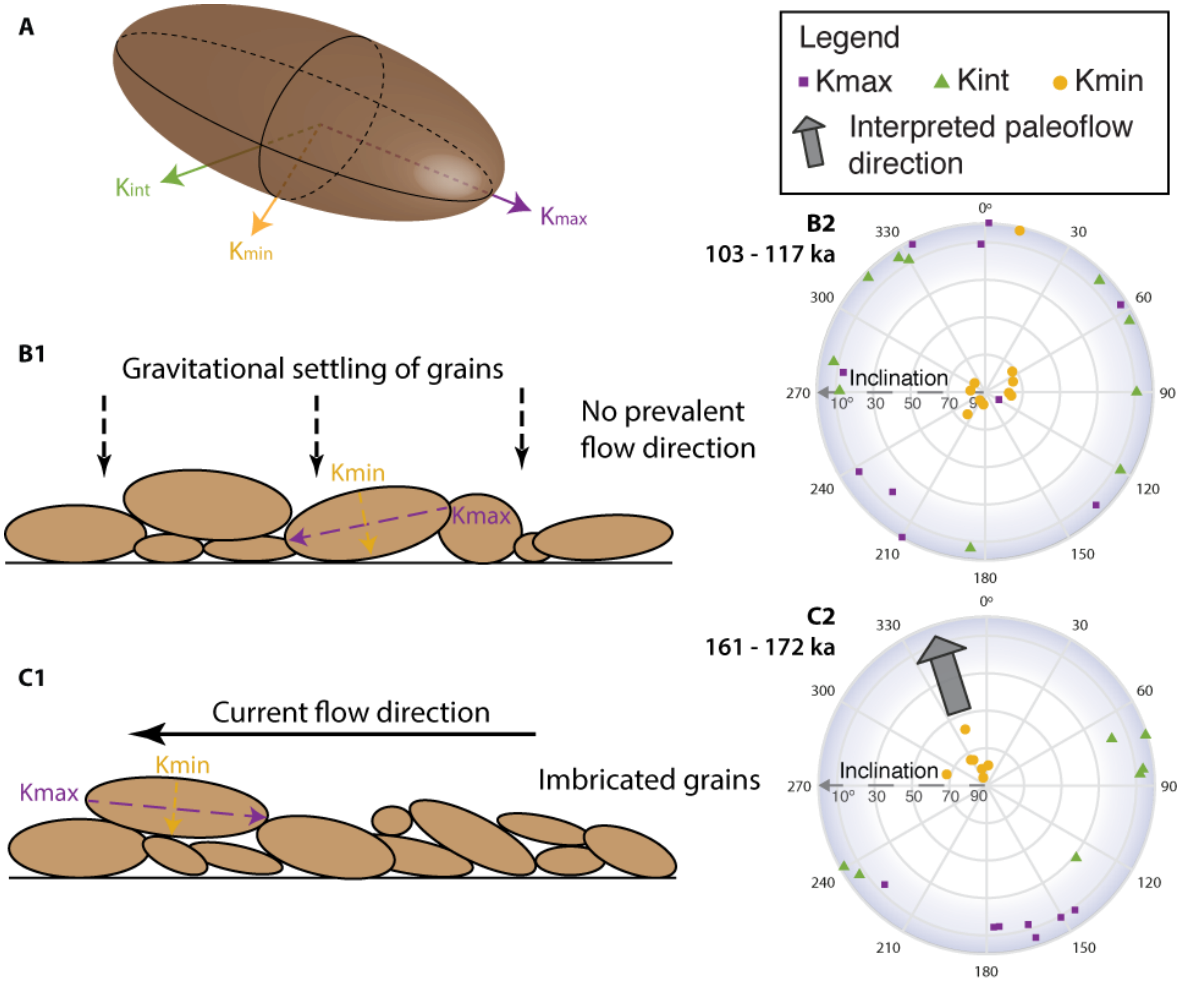

Figure 1.4. Schematic depiction of paleocurrent information derived from anisotropy of magnetic susceptibility data. (A) Illustration of the maximum (κ_{max}), intermediate (κ_{int}), and minimum (κ_{min}) axes of the AMS ellipsoid. (B1) Gravitational settling of grains in quiet water settings results in well-spread κ_{max} axes declinations and κ_{min} clustered around the centre, as shown in (B2) stereographic projection. (C1) Intermediate strength current flow imbricates κ_{max} axes opposite to the flow direction and skews κ_{min} axes from vertical into the direction of flow. In this instance κ_{max} axes are grouped to the south, and κ_{min} axes skewed to the north, both of which indicate northward flow, as shown in (C2). (B2–C2) Lower hemisphere stereographic projections of AMS κ_{max}, κ_{int}, and κ_{min} declination and inclination values from two intervals demonstrating each respective fabric type. The figure is based on similar figures in Taira (1989) and Tauxe (2010).

The room-temperature magnetic properties of magnetic materials often change at higher temperatures. At higher temperatures the remanence of remanence carrying minerals breaks down to show paramagnetic behaviour. This threshold temperature for magnetite, known as its Curie Temperature, is ~580 °C (e.g., Liu et al., 2012). These behaviours are observable by heating a sample up to ~700 °C and measuring the susceptibility at evenly spaced intervals before cooling back to ~50 °C. This measurement is commonly performed in an Argon atmosphere to avoid oxidation of minerals, which would show different behaviour (e.g., Jordanova & Jordanova, 2016; Xuan et al., 2012).

1.5.2.2 Hysteresis Parameters

Hysteresis parameters can be used to indicate domain states and mineralogy (Day et al., 1977; Dunlop, 2002; Heslop & Roberts, 2012). During measurement of a so-called hysteresis loop (Figure 1.5), the field is increased from zero (1 in Figure 1.5) to the state where all the moments are parallel to the applied field, called saturation (Ms; 2 in Figure 1.5). Saturation remanence (Mr) is reached when the applied field is reduced and reaches zero (3 in Figure 1.5). Here the magnetic moments show a remnant magnetisation in the orientation of the initially applied field. The field is then increased in the opposite direction and the coercivity (Hc) is found once half the magnetic moments have been reversed and the net magnetisation is zero (4 in Figure 1.5). The field then continues to be increased to saturation in the reverse direction; it is then reduced and reversed once again to close the loop. The coercivity of remanence (Hcr), measured separately to the hysteresis loop in a backfield experiment, is the applied field that leaves zero net remanence when reduced to zero itself.

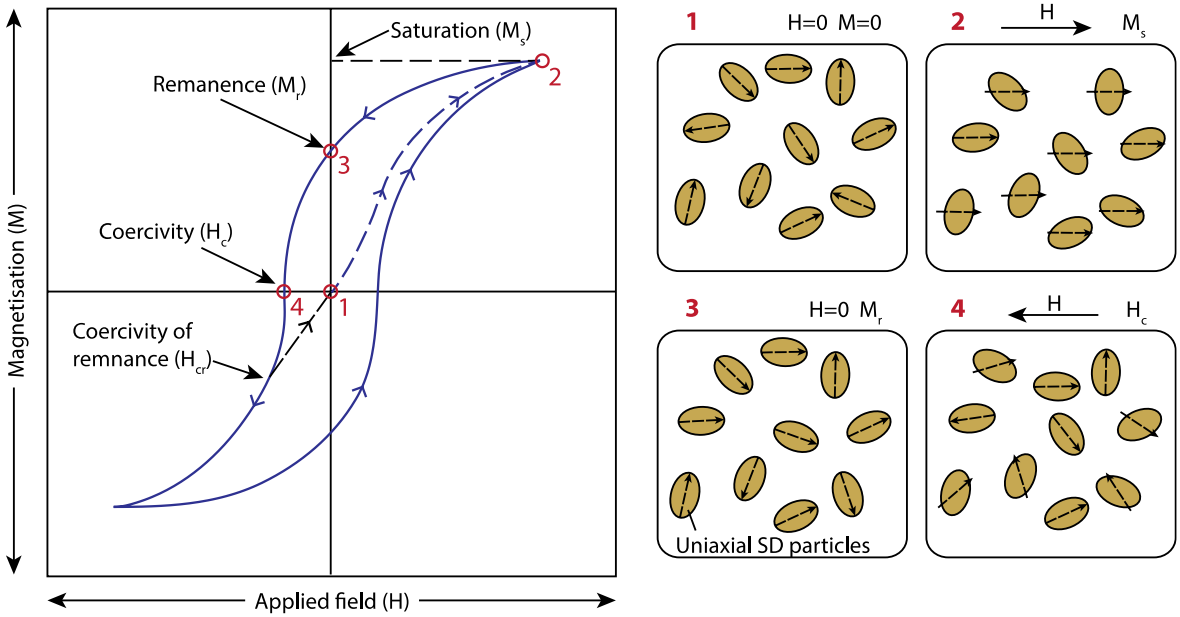

Figure 1.5. Schematic illustration of a hysteresis loop measurement adapted from Tauxe et al (2018). Measurement begins at step 1 with applied field (H) and magnetisation (M) at 0. See text for full explanation of steps.

The ratio of Hcr/Hc plotted against Ms/Mr in a Day Plot is a widely used technique for indicating the domain state of the bulk mineralogy (Day et al., 1977), though it has potential complexities and it should be used with caution (Roberts et al., 2018).

First order-reversal curves (FORCs) reveal details of the coercivity distribution and magnetic interactions and are particularly sensitive to magnetic domain state and grain size within a bulk sample. By measuring many partial hysteresis loops within a full hysteresis loop, a FORC diagram can be produced by taking the second order derivative of the cumulative magnetisation (Roberts et al., 2014; Roberts et al., 2000).

1.5.2.3 Laboratory-induced remanent magnetisations

Anhysteretic remnant magnetisation (ARM) is another common measurement and is sensitive to the concentration of fine-grained ferromagnetic minerals. An ARM is acquired by a sample placed in an alternating field (AF) superimposed with a direct current (DC) bias field , commonly 50 µT, leaving a preference in this direction in the remagnetised grains. Stepwise alternating field (AF) demagnetisation and measurement is often carried out at fields, generally, of up to 100 mT in order to learn about the coercivity distribution of the sample (Liu et al., 2012). Isothermal remnant magnetisation (IRM) is a different type of laboratory induced magnetisation that results

from exposure of magnetic particles to an applied field that is greater than their coercivity, and therefore flips their magnetisation to a more favourable angle relative to the direction of that field. These fields are often applied instantaneously at 300 mT, the approximate field at which magnetite becomes fully saturated, or ~1000 mT, at which most remanence carriers are fully saturated, commonly termed saturation isothermal remnant magnetisation (SIRM). Haematite and goethite however will likely not be fully saturated at 1000 mT, requiring much stronger fields (Liu et al., 2012).

Through progressive applied field strength increases (often up to 1 T), a detailed picture of the behaviour of remanence of a sample up to SIRM can be acquired; known as an IRM acquisition (IRMacq) measurement. The shape of the gradient curve of IRMacq is very informative, and unmixing these data can give information about the different minerals within the sample. This is achieved by deconvolving the differential curve into a number of, for example, cumulative log-gaussian or endmember functions that sum together to represent the original data, where each function represents a magnetic component (Egli, 2004; Kruiver et al., 2001; Maxbauer et al., 2016; Robertson & France, 1994).

1.5.2.4 Rock magnetic ratios and proxies

Ratios between ARM, IRM and κ can be used to determine different magnetic properties of sediment samples. The ratio of κ_{ARM} (ARM/DC bias field, as the ARM is commonly proportional the DC bias field) to κ, κ_{ARM}/κ, indicates the grain size of the magnetic particles because κ_{ARM} is more sensitive to finer magnetic particles while κ is generally more sensitive to coarser magnetic particles (Banerjee et al., 1981). Similarly, ARM/SIRM is also a magnetic grain size indicator, however it only uses the remanence carrying particles, disregarding superparamagnetic particles (Peters & Dekkers, 2003) and grains that are too coarse to carry remanence. The ratio of SIRM/κ has been demonstrated as an indicator for the presence of iron sulphide minerals (Roberts, 1995).

An estimate of the coercivity of a sample can be obtained through calculating the median destruction field (MDF) of ARM or IRM. The MDF is the alternating field required to remove half of the remanence from a sample (Tauxe et al., 2018).

Calculation of a parameter called hard isothermal remnant magnetisation (HIRM) is used to isolate and determine the contribution of antiferromagnetic particles (commonly with coercivities of >300 mT) which are commonly masked by the much stronger remanences of ferrimagnetic particles with coercivities of <300 mT. HIRM is defined as HIRM = (SIRM + $IRM_{-300\ mT}$)/2; -300 mT denotes a 300 mT field applied in the opposite direction to, and after, the SIRM. The S-ratio,

calculated as ((IRM$_{-300\ mT}$ / SIRM) +1) / 2, can be used to estimate the proportion of high coercivity minerals in a sample (Bloemendal et al., 1992; King & Channell, 1991). As the S-ratio can be influenced by both grain size and mineralogy, it is therefore useful in combination with another parameter, the L-ratio which is calculated as (SIRM + IRM$_{-300\ mT}$) / (SIRM + IRM$_{-100\ mT}$). The L-ratio is used to determine if there are significant changes in the hard coercivity component (Liu et al., 2007). If the L-ratio and HIRM show a linear relationship, changes in the S-ratio are likely driven by changes in mineralogy (i.e., type of mineral and provenance), whereas if the L-ratio is more constant and shows no relationship with HIRM, changes in the S-ratio are more like driven concentration variations of the same mineral type from the same source (Liu et al., 2007).

1.5.2.5 Diagenesis

Environmental and rock magnetic techniques can be used as proxies for reductive diagenesis in marine sediments, as iron bearing minerals are highly sensitive to redox changes. Several mechanisms can produce reductive conditions, for example, elevated levels of organic matter, produced by high productivity in the water column, respire and reduce oxygen concentrations in pore waters. Other mechanisms can include stratified bottom water conditions, upward diffusion of methane or riverine input of organics. Different oxidants yield progressively lower energy in pore-water environments. These environments in marine sediments range from oxic to nitrogenous to manganiferous to ferruginous to sulphidic to methanic. In oxic environments, Fe^{3+}-bearing minerals are precipitated by surface oxidation of detrital minerals. In Ferruginous environments, dissimilatory iron-reducing bacteria mediate the release of Fe^{2+} by dissolution of detrital and authigenic iron oxides. This Fe^{2+} can enable magnetotactic bacteria to biomineralize intracellular magnetite. In sulphidic environments where hydrogen sulphide is available (for example from bacterial sulphate reduction), it can react with Fe^{2+} to produce iron sulphide minerals (Roberts, 2015). These resultant mineralogical changes are detectable in many of the magnetic measurements outlined above, yielding information about environmental processes.

1.6 X-Ray Fluorescence: Essential theory and expanding use in Palaeoceanography

X-ray fluorescence (XRF) analysis is based on the principle of excitation of electrons by incident X-ray radiation. Electrons from inner atomic shells are ejected leaving a vacancy which is filled by higher energy electrons from outer atomic shells. The energy difference between the inner and

outer shells is surplus and emitted as a secondary pulse of X-ray radiation. Each element has characteristic fluorescence wavelengths and energy signatures; therefore, spectra can be deconvolved to determine relative element abundance. Progress in XRF instrumentation has allowed the continuous measurement (down to 2 mm interval spacing) of these XRF spectra down marine sediment cores, providing a high-resolution record of semi-quantitative elemental abundances. Additionally, in comparison to discrete destructive methods, results are obtained relatively rapidly, non-destructively at the split core surface. (Croudace et al., 2019; Richter et al., 2006; Weltje & Tjallingii, 2008).

Typically, XRF results are presented in the form of counts rates (per second per unit area) and attempts to convert this to concentrations have shown limited success with count vs concentration cross plots showing both bias and scatter (Böning et al., 2007; Tjallingii et al., 2007). Factors such as variable water content, irregular or cracked sample surfaces and element interactions can cause this non-linearity, meaning XRF data are regarded as only semi-quantitative (Richter et al., 2006; Tjallingii et al., 2007). A simple solution to this problem was established by Weltje and Tjallingii (2008). The log-ratio of element intensities was found to have a linear relationship with the log-ratio of element concentrations, meaning relative changes in element abundance from XRF core scanner data can be safely interpreted.

XRF is now a hugely popular technique in the marine sciences and palaeoceanography, with two main types of core scanner, the ITRAX and the Avaatech. These provide a potential tool for uses including, but not limited to, core to core correlation, grain size, productivity, carbonate content, diagenesis and mineralogy variations.

The ratio of Ca/Ti (or Ca/Fe) is one of the most commonly used XRF ratios as it broadly indicates the proportion of carbonate to terrestrial material, useful for a multitude of reasons including site-to-site correlation and understanding the general climatic setting. Zr/Al (or Zr/Rb) can be used as a grain size indicator as Zr is commonly found in resistate minerals whereas Al and Rb are more concentrated in clays, meaning this is a coarse to fine particle ratio (Bahr et al., 2014). Ca/Sr has been used as an indicator of the presence of ice-rafted debris (Hodell et al., 2008). Levels of organic productivity can be associated with the Br/Ti ratio, as Br is concentrated in organic matter (e.g., Ziegler et al., 2008). A high proportion of sulphur relative to iron, Fe/S, can be indicative of reducing conditions and reductive diagenesis as this process produces iron sulphide minerals (Sluijs et al., 2009).

1.7 Grain Size: Essentials and measurement methods

Sediment drifts, contourites, are produced by deep water currents flowing along bathymetric contours, eroding, transporting and depositing high volumes of material at water mass boundaries where flow velocity is lower. Sediment supply can come from a wide range of sources including vertical flux from windblown particles, river suspension plumes, biogenic material produced by sea surface primary productivity, direct downslope flux from low-density turbidity currents and hyperpycnal plumes, erosion of the sea floor and resuspension by bottom currents (Stow et al., 2008). Variations in speed of the flow are recorded within the contourites as changes in physical grain size. Coarser mean grain size is related to intervals of faster flow due to the selective deposition of slower settling particles. The higher energy environment preferentially allows the deposition of coarser grains, as according to Stokes' Law of settling velocity, alongside turbulence and shear stresses. The sortable silt mean proxy, SS, is the mean size of terrigenous particles in the range of 10 – 63 μm (McCave et al., 1995). The SS range represents particles that are hydrodynamically sorted by ocean currents. Finer particles, <10 μm, display cohesive behaviour and so may not be sorted and deposited individually, rather as aggregates. Therefore, when measured in a disaggregated state, results will be misleading as the particles may not have been deposited in the disaggregated state. The top of the range, 63 μm, represents the boundary between silt and sand sized particles. Above this value, particles no longer show viscous settling in water and no longer obey Stokes' law (McCave et al., 1995).

When interpreting SS it is important to establish its relationship with SS%; the percentage of material greater than 10 μm within the entire silt size range, i.e. 4 – 63 μm. This helps to establish that the principal process governing grain size distribution is current activity. A positive linear relationship between SS and SS% indicates that the material has been sorted by a current. The deposition of fine sediment is suppressed by a strong current meaning the proportion of sortable silt in the total <63 μm fraction will increase as the SS increases (McCave, 1985; McCave et al., 1995). If this correlation is not seen, it is possible that multiple sources of sediments are influencing variations in the mean grain size, for example the deposition of IRD (McCave & Hall, 2006)

It is important to note that biogenic and carbonate material are not considered and removed before measurement. This is because their net bulk densities are highly variable and their size does not correspond to that of much denser quartz particles. Additionally, these components could grow in situ and would therefore not have been hydrodynamically sorted.

When it comes to measuring grain size distribution, there are three main types of instrument which work on different principles. The instrument of choice for ocean current speed research is the Sedigraph as it measures a velocity-equivalent spherical diameter which can be effectively linked to depositional processes. This is because it works on the principle of settling velocity linked to particle size according to Stoke's Law (McCave et al., 2006; McCave et al., 2017). As the Sedigraph is less commonly available, requires more maintenance and has longer measurement times, the Coulter Counter has been shown to be a reliable and suitable alternative. Here, the particle size distribution is found by suspending a diluted sample in a saline solution with known electrical impedance and passing it through an aperture causing a measurable impedance change related to the volume of the particle. The Coulter Counter measures volume equivalent grain size (McCave et al., 2006; McCave et al., 2017).

Laser sizers are very commonly used in the environmental sciences, however, pose an issue when one is attempting to answer questions related to current speed. They determine grain size based upon the diffraction pattern of light as particles interact with a laser beam. In the calculation of grain size distribution from this diffraction pattern, it is assumed that all particles are equant (Xu, 2000). Whilst this results in precise measurements for coarse silt and sand sized particles, the size of fine silts and clays can be overestimated due to some minerals having a platey shape, i.e. one axis significantly longer than the others (Buurman et al., 2001). Konert & Vandenberghe (1997) showed that for particles with diameters of 2 and 16 um were calculated to be 8 and 22 um sizes, respectively, when measured by a laser particle sizer (McCave & Hall, 2006; McCave et al., 2017).

Chapter 2 Climate-Induced Variability in Mediterranean Outflow to the North Atlantic Ocean During the Late Pleistocene

2.1 Introduction

As discussed in Section 1.4, MOW has shown variable behaviour since its inception with varying effects on North Atlantic circulation. Benthic foraminiferal assemblages over the last 900 kyr show distinct glacial-interglacial contrasts at Site U1391, and these have been related to changes in MOW activity (interglacial maxima and glacial minima with peak velocities during marine isotope stage (MIS) 11) (Guo et al., 2017). Shifts in MOW water mass sourcing have been invoked to explain observed changes between MOW regimes at Site U1386 (Kaboth et al., 2017). To test these hypotheses, records are needed from sites in different water depths, to determine the history of MOW depth equilibration variability and to understand the forcing mechanisms involved.

Here I present new multiproxy records from a two-site depth transect on the West Iberian Margin, IODP Sites U1391 and U1385 to study both the strength and depth variability of MOW on millennial to orbital timescales over the past ~416 ka and to make inferences about the relative importance of its driving mechanisms through time. We find that MOW behaviour shows a strong imprint of climate-induced variability with two distinct regimes of orbital and millennial timescale variability.

2.2 Material and Methods

2.2.1 IODP Sites U1391 and U1385

Contourites are deep-sea sediments deposited under the influence of a bottom water current. MOW-generated contourite sediment packages extend from the Gulf of Cadiz to the West Iberian Margin. IODP Site U1391 is the most distal MOW-entrained site from the Strait of Gibraltar drilled during Expedition 339 (Figure 1.1). The stratigraphic interval studied here consists of sandy contourites and alternating red/brown and green/grey calcareous muds (Expedition 339 Scientists, 2013c). Sedimentation rates at Site U1391 are an order of magnitude higher than at typical pelagic sites, averaging ~27 cm/kyr over the last ~1.5 Ma (Hernandez-Molina et al., 2014). While there is no fixed boundary between the upper and lower limbs of MOW on the western

Iberian Margin, U1391 is situated closer to the lower limb in terms of its water depth (~1,085 mbsl).

IODP Site U1385 is situated northwest of Site U1391 (Figure 1.1) in deeper water (~2,585 mbsl), under the influence of NADW and southern sourced waters rather than MOW. Sediments at Site U1385 comprise nannofossil muds and clays with cyclical carbonate and colour variability (Expedition 339 Scientists, 2013a) and average sedimentation rates of ~11 cm/kyr (Hodell et al., 2015). Site U1385 was drilled near the position of Core MD01-2444, which yielded planktic and benthic oxygen isotope signatures closely resembling temperature records from Greenland and Antarctic ice cores, respectively (Hodell et al., 2013; Shackleton et al., 2004). Marine sediments from the Iberian Margin also provide detailed records of European terrestrial climate because of the narrow continental shelf and proximity of the Tagus River (Tzedakis et al., 2009, 2015). The clear and unequivocal links that Site U1385 stratigraphy provide between the marine, terrestrial, and ice core records make it an ideal reference section at which to develop a high-resolution chronology (Hodell et al., 2015).

2.2.2 Samples

A total of 106 u-channel samples (with typical dimensions of ~150 x 2 x 2 cm) were taken from the archive-half core sections, following the Site U1391 shipboard stratigraphic splice. The u-channel samples cover a continuous sediment sequence of ~120 m with some overlapping intervals between samples from different holes. In addition, a total of 274 paleomagnetic cubes (each with a volume of ~7 cm^3) and 37 bulk sediment samples were collected at selected depth levels from the same ~120 m sediment sequence.

2.2.3 X-ray Fluorescence Scanning

Site U1391 u-channels were scanned on the ITRAX X-ray fluorescence (XRF) core scanner at the British Ocean Sediment Core Research Facility (BOSCORF) at the National Oceanography Centre Southampton. A surface profile scan was taken to allow detector height adjustments downcore to ensure constant detector to sediment distance. A 4-µm-thin SPEXCertiPrep Ultralene film covered the sediment surface before scanning. Data were collected at 0.5 cm intervals with a 15 s count time at 30 mA current and 30 keV voltage. Split archive-half core sections from Holes U1385D and U1385E were scanned at 1 cm resolution on an Avaatech core scanner at the Godwin Laboratory at University of Cambridge, as reported by Hodell et al. (2015).

The ratio of calcium to titanium (Ca/Ti) is commonly used as a correlative tool between cores in marine sediments (and is used as such in this study) and reflects the changing relative proportions of biogenic and detrital sediment sources at Site U1385 (Hodell et al., 2013). Zirconium is commonly found in resistate minerals, while rubidium is more highly concentrated in clay minerals; therefore, the ratio between the two (Zr/Rb) is used as a grain-size proxy (Bahr et al., 2014; Rothwell et al., 2006). Element counts in XRF data not only depend on concentration but also on physical properties, such as water content, geometry of the sample, and programmed settings of the scanner. Using log ratios has been shown to be an effective method of minimizing these effects, allowing elemental variations to be compared between records (Weltje & Tjallingii, 2008).

2.2.4 Anisotropy of Magnetic Susceptibility Measurements

The fabric of paramagnetic and ferrimagnetic grains in a sample can be estimated by measurement of the anisotropy of magnetic susceptibility (AMS). AMS describes the directional variation of magnetic susceptibility and is expressed as a second-rank tensor converted to a magnitude ellipsoid (King & Rees, 1962). Three eigenvalues are used to represent the maximum, intermediate, and minimum axes of the ellipsoid, $\kappa_{max} > \kappa_{int} > \kappa_{min}$ (or $\kappa 1 > \kappa 2 > \kappa 3$) (Hrouda, 1982). The inclination and declination of each principal axis of the ellipsoid can be plotted on lower hemisphere projections and, alongside other calculated parameters, can reveal information about the nature of deposition (Figure 1.4). In the majority of cases where a current is acting on sediment, the orientation of the κ_{max} axis is parallel to the flow direction (Taira, 1989) (Figure 2c). Other key AMS parameters are summarized in Table 2 in Appendix B.

AMS of the U1391 paleomagnetic cubes was measured on a Kappabridge KLY-4S in the palaeomagnetism laboratory at the University of Southampton. Susceptibility was measured in 64 different directions while the sample was slowly spinning. Declinations of each AMS axis were corrected using the vector-mean paleomagnetic declination of each core. This was calculated from natural remnant magnetization (NRM) measurements of the u-channels from the archive-half core sections, taking the mean of 12 AF demagnetization steps from 20 up to 90 mT (Xuan, pers. comm. 2019). U1391 cores relevant to this study are typically 9.5 m long covering a total of ~30 kyr (assuming a mean sedimentation rate of 27 cm/kyr), over which the geomagnetic field should approximate a geocentric axial dipole field with secular variations averaged out, giving an expected declination of 0° for Brunhes-aged sediments at the site. Therefore, the vector-mean NRM declination of each core provides an estimate of the rotation needed to restore the azimuthal orientation of the core relative to north. NRM declinations of some cores show an apparent along-core trend, indicating that the core has twisted during the coring process (e.g.,

Lanci et al., 2004). For cores with an apparent trend in NRM declinations, we estimate a linear trend line and calculate declination correction values for cube samples from the core based on their relative position within the core.

2.2.5 Physical Grain-Size Analysis

Physical grain size is well established as an indicator of paleocurrent speed variations (McCave et al., 1995, 2017). The size fraction 10–63 μm represents the sediment that is hydrodynamically sorted and therefore is most representative of current strength. The mean of this range is known as the sortable silt mean proxy (SS) and has been linked to flow speed (McCave et al., 1995, 2017).

Thirty-seven bulk samples from Site U1391 were weighed, treated with 0.2% sodium hexametaphosphate solution, left on a shaker table overnight to disaggregate, and then sieved at 106 μm. The samples were then washed with 10% HCl to remove carbonate minerals and calcareous microfossils. Physical grain-size sample processing often includes a biogenic silica removal step. Inspection of smear slides across a range of climatic intervals showed that biogenic silica is extremely scarce (<1%) in Site U1391 sediments, consistent with shipboard observations (Expedition 339 Scientists, 2013c). The biogenic silica removal step was therefore not included during sample processing. Physical grain-size distributions of the processed samples were measured using a Multisizer 3 Coulter Counter at the University of Cambridge Godwin Laboratory. Samples were suspended in an electrolyte solution, treated with 2 minutes of ultrasound, and stirred. The suspended material was then passed through an aperture of 200 μm where volume-related impedance changes are caused by displacement of the electrolyte as the grains pass through. Grain-size distribution was measured in log2 steps in the range between 5 and 100 μm for a total of 20,000 counts. Measurements for each sample were repeated at least three times and typically six times to increase statistical reliability.

2.3 Results and Discussion

2.3.1 Chronology and Sedimentation Rate

Our new XRF core-scan records from Site U1391 are presented and compared to data from Site U1385, Site MD01-2444, and the synthetic Greenland oxygen isotope record in Figure 2.1. Over most of the shared stratigraphy, the XRF records from Sites U1391 and U1385 are remarkably similar to one another, allowing detailed correlation, in particular between ln(Ca/Ti). In general,

ln(Ca/Ti) ratios from the two sites also show close similarity to an alkenone-based record of sea surface temperature from Site MD01-2444 on the Iberian Margin (Martrat et al., 2007).

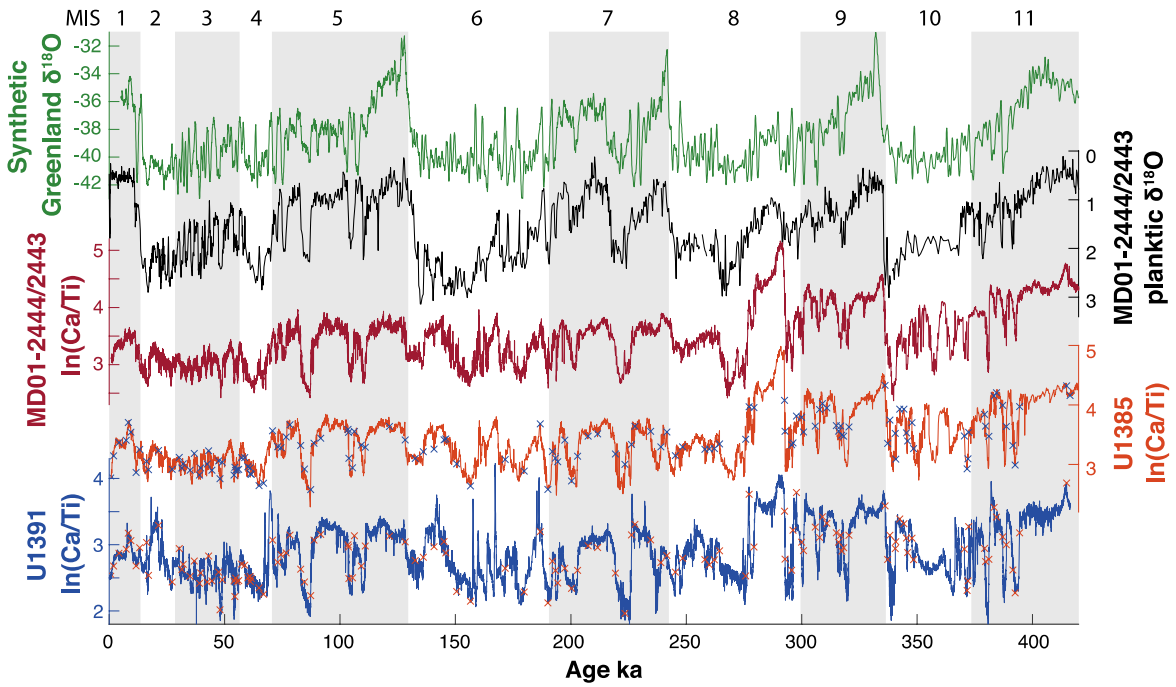

Figure 2.1. Records used to construct the U1391 age model, from top to bottom: synthetic Greenland $\delta^{18}O$ (Barker et al., 2011; green), MD01-2444/2443 planktic $\delta^{18}O$ (Hodell et al., 2013; black), and ln(Ca/Ti) (Hodell et al., 2013; red), U1385 ln(Ca/Ti) (Hodell et al., 2015; orange), and U1391 ln(Ca/Ti) (blue). Tie points between U1391 and U1385 ln(Ca/Ti) are shown in orange and blue crosses on each curve, respectively. Marine isotope stages are labelled across the top.

The chronology for Site U1391 was constructed by transferring the well-established age model from nearby Site U1385 (Hodell et al., 2015), using ln(Ca/Ti) as the correlation tool (Figure 2.1 and Table 1). Correlation of ln(Ca/Ti) between the two sites is mostly straightforward, except in the intervals 65–73, 140–190, and 348–380 ka, where the correlation is less clear. Planktic and benthic $\delta^{18}O$ records from Site U1391 (Guo et al., 2017) were placed on our constructed age model and compared with equivalent U1385 records (Hodell et al., 2015; Figure S1 in Appendix B). This figure confirms the robustness of our ln(Ca/Ti) correlation between Sites U1391 and U1385 because major climate transitions and much of the millennial scale variability documented in the $\delta^{18}O$ records are well aligned between the two sites.

The synthetic Greenland age model from Site U1385 was transferred to Site U1391 and is based upon the correlation of ln(Ca/Ti) at Site U1385 to the same parameters obtained from nearby piston Cores MD01-2444 and MD01-2443 (Hodell et al., 2015). Hodell et al. (2013) correlated sea surface temperatures and planktic $\delta^{18}O$ records at MD01-2444 and MD01-2443 to the synthetic

Greenland temperature record (Barker et al., 2011) (see Figure 2.1). The synthetic Greenland temperature record was constructed using a bipolar seesaw model prediction, making use of the relationship between Antarctic and Greenland temperature variations, and was chronologically tied to the absolutely dated Chinese speleothem record (Barker et al., 2011).

From 416 to 130 ka at Site U1391, the sedimentation rates at Site U1391 remain steady, at between ~28 and 30 cm/kyr (Figure 2.2). Between ~130 and ~50 ka the implied sedimentation rates increase steadily up to 39 cm/kyr before decreasing back to around 24 cm/kyr in the Holocene.

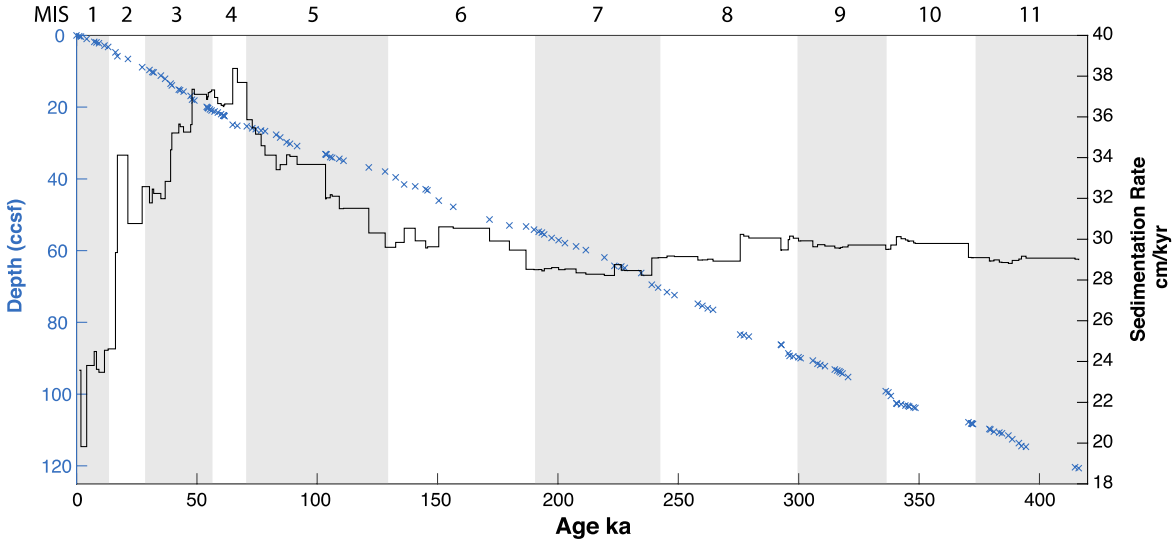

Figure 2.2. Age model and sedimentation rates of studied sediments from IODP Site U1391 showing the same depth-age tie points depicted in Figure 3.

2.3.2 AMS as a MOW Indicator at Site U1391

AMS parameters from Site U1391 cube samples, including κ_{max} declination, degree of anisotropy (P_j), and q values (see Table 2 for AMS parameters explanations), are shown in Figure 5. κ_{max} declination shows distinct behaviour throughout. Prior to ~130 ka, κ_{max} axes orientations show apparent glacial-interglacial variation, with the majority of the orientations grouped around the southeast during glacials, particularly between ~320 and 130 ka (Figure S2 in Appendix B). After ~130 ka, changes in κ_{max} declination became dominated by millennial-scale variability.

α_{95} values associated with the κ_{max} declination data are mostly less than 10° and are displayed in a histogram in Figure S3 (Appendix B). A lower hemisphere projection of κ_{max}, κ_{int}, and κ_{min} declination and inclination values from all samples is presented in Figure S4 (Appendix B). Throughout the record κ_{min} inclinations are predominantly clustered perpendicular to the horizontal with a mean value of 88.9° (Figure S4). κ_{max} declinations, across the entire studied

interval, are not only grouped to the southeast and northwest but also spread in directions between these two groups. Pj-T and q-β plots (Figures S5 and S6 in Appendix B), however, indicate that the fabric is mostly oblate and the sediments are likely current influenced. These Pj-T and q-β values indicating current activity are not restricted to certain κ_{max} declination directions. Influences such as a slope at the depositional site, coring, or sampling disturbance could have led to deviations in κ_{max} declination. It is also possible that downslope movement gave rise to more randomized directions in certain intervals, although this possibility is less likely according to the Pj-T and q-β plots (Figures S5 and S6). Furthermore, a stronger current may lead to grains deposited with a κ_{max} declination perpendicular to flow, though this is suggested to mainly occur in non-Newtonian fluids (Novak et al., 2014; Tauxe et al., 1998) and unlikely to be important at Site U1391 because the diagnostic behaviour of "streak-distributed" κ_{min} axes in the direction of flow on lower hemisphere projections (Park et al., 2013) is not observed.

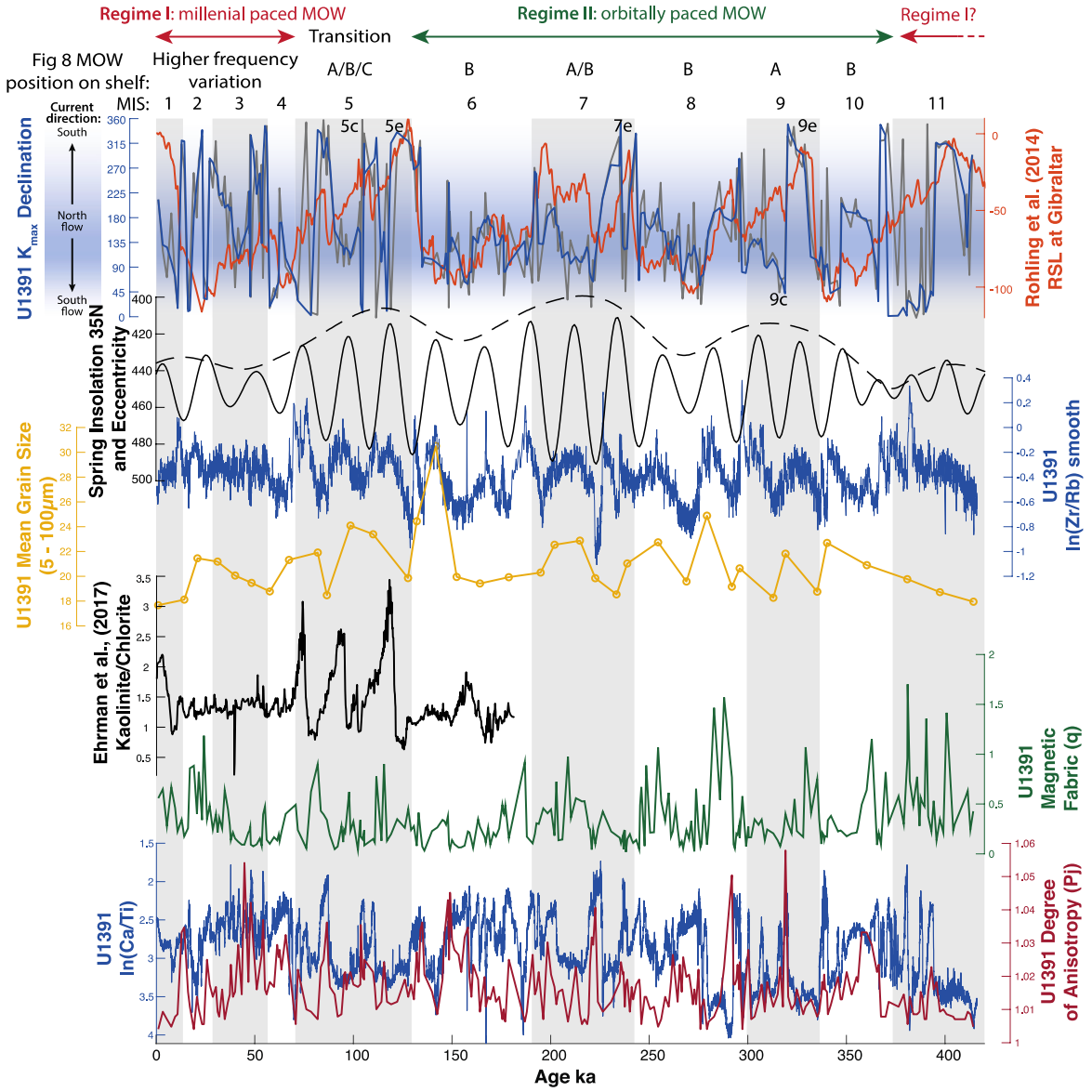

Figure 2.3. Two regimes of climate-induced Mediterranean Outflow behaviour on the West Iberian Margin during the late Pleistocene. From top to bottom: U1391 κ_{max} declination (grey . raw data; blue . 3-point moving average) and relative sea level at the Strait of Gibraltar (Rohling et al., 2014; orange), orbital eccentricity (dashed black), spring insolation at 35°N (solid black), U1391 ln(Zr/Rb) smoothed (3-point moving average) (blue), geometric mean physical grain size (yellow), eastern Mediterranean kaolinite/chlorite ratio (Ehrmann et al., 2017; black; higher values indicate drier North Africa), magnetic fabric q (green; higher values generally indicate stronger current), ln(Ca/Ti) (blue), and degree of anisotropy Pj (red). Blue shading in the top panel signifies declination values of κ_{max} data that indicate northward current flow at Site U1391.

Strong inverse correlation is observed between the degree of anisotropy (Pj) and ln(Ca/Ti) (Figure 2.3). Orbital scale variation in ln(Ca/Ti) is linked to dilution of carbonate by terrigenous input from

the shelf on the West Iberian Margin, while productivity changes largely reflect millennial scale variability (Hodell et al., 2013). Changes in Pj have been linked to both flow speed and delivered sediment composition (Yokokawa & Franz, 2002). Figure 2.3 shows that when Pj is low, the magnetic fabric, q, and physical grain-size proxies indicate stronger MOW. Given that ln(Ca/Ti) is high in these intervals, generally corresponding to a warmer climate (Figure 2.1), it is also likely there is a greater degree of bioturbation that may lower Pj. When Pj is high, lower ln(Ca/Ti) indicates a greater proportion of terrestrial input. Directional AMS data do not appear to have any relationship with the degree of anisotropy. We infer, therefore, that Pj at Site U1391 mainly represents the foliation of the sediment produced at times of higher terrestrial input, lower bioturbation, and slower flow, rather than a current-induced lineation.

From MISs 10 to 4, κ_{max} declination variability shows remarkable first-order correlation with relative sea level (Figure 2.3). During glacial interval MISs 6, 8, and 10, the majority of the κ_{max} declination values dip to the southeast, suggesting a predominantly northwest imbrication and therefore north-westward flow that is likely attributable to MOW (see Figure 2.3 and Figure 2.4). During most of interglacial MISs 5, 7e, 9a, 9e, and 11, however, κ_{max} declination is more scattered, with many samples in these intervals showing clear dips to the north suggesting a degree of southward imbrication (Figure 2.3 and Figure 2.4). This observation implies a less stable and possibly weaker southward flowing water mass over Site U1391 at these times than during glacials. Given changes in Atlantic vertical density structure and a less dense MOW during interglacials (Rogerson et al., 2012), MOW likely shoaled during these interglacial stages and may only have been active in water depths shallower than Site U1391. The water mass lying underneath MOW is the southward flowing, eastern NADW (ENADW). If the MOW shoaled during these interglacials it follows that ENADW also shoaled and/or expanded to influence sedimentation at Site U1391 at these times.

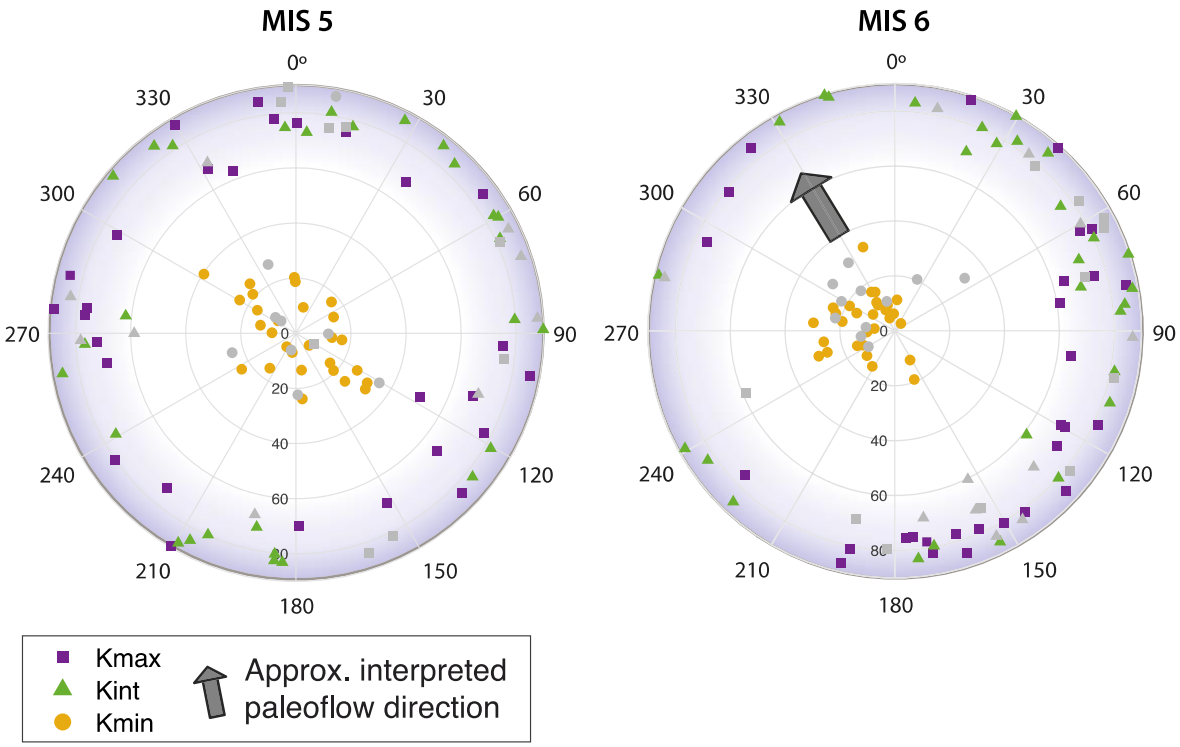

Figure 2.4. Example lower hemisphere projections of AMS κ_{max}, κ_{int}, and κ_{min} declination and inclination values at intervals of MOW presence (MIS 6) and absence in (MIS 5). MIS 5 κ_{max} and κ_{int} declinations are well scattered. However, during MIS 6, κ_{max} and κ_{int} show groupings to the southeast, indicating flow to the northwest.

2.3.3 Orbitally Paced MOW Influence at Site U1391 During MISs 10 to 4

The physical grain-size data show predominantly polymodal and moderately sorted distributions. The geometric mean grain size at Site U1391 is a coarse silt of ~20.8 µm, with the highest value of ~30.5 µm occurring at ~139 ka. Although these data are of relatively low temporal resolution, the mean values of grain size over time have similar patterns of variability to those documented in our high-resolution ln(Zr/Rb) data series (Figure 2.3). The positive correlation between mean physical grain size and ln(Zr/Rb) at Site U1391 (Figure 2.3 and Figure 4.1) suggests that ln(Zr/Rb) functions well here as a mean physical grain-size proxy, as discussed in section 4.4 and suggested elsewhere (Bahr et al., 2014; Rothwell et al., 2006). At Sites U1391 and U1385 ln(Zr/Rb) shows precession-paced variability between MISs 10 and 4, while in the absence of high-amplitude precession forcing, millennial-scale variabilities dominate in MIS 11 and MISs 3 to 1 (Figure 2.3 and Figure 2.5). After MIS 5, millennial-scale cold events (vertical grey bars in Figure 2.7) are marked by distinctly coarser sediments at Site U1385 compared to Site U1391.

The grain-size records from Sites U1391 and U1385 rule out a major influence by sea level-forced downslope movement. R^2 coefficients between Site U1391 ln(Zr/Rb) and downcore variation of each grain-size bin population are shown in Chapter 4, Figure 4.5. The ln(Zr/Rb) record correlates best with grain sizes ~30–70 µm, mostly in the sortable silt range, which is therefore more likely hydrodynamically sorted (MOW) material. The sortable silt proxy has been used previously on the Iberian Margin to identify paleocurrent changes (Hall & McCave, 2000). Finer sediments (grain sizes <~20 µm), on the other hand, which are more likely to be controlled by lower energy downslope transport, appear to be inversely correlated with the ln(Zr/Rb) data (Figure S8). Further evidence of current speed-controlled grain-size variability is found in the positive correlation between grain size and q values (magnetic fabric, see Table S1). q values tend to peak at precession maxima (Figure 5), indicating greater importance of shear stresses acting tangentially along the bed (i.e., a stronger current influencing deposition) at these times.

The clear precession signal in the ln(Zr/Rb) grain-size proxy (Figure 2.3 and Figure 2.5) from MISs 10 to 4 likely reflects changes in flow velocity at Site U1391 and points to the influence of circum-Mediterranean rainfall climate variability. Reductions in both winter and summer precipitation at insolation minima (Bosmans et al., 2015, 2020; Kutzbach et al., 2014; Trauth et al., 2009) likely contributed to increased LIW formation and outflow strength. The ln(Zr/Rb) proxy record of current speed shows remarkable alignment with changes in spring insolation at 35°N (Figure 2.3). This result suggests a stronger response of MOW to late winter/spring climate forcing of eastern Mediterranean hydrography at these timescales than to summer insolation.

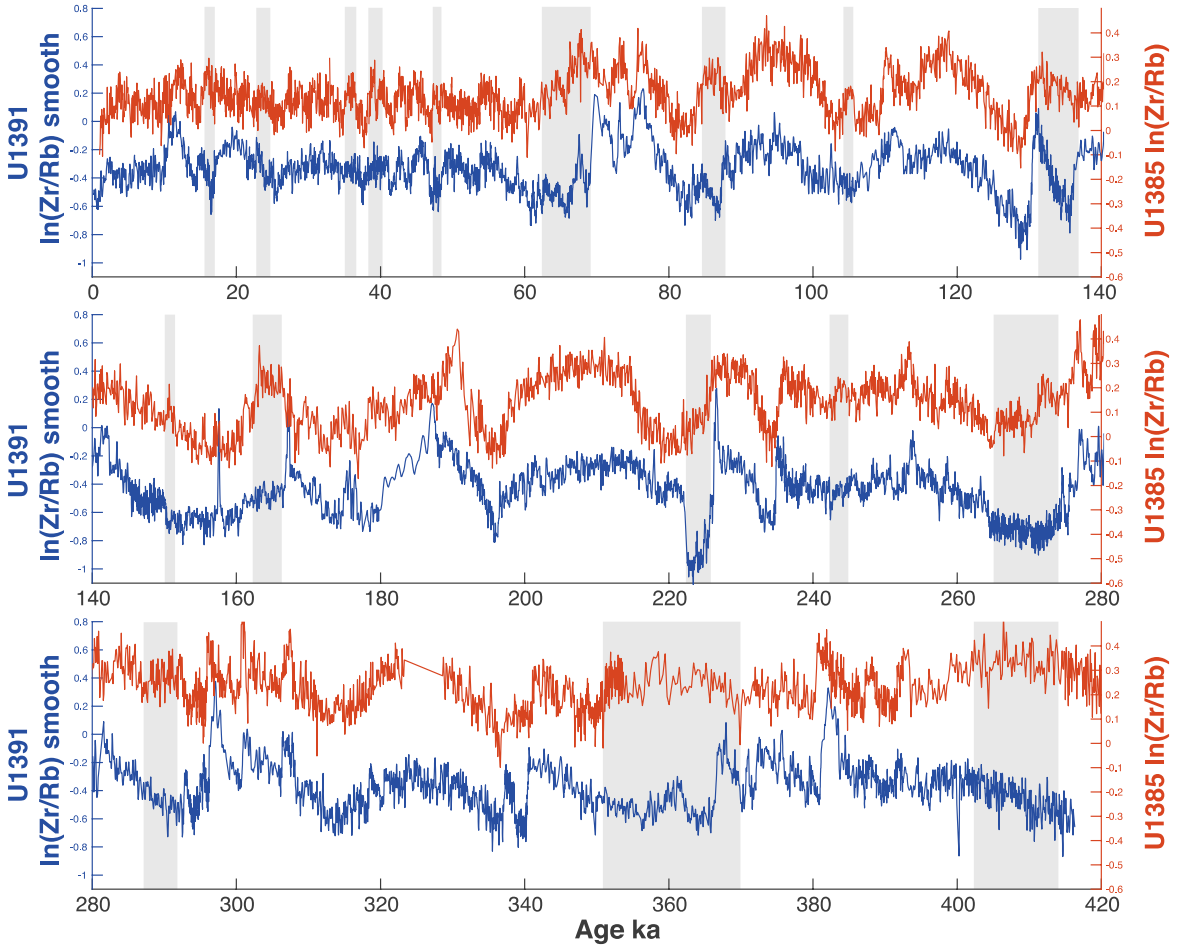

Figure 2.5. Detailed comparison of Site U1391 (3-point moving average) and U1385 ln(Zr/Rb) records. Gray vertical bars highlight the short intervals during which the two records are most discrepant.

Although Site U1385 lies below the expected depth of MOW influence, it records a pattern of ln(Zr/Rb) variability similar to that observed at Site U1391 (Figure 2.5). Additionally, the insolation forced grain-size pattern continues at both sites through MISs 5, 7, and 9, when the AMS κ_{max} declination data indicate that MOW had shoaled above Site U1391 (Figure 2.3). We infer that terrestrial sediments deposited on the West Iberian Margin (Hodell et al., 2013; Thomson et al., 1999) were hydrodynamically sorted by MOW in transit to sites below MOW (Figure 2.6). Similar hydrodynamic sorting effects on organic carbon transport have been inferred for a sediment core near the location of Site U1385 (Magill et al., 2018).

During the precession maximum between ~160 and 170 ka, mean physical grain size and ln(Zr/Rb) at Site U1391 do not coarsen as they do in previous precession cycles, while ln(Zr/Rb) at Site U1385 does coarsen (highlighted in Figure 2.5). Following the grain-size hydrodynamic sorting mechanism (Figure 2.6), it is inferred that MOW may have deepened below Site U1391 during this interval but still influenced grain size at Site U1385 through hydrodynamic sorting of terrestrial particles moving downslope to Site U1385. Notably, the κ_{max} declination does not vary greatly

during this time interval (Figure 2.3), possibly indicating a partial presence of MOW that is sufficient to orient the magnetic grains but not enough to hydrodynamically sort the grain size. Other intervals of different ln(Zr/Rb) behaviour, highlighted in Figure 2.5, tend to occur around cold events, suggesting that similar episodes of MOW deepening to depths below Site U1391 may have occurred many times during the last 416 ka.

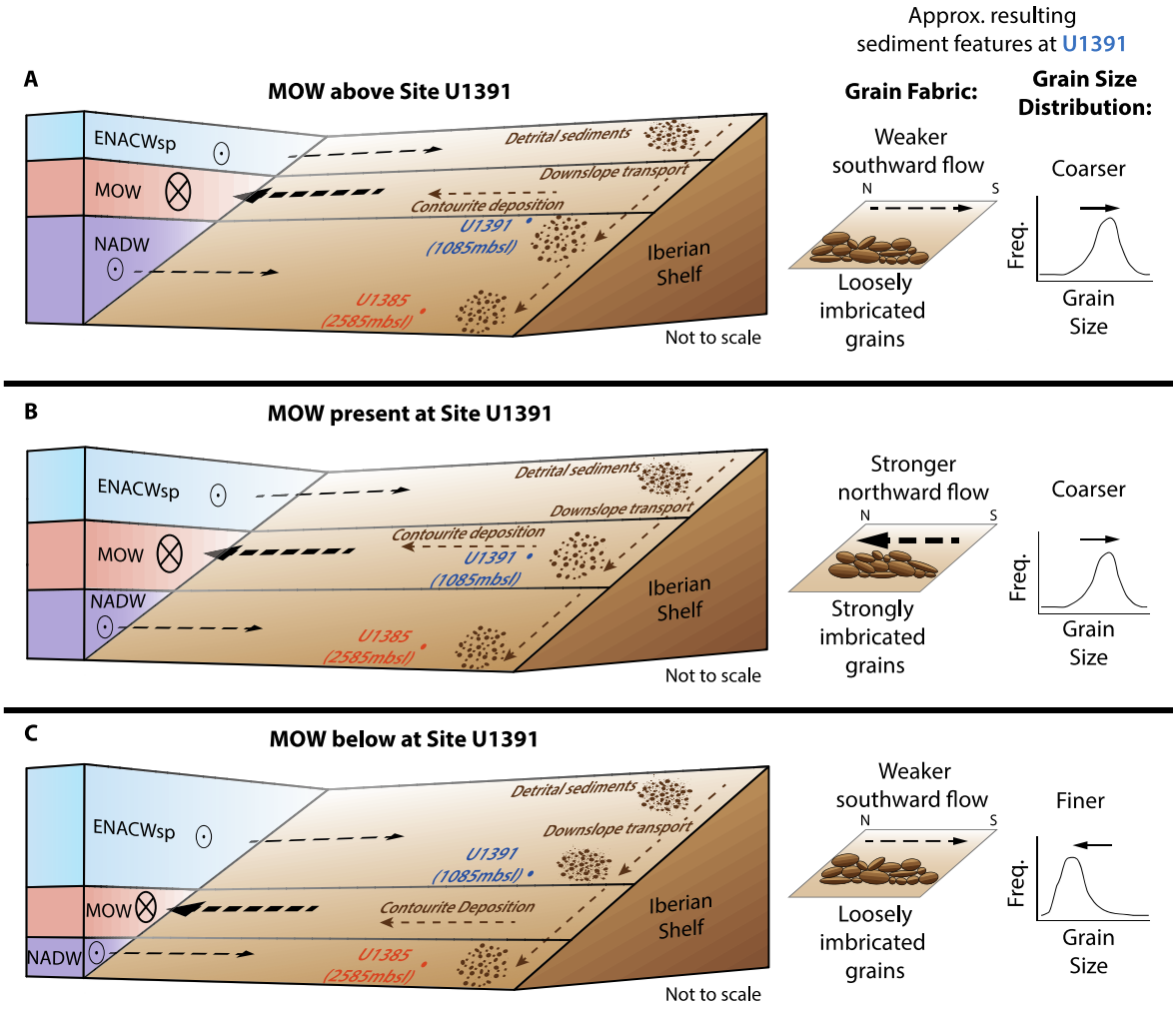

Figure 2.6. Schematic of inferred MOW vertical migration on the Iberian shelf to explain coeval grain-size variability at both Sites U1391 and U1385 and κ_{max} orientation changes at Site U1391. (a) MOW positioned above Site U1391 while NADW is present, resulting in grains that are weakly imbricated by southward flow. Mean physical grain size reflects MOW variability. (b) MOW present at Site U1391, resulting in grains that are more strongly imbricated reflecting fast northward flow. Mean physical grain size reflects MOW variability. (c) MOW positioned below Site U1391 while ENACWsp is present, meaning grains are weakly imbricated by a southward flow. Mean physical grain size does not reflect MOW variability. ENACWsp . Eastern North Atlantic Central Water subpolar; MOW . Mediterranean Outflow Water; NADW . North Atlantic Deep Water.

2.3.4 Two Distinct Regimes of MOW Behaviour on the West Iberian Margin

A first-order feature of the records is the strength of the orbitally paced (mainly precession) signals between MISs 10 and 4 (Section 4.4). From MIS 5 we see strong millennial-scale variability, which is initially superimposed on the orbital signal, but from MIS 3 to present, the millennial-scale signal dominates (Figure 2.3 and Figure 2.7). Thus, these records describe two regimes of temporal change and a transition interval between them. Regime I occurred from MIS 3 to present and during MIS 11. Regime II occurred between MIS 10 and MIS 5, inclusive. Through Regime II, MOW was orbitally paced and the average depth was shallower; it was present at Site U1391 during glacials and migrated above U1391 at peak interglacials. MOW behaviour then underwent a transition during MISs 5 and 4, when the influence of both orbital and millennial-scale forcing is documented and the MOW plume deepened on the West Iberian Margin. Regime I began around 60 ka; MOW was on average deeper, migrating below Site U1391 during stadials, and responded to millennial-scale variability more strongly, as recorded by both grain size and κ_{max} declination signals.

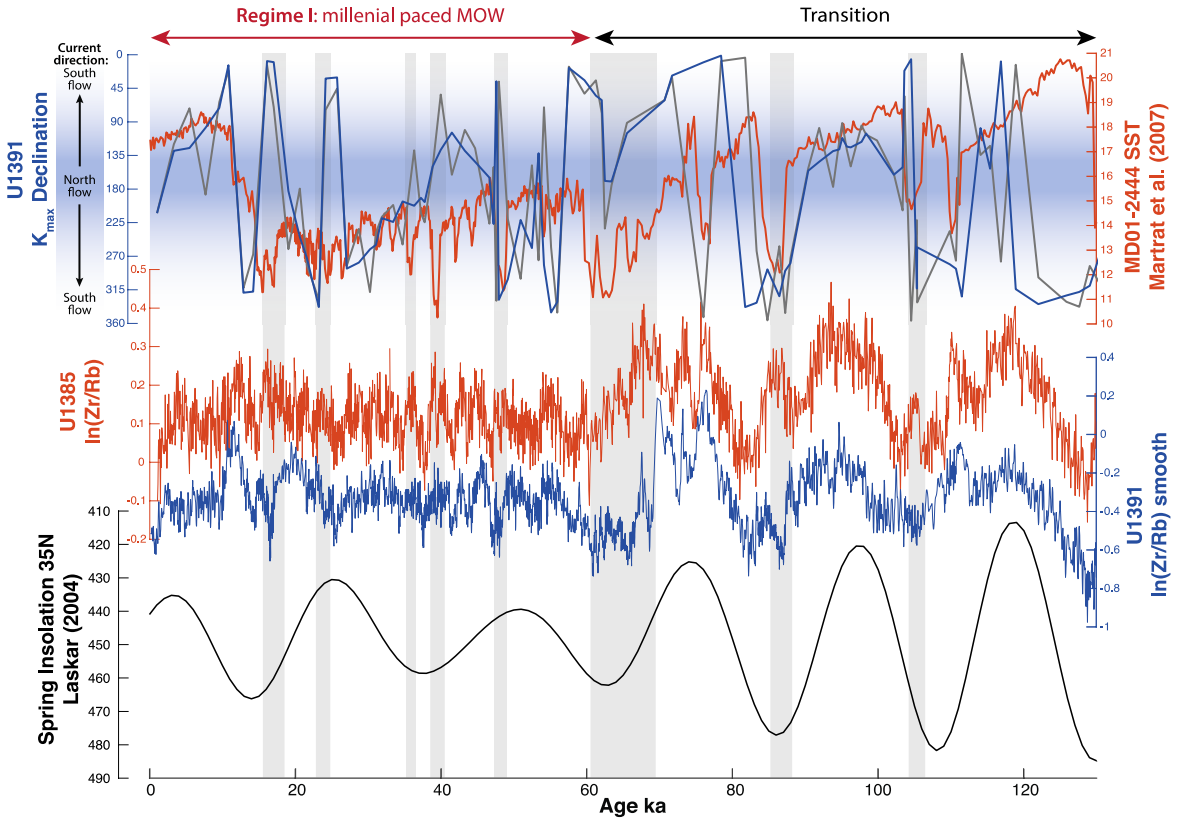

Figure 2.7. MOW variability during the transition interval and Regime I. From top to the bottom: U1391 κ_{max} declination (grey . raw; blue . 3-point moving average), MD01-2444 sea surface temperatures (Martrat et al., 2007; orange), ln(Zr/Rb) from Sites U1391 (blue) and U1385 (orange), and spring insolation at 35°N (Laskar, 2004; black). Cold

events are marked by grey bars. Note that y-axis direction of the κ_{max} declination is reversed compared with Figure 4.

The two distinct regimes interpreted here are consistent with the independently calculated sedimentation rate history of Site U1391 shown in Figure 2.2. When MOW is interpreted to either be present at or lie just above U1391 (Regime II), there is a steady sedimentation rate of ~29 cm/kyr. Sedimentation rates increase during the transition interval consistent with MOW movement to a deeper position on the West Iberian Margin, with an average position closer to U1391, focusing more deposition at the site. The subsequent decrease in sedimentation rate around 50 ka is consistent with MOW being frequently located below and therefore bypassing the site.

For the last ~130 ka, κ_{max} declination and sea surface temperature records show generally opposing behaviour, declination implying northward flow at Site U1391 during warm intervals before flipping to indicate southward flow during stadials. This relationship contrasts with the one documented for orbital forced insolation minima and maxima during the preceding ~235 kyr (Figure 2.3 and Figure 2.7). As illustrated in the ln(Zr/Rb) records in Figure 9, during the transition interval from ~130 to 60 ka, there is a strong imprint of millennial-scale events superimposed on the precession-paced grain-size cycles. From 60 ka, the precession signal disappears to produce a regime dominated by millennial change. During the latest ~106 kyr, ln(Zr/Rb) records from Sites U1385 and U1391 diverge from one another during cold stadials (vertical bars in Figure 2.7) but resemble one another more closely during warmer interstadials. During stadials we find coarser material at Site U1385 than at U1391, implying that the MOW plume depth is situated between the two sites, sorting the sediment that reaches U1385 but not significantly affecting U1391 grain sizes (Figure 2.6c and Figure 2.7). κ_{max} declinations at U1391 indicate southward flow at these times. We hypothesize that, in the transition interval, from ~130 to 60 ka, the average depth of MOW deepened on the West Iberian Margin to an arrangement wherein the main plume was present at Site U1391 during interstadials (Figure 2.6b) but deepened below the site during stadials (Figure 2.6c).

2.3.5 Driving Factors of the Distinct MOW Regimes

The overall structure of these records strongly suggests that the insolation response to amplitude modulation of precession by the 400 kyr eccentricity cycle exerts strong climatic control on MOW variability (Figure 2.3). Longer records are needed to verify this interpretation, but MOW Regime I is closely associated with the long-eccentricity node-induced minima in modulated precession

(MIS 11 and MISs 3 to 1), whereas Regime II occurs when amplitudes of the precession cycles are larger. This observation suggests a strong climate influence on MOW behaviour with some kind of hydroclimate control on the salinity of the Mediterranean a likely driving mechanism. Support for this interpretation comes from the strong correspondence in structure between our records for the last glacial cycle and the reconstruction of North African rainfall climate from an eastern Mediterranean site of Ehrmann et al. (2017). In this interpretation of our data, drier conditions from about 60 ka preconditioned eastern Mediterranean waters to produce a denser deeper-equilibrating MOW in Regime I compared to Regime II. Yet, while the close correspondence between the youngest portion of our data (the transition interval and Regime I) and the records of Ehrmann et al. (2017) imply a link to North African hydroclimate and therefore summer insolation change, the strong precession signal in our records for Regime II shows a particularly close relationship with changes in spring insolation (Figure 2.3). This observation raises the intriguing possibility that precipitation change associated with winter storm track activity (Bosmans et al., 2015, 2020; Kutzbach et al., 2014) may have exerted an important influence on Mediterranean hydrography and MOW behaviour during the late Pleistocene.

The data support the suggestion of Rogerson et al. (2012) that across glacial-interglacial timescales the North Atlantic vertical density structure was the primary control on the MOW plume settling depth. However, we propose that, on 400 kyr eccentricity timescales, circum-Mediterranean humidity and MOW density properties play a major role in controlling the equilibration depth of MOW in the Atlantic, via the eccentricity modulation of precession cycles.

MOW records from IODP Sites U1386 (water depth 561 m) and U1389 (water depth 644 m) in the Gulf of Cadiz (Figure 2.1), which extend to ~570 and ~250 ka, respectively, also show precession pacing and a change in behaviour between ~130 and 60 ka (Kaboth-Bahr et al., 2018; Kaboth et al., 2017). These phases and mechanisms fit well with our West Iberian Margin records of strength and depth changes of MOW. From ~130 ka to present, MOW was interpreted to be more active at Site U1386, as reflected in increased grain-size variability. An offset in benthic $\delta^{18}O$ values between Sites U1386 and ODP 967 was also observed. A greater proportion of western Mediterranean deep-water (WMDW) influence, and therefore greater density contrast across the Strait of Gibraltar and faster flowing MOW, was invoked to explain these observations (Kaboth et al., 2017). During the last glacial cycle (Regime I), greater aridity in northeast Africa compared to previous glacial-interglacial cycles (Ehrmann et al., 2017; Larrasoaña et al., 2003) and the resultant higher salinity surface waters in the eastern Mediterranean would have driven more vigorous production of LIW. In this scenario, LIW would have flowed over the WMDW more quickly (Figure 1.3), causing a greater proportion of it to be drawn over the Camarinal Sill by Bernoulli aspiration (Millot, 2009; Stommel et al., 1973). This would also have acted to increase the density of the

MOW, resulting in a generally lower settling depth on the west Iberian slope, as observed at Site U1391 during Regime I.

From ~475 to 130 ka, Site U1386 appears to show decreased MOW activity with a greater proportion of LIW influence compared to the interval after 130 ka (Kaboth et al., 2017). This interpretation is based on both a reduced gradient between U1386 benthic $\delta^{18}O$ values and those of the eastern Mediterranean ODP Site 967 and modest grain-size variability during this interval. This interpretation is broadly consistent with the shallower MOW regime that we document between ~365 and 130 ka on the West Iberian Margin. Compared with Regime I, the generally more humid conditions in northeast Africa (Larrasoaña et al., 2003) during Regime II would have resulted in a less dense, and therefore slower moving, eastern sourced MOW with a much smaller proportion of WMDW, as suggested by Kaboth et al. (2017). The generally lower density MOW would have resulted in the shallower MOW settling depths that we reconstruct on the West Iberian Margin during Regime II.

The observations presented here call into question the interpretations of Guo et al. (2017). MOW was interpreted to be more active at Site U1391 during interglacial intervals and weaker at glacial maxima, based upon the presence of certain MOW-sensitive species of benthic foraminifera. However, a reassessment of benthic assemblages is merited (García-Gallardo et al., 2017a, 2017b) because of evidence for downslope transport on the West Iberian Margin (Hall & McCave, 2000; Hodell et al., 2013; Thomson et al., 1999).

The records presented here clearly evidence strong climate-induced variability of MOW behaviour during the late Pleistocene on both astronomical (mainly precession) and millennial timescales. Analysis of the detailed mechanisms involved is beyond the scope of this contribution, but we find strong evidence suggesting that circum-Mediterranean rainfall climate change was a likely driver of MOW variability.

2.4 Conclusions

I present new records of MOW variability on the West Iberian Margin, documenting MOW behaviour back to MIS 11. Using the combination of AMS at Site U1391 and grain-size proxies at both Sites U1391 and U1385 allows the reconstruction of changes in MOW strength and depth. It is shown that AMS is a useful proxy for reconstructing current changes, mode of deposition, and migration of the MOW. Azimuth changes of the κ_{max} axis in conjunction with grain size and magnetic fabric indicate MOW presence/absence and flow speed change.

Two regimes of MOW behaviour are inferred, driven by insolation change in response to modulation of precession by the long (~400 kyr) eccentricity cycle. Strong precession-paced changes in MOW strength are documented between MISs 10 and 4 (Regime II). During this interval, interglacial peaks were marked by MOW shoaling to depths above Site U1391, indicated by the southward imbrication of magnetic grains caused by the underlying NADW at Site U1391. From MIS 5 we also see strong millennial-scale variability, which is initially superimposed on the orbital signal (defining the transition interval), but from MIS 3 to present and during MIS 11, the millennial scale signal dominates (Regime I).

These new records signal a generally less dense more shallowly equilibrating MOW in the North Atlantic between MISs 10 and 4, compared with MISs 3 to 1 and MIS 11. Thus, the impact of MOW on North Atlantic circulation and structure may well have evolved in ways not represented during the last glacial cycle. MOW's ability to enhance NADW formation and to help reinvigorate AMOC during cold-warm transitions may have been different in Regime II. Further investigation is merited of the forcing mechanisms involved, but the records clearly document strong climate-induced variability in MOW behaviour during the late Pleistocene and suggest that changes in rainfall climate in the circum-Mediterranean exerted an important control.

Chapter 3 Environmental Magnetic Investigations on West Iberian Margin Sediments: Provenance and Processes

3.1 Introduction to west Iberian Margin sediments

Marine sediments from the West Iberian Margin are key archives of orbital and millennial scale paleoclimate variability (Hodell et al., 2013) and high- and low-latitude forcing (Tzedakis et al., 2009; Voelker & de Abreu, 2011). Crucially, planktic and benthic oxygen isotope records in foraminifera from this region can be correlated to both the Greenland and Antarctic ice core records, respectively (Shackleton, Hall, & Vincent, 2000). High mean sedimentation rates (ranging between 10 -29 cm/kyr) are maintained through warm and cold intervals in the region (Hodell et al., 2015, Nichols et al., 2020). Furthermore, pollen records provide a link to changes in terrestrial European climate (Tzedakis et al., 2009, 2015). Most recently, it has also been shown that physical grain size variations from the region can be linked to changes in Mediterranean Outflow Water (MOW) and, by inference, precipitation changes over the circum-Mediterranean (Nichols et al., 2020).

Previous work on environmental magnetism in late Pleistocene sediments on the west Iberian has focussed on sediments from deep water sites (> ~2000 mbsl) and found close links between magnetic parameters of the sediments and northern high latitude variability (Channell et al., 2013; Moreno et al., 2002). In those studies, concentrations of fine-grained magnetite were observed to vary closely with oscillations between warm and cold events. Two opposing hypotheses have been presented for the cause of magnetic grain size variations. Deep sea transport of magnetite from the North Atlantic was suggested by Moreno et al (2002) whereas Channell et al (2013) found evidence of sea-level controlled dilution of the concentration of magnetotactic bacteria by terrigenous input from the Iberian slope.

Variations in concentration of haematite on the west Iberian Margin have been hypothetically linked to aeolian transport of dust from North Africa (Channell et al., 2013; Hodell et al., 2013). The s-ratio and a* (ratio of red to green wavelengths of light reflected from sediment surface), both interpreted as indicating haematite concentration, show strong insolation control with enhanced input during stadials and glacials (Channell et al., 2013; Hodell et al., 2013). It has however, not yet been confirmed if North Africa is the source of this haematite as riverine input cannot be ruled out.

Ice-rafted debris (IRD) are coarse lithic material deposited in layers throughout large regions of the North Atlantic as a result of iceberg discharge from northern hemisphere ice-sheets (Bond et al., 1999; Heinrich, 1988). IRD is often strongly associated with millennial scale cooling events known as Heinrich Events where there is a large slowdown in Atlantic meridional overturning circulation (AMOC), strong regional cooling and a southward shift of the polar front. The relationship between AMOC and Heinrich and other IRD events has been the subject of intense debate with questions concerning what the root cause of the rapid initiation is and then the recovery and the extent of the southward migration of the polar front (Barker et al., 2015; Bond et al., 1999). To further understand the origin and nature of IRD events, correlation of IRD layers across the North Atlantic is an important exercise. IRD can often be identified by large peaks in magnetic susceptibility in North Atlantic sediments (Kissel, 2005; Stoner et al., 1996) as well as XRF ratios ln(Si/Sr) and ln(Sr/Ca) and the wet bulk density of the sediment (Channell et al., 2012; Hodell et al., 2008). IRD has been identified in previous environmental magnetic studies of deep (>~2500 mbsl) sediments from the Iberian Margin (Channell et al., 2013; Moreno et al., 2002; Thouveny et al., 2000).

Here the two competing hypotheses on the forcing of magnetic grain size changes are tested by determining the nature of magnetic grain size changes at IODP Site U1391, which lies in shallower water (~1085 mbsl) and is therefore less strongly influenced by deep sea sediment transport from the North Atlantic. I also use environmental magnetic methods to investigate (i) variations in the concentration of haematite and (ii) ice-rafted debris (IRD) on the west Iberian Margin to test the suggestion that haematite supply is controlled by aeolian transport of dust from North Africa or riverine input from the Iberian margin (Channell et al., 2013; Hodell et al., 2013) and to understand of AMOC behaviour and the migration of the polar front on millennial timescales in the Northeast Atlantic.

3.2 Materials and Methods

3.2.1 U-channel and bulk sediment samples from IODP Site U1391

This study focusses on IODP Site U1391, situated on the west Iberian Margin at a water depth of 1085 mbsl, drilled during IODP Expedition 339 (Mediterranean Outflow) (Expedition 339 Scientists, 2013). A total of 106 continuous u-channel samples were collected from Site U1391 for palaeomagnetism and environmental magnetism studies. Sampling of the u-channels followed the shipboard splice derived from Holes U1391A and U1391B (Expedition 339 Scientists, 2013c).

All u-channel samples were taken from the centre of the archive half-core sections to avoid disturbed or contaminated core margins that can influence the quality of paleomagnetic and environmental magnetic records. Sediments in each u-channel sample are enclosed in plastic containers of the same length as the core-section (typically ~150 cm) and an internal cross section of ~1.8 x 1.9 cm^2, with a clip-on plastic cover that seals the sediments to minimize dehydration (Tauxe et al., 1983). The collected u-channel samples cover a continuous sediment sequence between 0-120.62 m CCSF-A at IODP Site U1391.

During u-channel sampling, excess sediment along the outside walls of the u-channel containers were collected in plastic bags. These scrapings represent an average bulk sediment sample of the core-sections from which the u-channels were taken. Discrete bulk sediment samples were also collected from 27 depth levels with representative lithology and/or characteristic environmental magnetic behaviour.

3.2.2 Environmental magnetic measurements on u-channel samples

Natural remnant magnetization (NRM) of the u-channel samples were first measured on a 2G Enterprises liquid helium-cooled pass-through superconducting rock magnetometer (SRM) at the University of Southampton. NRM data were collected before and after stepwise alternating field (AF) demagnetisation and are reported separately (Xuan and Nichols et al., in preparation). Following NRM measurements, volume magnetic susceptibility of the u-channel samples was measured at 1 cm intervals on a susceptibility track at the University of Southampton equipped with a Bartington MS3 meter and 42-mm diameter MS2C sensor loop. Measurements for each u-channel were repeated at least twice and up to four times to verify and produce reliable results that are less affected by drift.

The u-channel samples were subsequently used for rock magnetic analyses. Anhysteretic remnant magnetisation (ARM) was imparted in a 100-mT peak AF and a 50-µT direct current (DC) bias field along the long-axis of each u-channel. The acquired ARM was measured prior to demagnetisation and after stepwise AF demagnetisation with peak fields of 10, 20, 25, 30, 35, 40, 45, 50, 55, 60, 70, 80 and 100 mT. After completion of ARM experiments, isothermal remnant magnetisation (IRM) was imparted to the samples in a 300 mT field (IRM_{300mT}) and then a 950 mT field ($IRM_{950\ mT}$). $IRM_{300\ mT}$ were measured before and after stepwise AF demagnetisation with peak fields of 10, 15, 20, 25, 30, 40, 50, 60, 70 and 100 mT, and $IRM_{950\ mT}$ were measured before demagnetisation and after 30 mT AF demagnetisation. $IRM_{950\ mT}$ measured before demagnetisation is used as saturation IRM (SIRM) in this study. Subsequently backfield IRM was applied to the samples in 100 mT ($IRM_{-100\ mT}$) and then 300 mT ($IRM_{-300\ mT}$) fields that are in the opposite direction to that of the $IRM_{950\ mT}$.

$IRM_{-100\ mT}$ was measured on the SRM without any treatment and $IRM_{-300\ mT}$ was measured before and after 30 mT AF demagnetisation.

ARM and IRM measurements were made on the same SRM at the University of Southampton used for NRM analyses. The SRM has a narrow sample access bore (4.2-cm diameter) designed for u-channel measurements and is housed inside a magnetically shielded room. Similar to NRM, ARM and IRM measurements for each u-channel were made at 1-cm intervals over the sample length as well as over a 10-cm "leader" interval before the sample and a 10-cm "trailer" interval after the sample. The "leader" and "trailer" measurements serve the dual functions of monitoring the measurement background and allowing for future signal deconvolution (Oda & Xuan, 2014; Xuan & Oda, 2015). The UPmag software (Xuan & Channell, 2009) was used to correct any flux jumps and spike noises in SRM measurements.

3.2.3 X-ray fluorescence

X-ray fluorescence (XRF) data was collected on Site U1391 u-channels at 1 cm resolution, further details of the method can be found in chapter 2 (Nichols et al., 2020). The log ratio of Fe (XRF counts) to magnetic susceptibility, $\ln(Fe/\kappa)$, compares semi-quantitative counts of Fe with how much that Fe is contributing to the bulk magnetic susceptibility and has been suggested as a proxy for reductive diagenesis (Funk et al., 2003a, 2003b; Itambi et al., 2009). This ratio is typically constant for sediments unaffected by diagenetic processes and is dependent on the source material. When reductive diagenesis affects the sediment, depletion of ferric minerals leads to a significant reduction in magnetic susceptibility and an associated increase in $\ln(Fe/\kappa)$ (Funk et al., 2003a). A high proportion of sulphur relative to iron, Fe/S, can be indicative of reducing conditions and reductive diagenesis as this process produces iron sulphide minerals (Sluijs et al., 2009). As diagenesis is often associated with elevated levels of organic matter it is useful to combine these reductive diagenesis ratios with proxies sensitive to concentration of organic material. Levels of organic matter can be associated with the Br/Ti ratio, as Br is concentrated by organisms (e.g. (Ziegler et al., 2008).

3.2.4 Rock magnetic experiments on bulk samples

U-channel scrapings and the 27 bulk sediment samples were used for rock magnetic experiments on a Princeton Measurements Corp. (now Lakeshore Inc.) Model 3900 vibrating sample magnetometer (VSM) at the University of Southampton. The weight of samples used for all analyses on the VSM was measured and used to normalize the measurement data.

Hysteresis loops for the samples were measured using applied fields ranging between -0.5 T and +0.5 T with steps of 4 mT and averaging time of 500 ms. For backfield experiments on the same samples, a 0.5 T field was first applied to the samples, remanence of the samples was then monitored after applying (and turning off) an increasing field (with a 5-mT increment) in the opposite direction until zero remanence was reached. Hysteresis loop data were processed, and slope corrected following the procedures of Jackson and Solheid (2010) and using the HystLab program (Paterson et al., 2018). The slope corrected hysteresis loop data and backfield curves were used to determine ratios of hysteresis parameters: Mr/Ms and Bcr/Bc, where Mr is saturation remanence, Ms is saturation magnetization, Bcr is coercivity of remanence, and Bc is coercivity. The ratio of Bcr/Bc plotted against Ms/Mr in a Day Plot is a widely used technique for determining the domain state of the bulk mineralogy (Day et al., 1977).

Scrapings and bulk samples were also used for IRM acquisition experiments on the VSM. IRM of the samples were acquired and measured (using an averaging time of 500 ms) at 100 field steps on a logarithmic scale ranging from 0.1 mT to 500 mT. Decomposition of the gradient for IRM acquisition data were calculated using IRMunmix software (Heslop et al., 2002). In addition, a total of 11 selected bulk samples were used for first order reversal curve (FORC) measurements (Pike et al., 1999; Roberts et al., 2014; Roberts et al., 2000) on the VSM. The FORC diagrams consist of 173 curves collected at 1.5 mT field increments with an averaging time of 200 ms. FORC measurement data were analysed using the FORCinel software (Harrison & Feinberg, 2008), which incorporates VARIFORC smoothing (Egli, 2013) and statistical confidence intervals (Heslop & Roberts, 2012).

Susceptibility versus temperature (κ-T) curves, generated using an AGICO Corporation susceptibility meter (KLY-4S with a CS3 furnace) at the University of Southampton, were measured for 11 samples at heating and cooling rates of ~11 °C/min. Susceptibility was measured at evenly spaced intervals from room temperature up to 700 °C and then cooled back to 50 °C in an Argon atmosphere. Two samples had separate subsamples taken and were measured in air during heating and cooling.

3.3 Results and Discussion

3.3.1 Continuous environmental magnetic records from Site U1391 sediments

Environmental magnetic data collected on u-channel samples have been placed on age according to the chronology described in Chapter 2 and Nichols et al. (2020). This age model was

constructed by correlating ln(Ca/Ti) data acquired from x-ray fluorescence (XRF) scans of Site U1391 sediments to those from the nearby Site U1385, and transferring the Synthetic Greenland age model from Site U1385 (Hodell et al. (2015)). Tie points used for transferring the age model and estimated sedimentation rates changes at Site U1391 are shown in Figure 2.1 in Chapter 2 (Nichols et al., 2020).

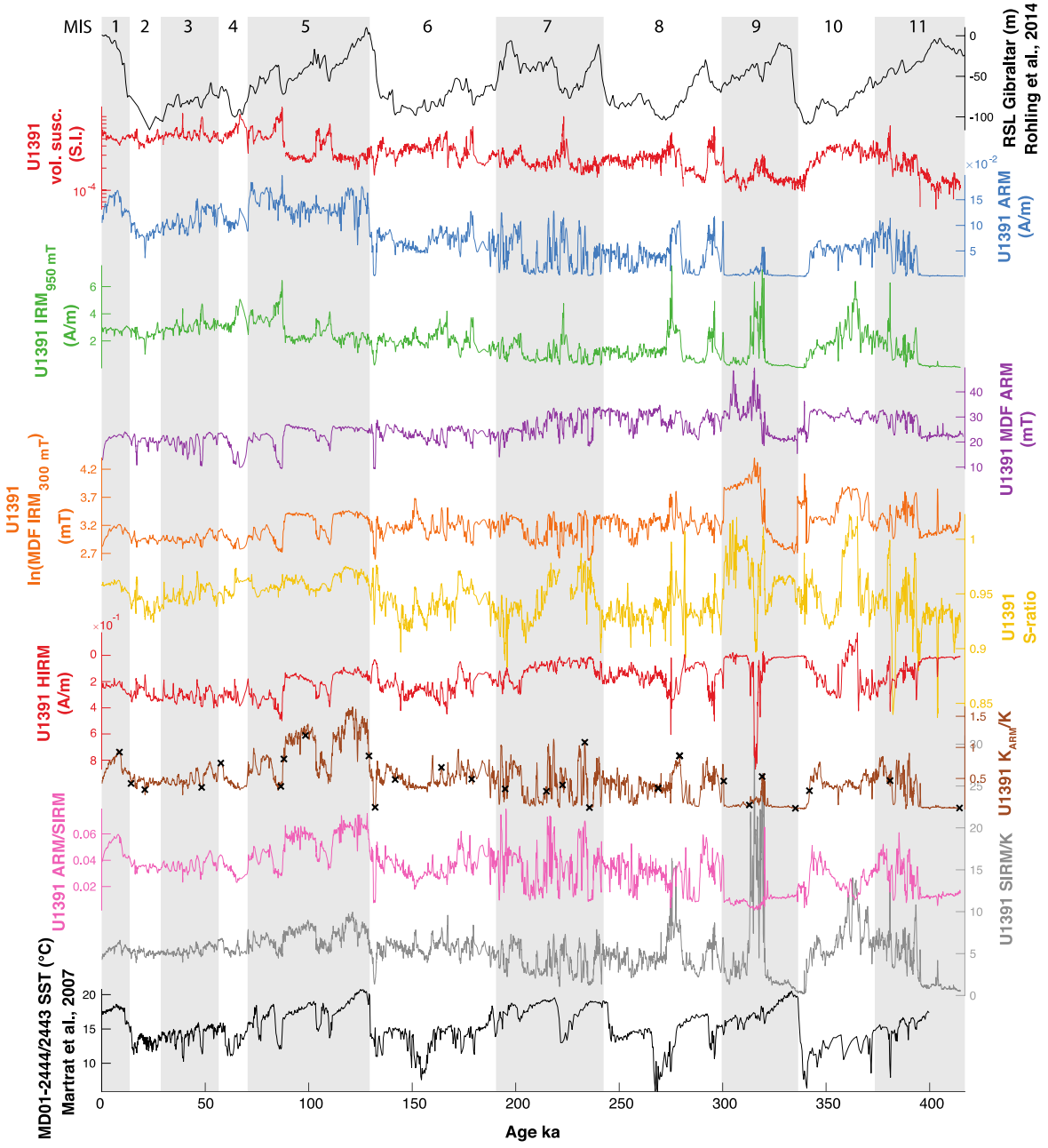

Figure 3.1. Environmental magnetic parameters at Site U1391 with climate record comparisons. From top to bottom: Relative sea level (RSL) at the Straits of Gibraltar (Rohling et al., 2014), magnetic susceptibility (log scale), ARM, $IRM_{950\,mT}$, Median destruction field (MDF) of ARM, MDF of $IRM_{300\,mT}$ (log scale), S-ratio (log scale), HIRM, κ_{ARM}/κ ,

ARM/IRM, SIRM/κ and sea surface temperature at Sites MD01-2444/2443 on the west Iberian Margin (Martrat et al., 2007). Black crosses indicate where rock magnetic measurements have been made, and vertical grey bars represent interglacial marine isotope stages (MIS).

Figure 3.1 shows the measured magnetic concentration parameters of Site U1391 sediments including volume normalised susceptibility, ARM and $IRM_{300\,mT}$ compared with the calculated environmental parameters (i.e., MDF of ARM, s-ratio, κ_{ARM}/κ, ARM/SIRM and SIRM/κ). Relative sea level (RSL) (Rohling et al., 2014) and sea surface temperature (SST) (Martrat et al., 2007) are displayed for comparison. A clear distinction in behaviour of environmental magnetic parameters is observed prior to and after ~130 ka (Figure 3.1). Through the latest ~130 kyr, concentrations of magnetic materials and particularly variations of environmental magnetic ratios closely follow millennial scale climate variability of Iberian Margin sea surface temperature and relative sea level, with higher concentrations seen at colder intervals. This observation is in agreement with findings from environmental magnetic studies conducted on sedimentary records from deeper sites on the west Iberian Margin (Channell et al., 2013; Moreno et al., 2002). Unlike the sediments from the deeper sites however, Site U1391 environmental magnetic records show higher frequency variability and less direct links with climate signals prior to ~130 ka. In addition, magnetic concentration parameters show minima during warm intervals, MIS 7e, 9 and 11. At warm intervals in MIS 5 the consistent high levels of MDF of ARM and $IRM_{300\,mT}$ indicate a high proportion of biogenic magnetite contributing to the remanence.

Prior to ~130 ka, generally higher MDF ARM and lower S-ratios suggest presence of a higher coercivity component, particularly at intervals where concentrations of magnetic material are low (Figure 3.1). The κ_{ARM}/κ record also shows significant alteration prior to ~130 ka, particularly at warmer intervals MIS 7e, 9 and 11 where magnetic grain sizes appear very coarse. This alteration at warmer intervals suggests the higher coercivity component could have resulted from diagenesis related processes, associated with oxygen removal by increased respiration by organic matter (see Section 3.3.3 below). Below sediments dating ~230 ka , shipboard visual core descriptions describe locally occurring pyritised burrows and shell fragments black specks (sulphide), indicating sulphidic mineral diagenesis has occurred. As this diagenesis is not seen deeper on the Iberian margin (Channell et al., 2013; Moreno et al., 2002) in sediments with similar age, or more recently at Site U1391, it is possible that these conditions result from a combination of increased productivity at warm intervals combined with vertical migration of the Mediterranean outflow water and associated changes in sedimentation rate and bottom water ventilation at the shallower Site U1391 (see further discussion in Section 3.3.3).

Magnetic grain size proxies κ_{ARM}/κ, ARM/SIRM, SIRM/κ, and composition parameters MDF of $IRM_{300\,mT}$ show strong similarity during the last ~130 kyrs (Figure 3.1), suggesting that majority of variability in bulk magnetic properties of Site U1391 sediments during this time are driven by grain size changes rather than mineralogy. Where MDF of $IRM_{300\,mT}$ increases above κ_{ARM}/κ (~67 – 64 ka, ~158 – 148 ka, ~280 – 272 ka, ~320 – 300 ka and 366 – 350 ka), SIRM/κ also tends to increase, indicating that reductive diagenesis may be affecting grain size and causing increases in coercivity. High SIRM/κ, relative to κ_{ARM}/κ and ARM/IRM (signifying that the increase may not be related to grain size), may also indicate increased concentrations of iron sulphides such as greigite (Fe_3S_4) (Roberts, 1995). However, during the κ-T experiments (Figure 3.2) no significant drop on the heating curve in magnetic susceptibility is observed between 270 and 350 °C (Roberts, 1995), indicating that iron sulphides are likely only a minor phase.

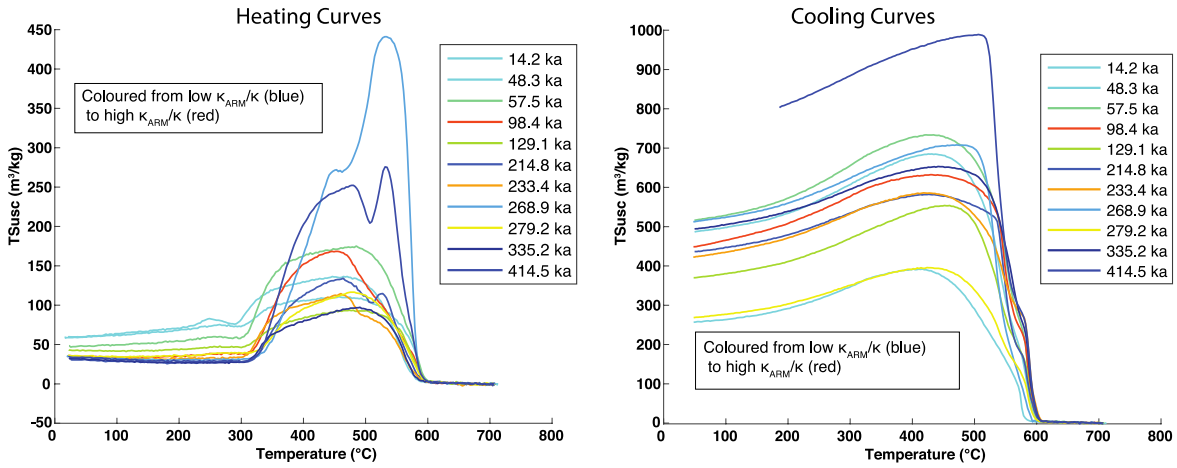

Figure 3.2. High temperature magnetic susceptibility heating (left) and cooling (right) curves. Colours indicate κ_{ARM}/κ values from high (fine grained) in red to low (coarse grained) in blue.

3.3.2 Magnetic phases of Site U1391 sediments

Decomposition of the gradient for IRM acquisition data acquired on representative samples are shown in Figure 3.3. Up to four different magnetic components were used to fit the IRM gradient data. Biogenic magnetite has been shown to be a significant magnetic component on the Iberian margin (Channell et al., 2013) and detrital sources at Site U1391 likely include the shelf, MOW and aeolian transport.

For samples dated between 130 ka to present, gradients of IRM acquisition curves from warm intervals show little to no significant contribution of high coercivity materials (>~150 mT), with unmixing revealing three or less low coercivity components being dominant (Figure 3.3a).

Magnetic components 1, 2 and 3 are shown in Figure 3A with purple, yellow and orange dashed lines, respectively. Component 1 (purple) has a mean coercivity of ~46 mT, dispersion parameter (DP) of 0.25 and contributes to just over half the total remanence. Component 2 (yellow) contributes ~24% of the total remanence, has a DP of 0.33 and a mean coercivity of ~17 mT. Similar to the component 1, component 3 (orange) also has a mean coercivity of ~46 mT but with a much wider dispersion parameter (DP) at 0.52 and contributes to just ~ 20% of the total remanence.

The characteristics of these three components fit with different forms of detrital magnetite. The relatively high coercivity of component 1 could be due to some reduction of the outer shell of the original magnetic grains leaving a finer, higher coercivity, core. Component 2 is likely multi-domain detrital magnetite due to the low coercivity and the high DP indicates a wide range of grain sizes. Component 3 may also be detrital magnetite with a greater range of grain sizes, indicating that it could be from a different source to component 1.

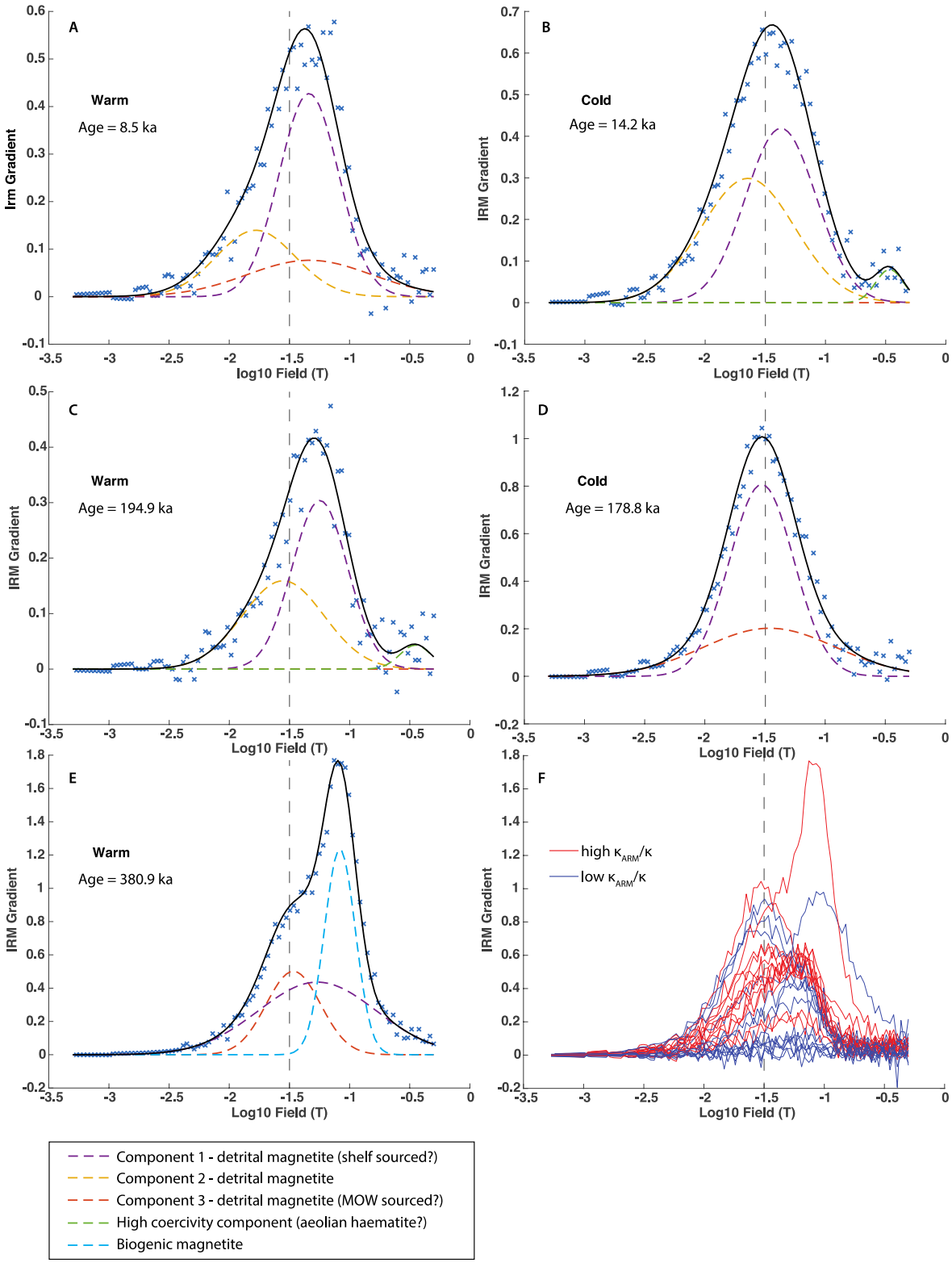

Figure 3.3. IRM acquisition gradients, and their decomposition into separate components, from different climate intervals. A) and B) Typical results from warm and cold intervals after ~130 ka. C to E) Results from before ~130 ka. F) Stacked IRM acquisition derivatives. κ_{ARM}/κ colour determined by whether or not a sample falls above or below the median κ_{ARM}/κ value. Dashed vertical grey lines are at 31.6 mT for reference.

At cold intervals after 130 ka, components 1 and 2 are similar to the warm intervals (Figure 3.3B). However, component 3 is not observed. As the MOW has been interpreted to be absent from U1391 during stadials of the last 130 ka (see Nichols et al., 2020), component 3 may represent magnetite that is transported and sorted by MOW. Additionally, at some of these cold intervals a higher coercivity component is present which has a mean coercivity of ~300 mT (Figure 3B). This is often accompanied by apparent shifts in S-ratio to lower values (see Figure 3.1). North Africa was drier and produced greater quantities of aeolian dust at stadials (e.g., Grant et al., 2017; Larrasoaña et al., 2003; Trauth et al., 2009). This high coercivity component therefore may be aeolian haematite sourced from North Africa.

Samples from glacial intervals before 130 ka (Figure 3.3D) tend to show two components, without the higher coercivity component seen after 130 ka. The two components reflect components 1 and 2 from after 130 ka, having similar mean coercivities to each other and a similar difference in DP and relative contribution. The mean coercivities however, are slightly lower than those from after 130 ka, at ~32 mT, possibly reflecting marginally enhanced background levels of diagenesis before 130 ka, relative to after, that has removed some of the finest magnetite. Warm intervals before 130 ka show variable behaviour; many have much weaker remanence resulting in IRM acquisition data with high noise levels (Figure 3.3F), likely from enhanced levels of reductive diagenesis, while some also show evidence of a high coercivity component (mean ~350 mT) such as at 195 ka (Figure 3.3C). The peak with strong remanence at 381 ka with a peak gradient of ~1.7 (Figure 3.3E), could be a hard biogenic magnetite, this is common throughout the record shown by many of the samples in Figure 3.3F showing a strong peak at a similar coercivity. These results therefore represent a combined effect of a wide range of factors with varying contribution through time including sediment source/transportation and degrees of diagenesis.

The narrow and uniform nature of many of the hysteresis loops indicate that magnetic content in the sediments are dominated by low coercivity magnetic minerals (Figure 3.4). After 130 ka, hysteresis loop shapes are generally similar however, warm intervals show lower Ms compared to cold, in agreement with IRM acquisition observations. Before 130 ka, hysteresis loop shapes are more variable, again consistent with observations made on IRM acquisition results. Figure 3.4C shows a sample containing biogenic magnetite.

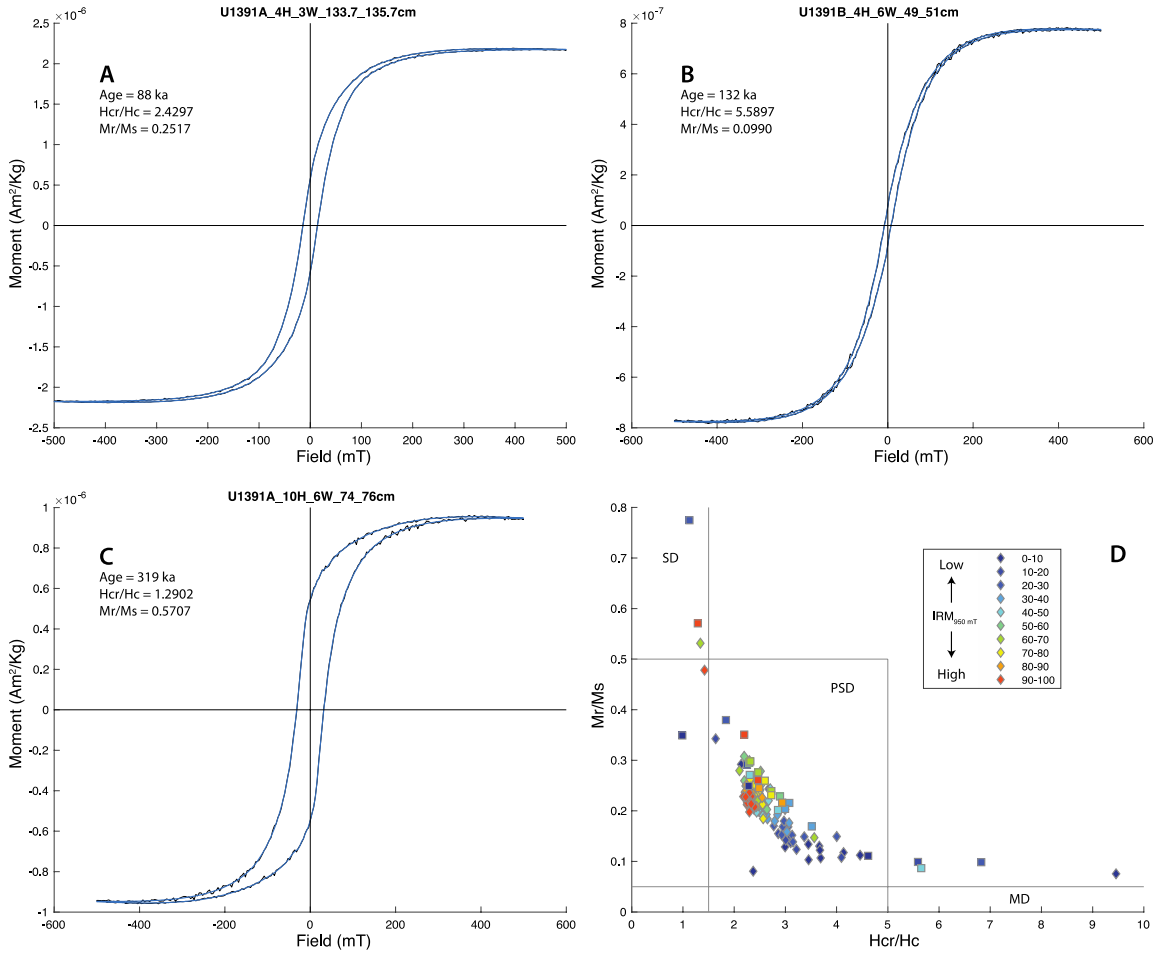

Figure 3.4. Hysteresis loops (A to C) showing range of typical behaviours seen in U1391 sediments. D) Day Plot coloured by $IRM_{950\,mT}$ values (high (red) to low (blue)).

The Day Plot in Figure 3.4 shows results from both u-channel scraping (diamond markers) and discrete samples (square markers). Plotted data points are coloured according to $IRM_{950\,mT}$ values of corresponding samples. Results from majority of the samples fall within the pseudo-single-domain (PSD) region, with notable exceptions lie at both extremes of the curve. Samples that fall closer to the single-domain (SD) and multi-domain (MD) regions tend to have higher and lower IRM values, respectively. Results falling outside the SD, PSD or MD regions could be due to higher noise levels in these measurements.

The magnetic susceptibility of 11 samples monitored on heating and cooling are shown in Figure 3.2. Across all the κ-T results, there is a significant drop in magnetic susceptibility near ~580 °C, the curie temperature of magnetite; consistent with a dominant low coercivity magnetic phase indicated by hysteresis and IRM acquisition data. The initiation of reductions in susceptibility seen in some samples (at 214.8, 233.4 and 414.5 ka) during heating from ~450 to 500 °C may be indicative of the presence of titanomagnetite, as increasing titanium concentrations in titanomagnetite reduces the curie temperature below that of magnetite. Titanomagnetite could be formed during heating between ~300-450°C or they could be original detrital component.

Channell et al., (2013) found detrital titanomagnetite deeper on the west Iberian Margin at MD01-2444, through a combination of EDS and the techniques used here. It is therefore likely that some detrital titanomagnetite is also present at U1391 further up the shelf. These higher Ti titanomagnetite samples are all located in interglacials, but no other correlation with climate signals is observed. This is an unexpected observation as detrital material is most likely to contain titanomagnetite, which is expected to contribute more to the sediments at cold intervals with low sea levels. Potentially, the titanomagnetite forms a greater proportion of the sediments and is therefore more visible in the results at these warm intervals because the finer magnetite fraction has been impacted by reductive diagenesis.

A feature of every measured sample is the increase in susceptibility at ~350 °C. This magnetic enhancement likely represents the formation of new magnetite from minerals such as smectite (Hirt et al., 1993), ferrihydrite or lepidocrocite (Hanesch et al., 2006), which have been shown to transform around this temperature.

It is of note that the lack of trend between κ_{ARM}/κ values (colours in Figure 3.2) and κ-T sample behaviours indicates that there is little relationship between grain size and mineralogy in these samples.

Selected representative FORC diagrams are shown in Figure 3.5, including showing typical behaviour from glacial and interglacial intervals. The majority of the FORC diagrams, through both warm and cold intervals show a narrow ridge elongated along the Bc axis, up to 60 – 80 mT. This is consistent with the coercivity of the dominant component 1 observed in IRM acquisition data (Figure 3.3) which was interpreted to be detrital magnetite. At MD01-2444 at ~2500 mbsl Channell et al., (2013) determined through similar FORC observations and TEM analysis that a major component was biogenic magnetite. Together, these observations are all indicative of fine-grained magnetite being the dominant magnetic phase at Site U1391 throughout the studied interval. While at warm intervals just the narrow ridge is observed with minimal vertical spread (Figure 3.5a); cold intervals show more interaction along the vertical axis indicating presence of coarser magnetite (Figure 3.5b). This indicates an enhanced detrital contribution at stadials and glacials, compared to warm intervals which may have a higher proportion of a finer phase of magnetite, possibly biogenic in origin. The FORC diagram from 48 ka (Figure 3.5c) at Heinrich Stadial 5 shows low coercivity (Bc) and more particle interaction indicating magnetite at the coarser end of PSD and toward MD (similar to Channell et al 2013). This coincides with low κ_{ARM}/κ values and a peak in susceptibility in Figure 3.1, also indicative of coarser magnetic grains. The FORC diagram in Figure 3.5d indicates lower coercivity coarser grained material. Other rock magnetic results from the same sample show a narrow hysteresis loop and a weak and noisy IRM

acquisition curve. This may be a result of reductive diagenesis removing the fine magnetite grains (discussed in Section 3.3.3). Toward the base of the record, especially in MIS 9 and 11, samples retain very little remanence presenting difficulties in getting a reliable FORC measurement.

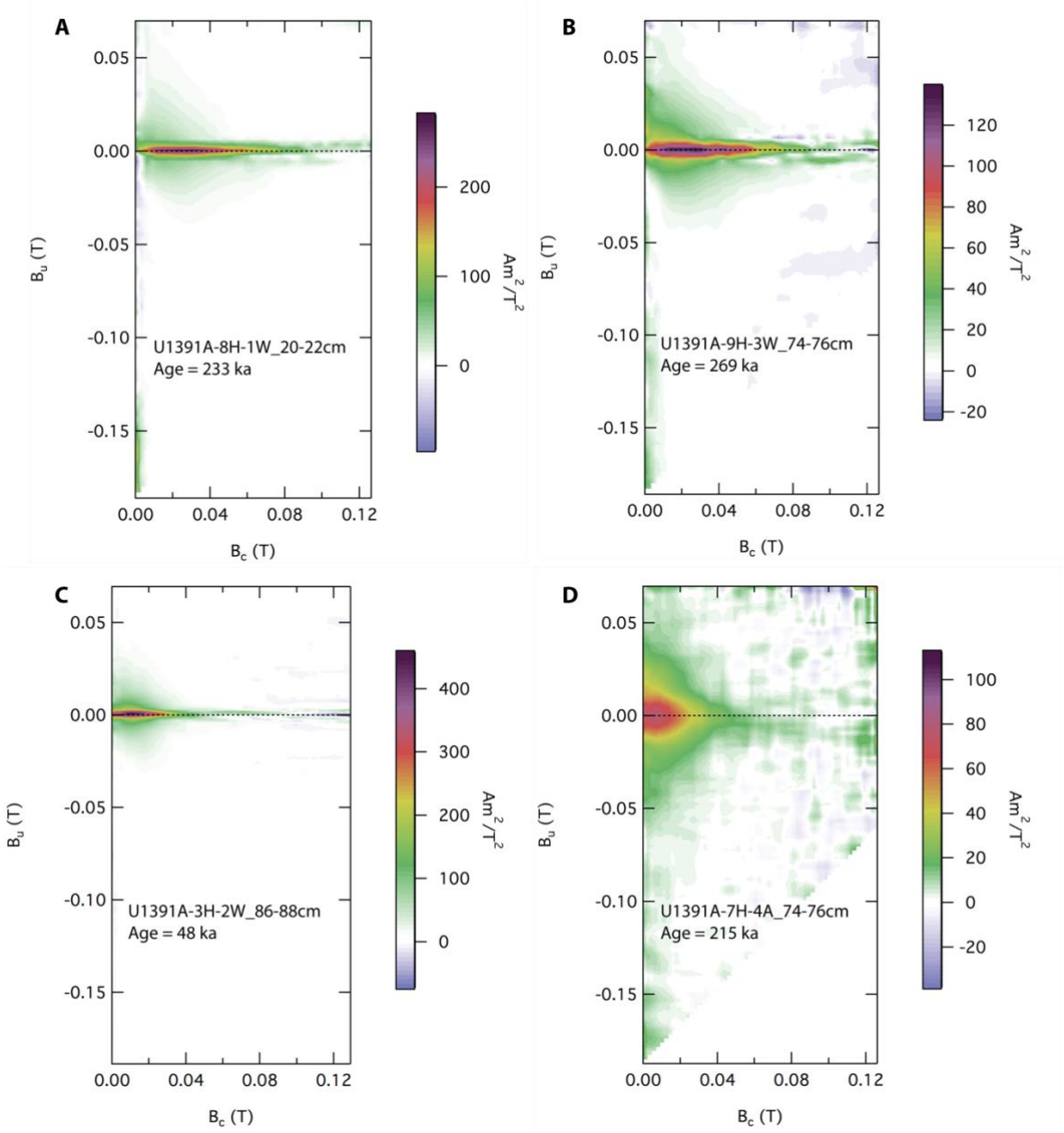

Figure 3.5. FORC diagrams of Site U1391 sediment samples from: A) a typical interglacial interval, B) a typical glacial interval, C) Heinrich event 5, and D) MIS 7.

In summary, our rock magnetic analyses suggest that magnetite is the dominant phase contributing to magnetic remanence. After ~130 ka, variations in environmental and rock magnetic parameters are the direct result of environmental influences, particularly sea level and SST. Multiple sources of detrital magnetite are present, likely from the shelf and MOW. Additionally, at cold intervals a higher coercivity component that could be aeolian dust from North Africa, though we can't rule out that this is also from the shelf. Evidence of a fine-grained

phase, possibly biogenic magnetite, is displayed in the FORC diagrams. Before ~130 ka variations in environmental magnetic parameters are mostly due to varying levels of reduction affecting different magnetic grain sizes by proportionately different amounts. At MIS 7e, 9 and 11 the smallest grains were majorly impacted and possibly all dissolved. The outer layer of coarser detrital grains may have been diagenetically impacted, leaving a magnetite core.

3.3.3 Oxidation state changes at Site U1391 before MIS 5

Diagenetic chemical changes in sedimentary environments are strongly associated with the degradation of organic matter, accumulated from terrestrial and/or marine plant, animal and planktonic remains. Microbes derive energy from this organic matter through oxidation of organic compounds, releasing CO2, leading to the oxidative degradation of the organic compounds (Roberts, 2015). Microbial metabolism requires an oxidant to reduce; when one becomes depleted it proceeds to the next most energy producing oxidant in a sequence of progressively lower free energy yields, as follows: oxygen, nitrate, manganese oxides, iron (oxyhydr-)oxides, sulphate, and organic matter itself (Froelich et al., 1979). This sequence leads to the formation of different diagenetic zones in sediment profiles which can be characterised by the oxidant of choice and the accompanying respiration process in parentheses) are oxic (aerobic respiration), nitrogenous (nitrate reduction), manganous (manganese reduction), ferruginous (iron reduction), sulphidic (sulphate reduction), and methanic (methanogenesis) (Canfield & Thamdrup, 2009).

These zones can be identified by pore water chemistry profiles, as manganese oxides, iron (oxyhydr-)oxides, and sulphate are reduced, the concentration of Mn^{2+}, Fe^{2+}, and H_2S, respectively, increases in sedimentary pore waters. The release of these ions provides reactants for authigenic mineral formation, the presence of which can be used as indicator of diagenetic conditions (Berner, 1981).

The depletion of sulphate in pore waters indicates that these sediments have passed through the ferruginous (iron reduction) zone, which is most likely to have degraded the primary magnetic signal. The sulphate ion concentration in U1391 sediments drops from 3.8 mM to 0 mM between 12.95 and 22.35 metres below sea floor (Expedition 339 Scientists, 2013). This equates to an age of between ~35 and ~68 ka and so does not coincide with the notable changes in ARM intensity between 130 to 200 ka, or the ln(Fe/κ) baseline shift at 88 ka, and is therefore unlikely to be related.

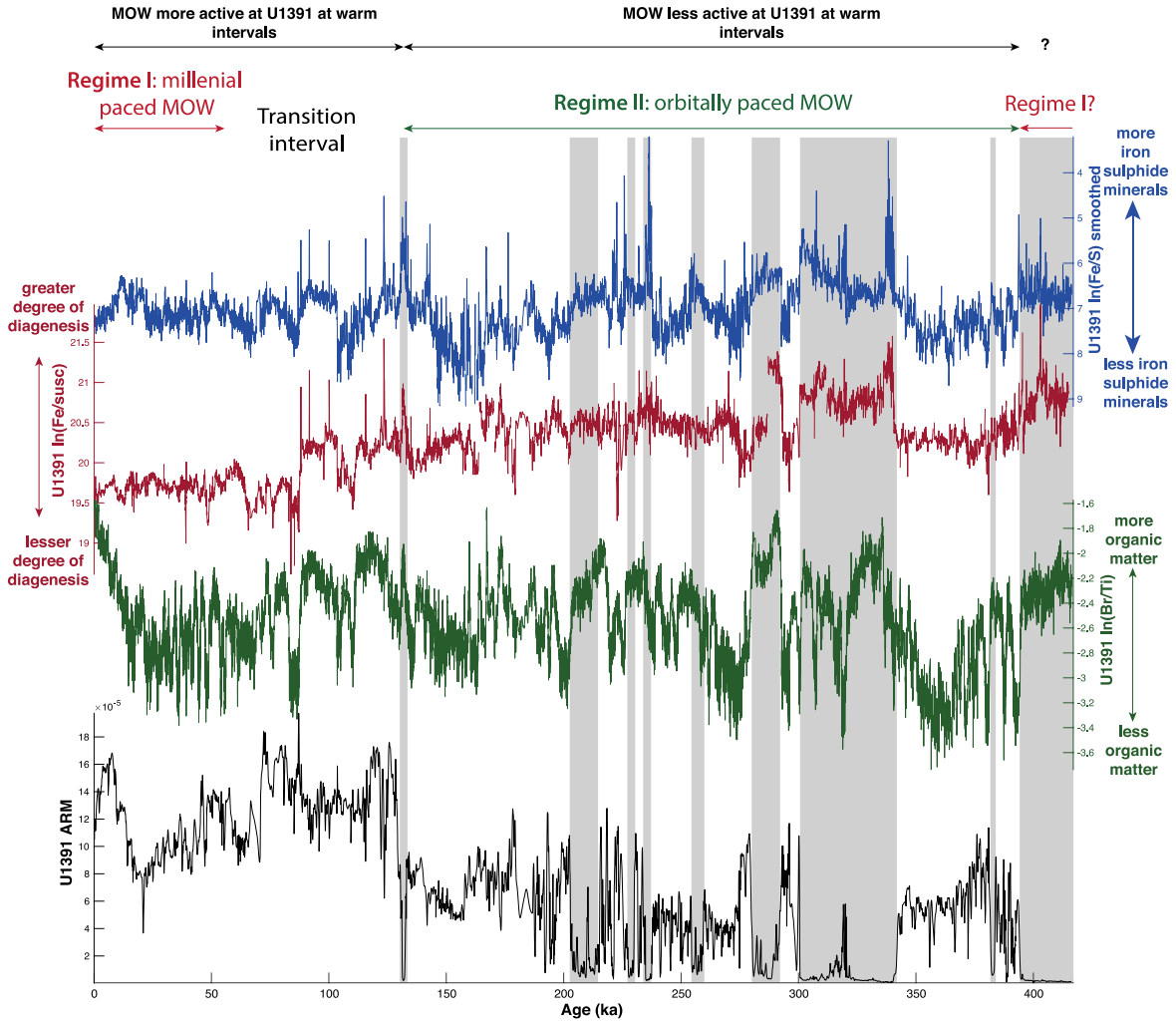

Figure 3.6. Diagenesis proxies at Site U1391. From top to bottom: ln(Fe/S), ln(Fe/κ), ln(Br/Ti), ARM. Vertical grey bars indicate intervals of reduced ARM intensity where diagenetic processes are inferred to have occurred.

We would expect to see an increase in ln(Fe/κ) during intervals of increased diagenesis. As seen in Figure 3.6, highs in ln(Fe/κ) values tend to coincide with lows in ARM intensity, particularly at MIS 9 and 11, suggesting that these lows are caused by reductive diagenesis. Additionally, at these intervals, ln(Br/Ti) increases indicating greater concentrations of organic matter (Bahr et al., 2014; Ziegler et al., 2008), and ln(Fe/S) decreases indicating more iron sulphide minerals are present (Figure 3.6). I therefore attribute the lows in ARM intensity at MIS 7, 9 and 11 to non-steady state reductive diagenesis caused by interglacial increases in organic matter flux to the seafloor. The associated reduction in oxygen content in sediment pore waters due to increased microbial respiration caused reduction of magnetite grains by sulphate ions available in sea water. The finest magnetite grains would have been most susceptible to diagenesis due to their high surface-to-volume ratio causing the relative increase in proportion of coarser grains and the increase in magnetic grain size at these intervals (κ_{ARM}/κ in Figure 3.1).

The same indications of diagenesis through these warm intervals at U1391 is not seen deeper (~2500 mbsl) on the west Iberian Margin (Channell et al., 2013; Moreno et al., 2002) suggesting some unique feature to shallower depths and Site U1391 is the cause. Notably, a baseline decrease in ln(Fe/κ) is observed at ~88 ka (Figure 3.6) suggesting that before this time, more Fe was found in minerals with a lower susceptibility, likely due to a generally higher level of reductive diagenesis (Funk et al., 2003a).

The baseline decrease in ln(Fe/κ) occurs during the transition phase of MOW behaviour, when the average depth of MOW was interpreted to be shifting to deeper on the Iberian Margin. The diagenesis may, therefore, be linked to the changing regimes of MOW behaviour across the studied interval, and associated changes in sedimentation rates (Nichols et al., 2020). This migration would not impact upon the deeper site U1385 (current water depth of ~2585 m). Sedimentation rates at Site U1391 from MIS 11 to 6 remained steady at ~29 cm/kyr (Figure 2.2 and Nichols et al., 2020). However, at the beginning of MIS 5, the sedimentation rate begins to increase sharply, peaking at ~38 cm/kyr in MIS 4. This would have caused MIS 5 sediments to have passed through the dissolution front of the reductive diagenetic zone much more rapidly compared to previous interglacials. Consequently, the fine-grained magnetite was exposed to the dissolution front for a significantly shorter period of time leaving the grains and primary magnetic signal relatively less affected by diagenetic processes.

3.3.4 Millennial scale variability from MIS 5 to present

Variations in κ_{ARM}/κ at deep sites on the west Iberian Margin (e.g. MD01-2444) follow climatic changes over orbital time scales (Channell et al., 2013; Moreno et al., 2002). Site U1391 κ_{ARM}/κ variability is similar to climatic changes down to millennial scale variability (Figure 3.7). As U1391 experiences a different depositional regime compared to deeper sites on the west Iberian Margin (i.e. contourites generated by MOW as opposed to hemipelagic), and U1391 is not influenced by deep water currents, it is unlikely that magnetic grain size variations on the west Iberian Margin are controlled by deep sea transport of magnetite grains from the North Atlantic, as suggested by Moreno et al., (2002).

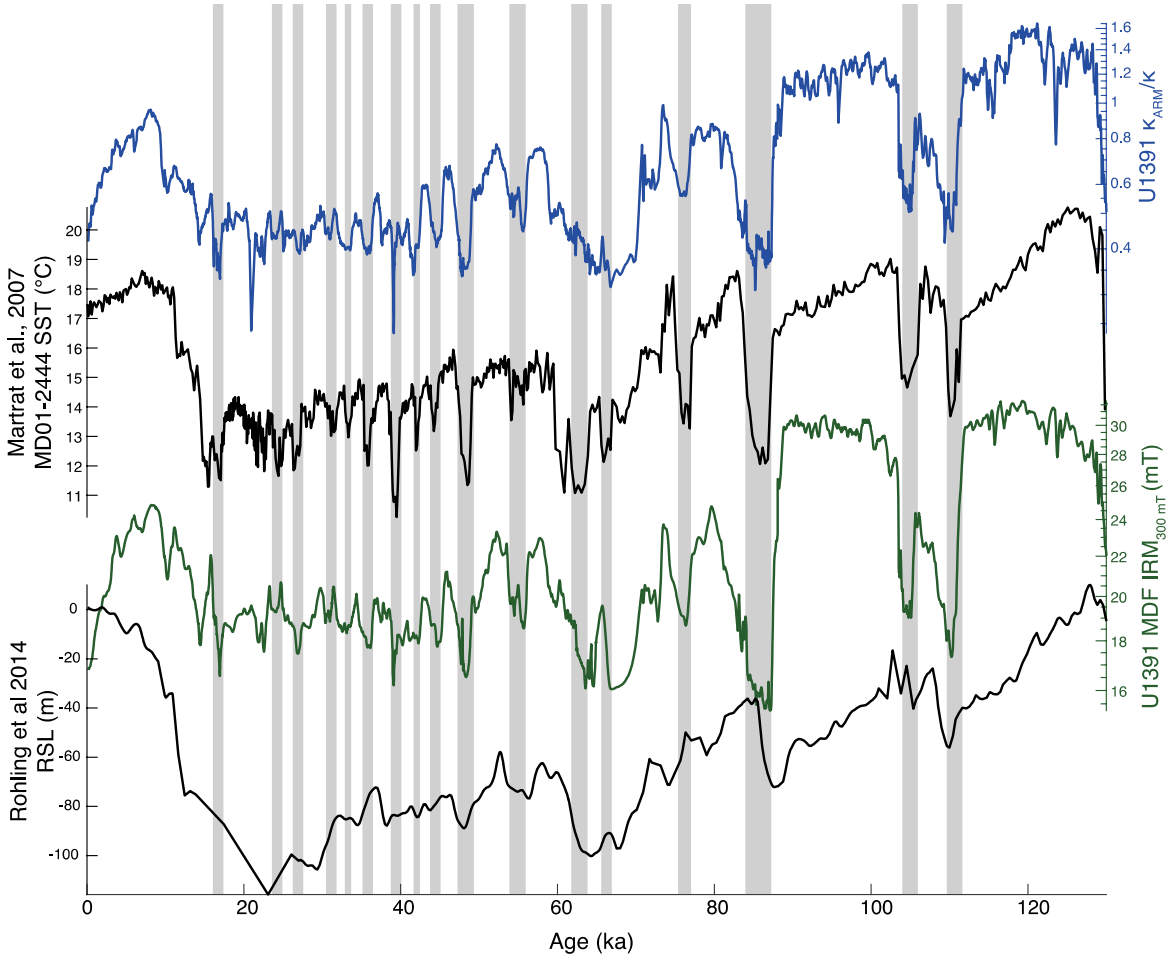

Figure 3.7. Millennial scale variability in environmental magnetic proxies of Site U1391 sediments during the last ~130 kyr. From top to bottom: U1391 κ_{ARM}/κ (log scale), MD01-2444 sea surface temperature (SST) (Martrat et al., 2007), MDF of $IRM_{300\ mT}$ and RSL at the Straits of Gibraltar (Rohling et al., 2014).

During stadials, Channell et al. (2013) determined that sea level controlled enhanced input of coarser detrital magnetite diluted fine biogenic magnetite, lowering κ_{ARM}/κ values. He and Pan (2020) found that at MD01-2444, more biogenic magnetite was produced (or preserved) at warm periods compared to cold periods. This would have the effect of raising κ_{ARM}/κ values at these interstadials, in agreement with κ_{ARM}/κ variability at Site U1391. Given the strong correlation of SST (Martrat et al., 2007) and κ_{ARM}/κ at Site U1391 back to ~130 ka (Figure 3.7), and the presence of narrow horizontal ridges seen in FORC diagrams from Site U1391 (Figure 3.5) indicating the presence of a fine magnetic phase (possibly biogenic magnetite) we infer that SST could be the major control of magnetic grain size variability, influencing differing rates of growth of biogenic magnetite at warm and cold intervals. This implies that the fine biogenic component is more important for κ_{ARM}/κ values than the sea level controlled detrital input of coarser magnetite at Site U1391 in the latest ~130 ka. As discussed in section 3.3.3, post-depositional processes affected the κ_{ARM}/κ record at U1391 before 130 ka.

3.3.5 Haematite on the Iberian Margin

S-ratio variations (Figure 3.1) in Iberian Margin sediments have previously been interpreted as representing haematite variations (Channell et al., 2013). At Site U1391 however, there are notable differences between HIRM and the S-ratio, this may indicate that the S-ratio is more controlled by reductive magnetite losses (diagenesis) or changing magnetite accumulation from different sources.

The Site U1391 S-ratio closely matches SST variability back to ~130 ka (Figure 3.1), showing higher coercivities at colder intervals, in agreement with HIRM variability and backing up IRM acquisition interpretations (Figure 3.3). In order to interpret the S-ratio at Site U1391, it first needs to be determined if variability is due to changing concentrations of high coercivity minerals or changes in their mineralogy (i.e. different sources) (Liu et al., 2007). This can be determined using a combination of the L-ratio (HIRM/(0.5 * (SIRM + IRM_{-100mT})) and hard isothermal remnant magnetisation (HIRM; $IRM_{AF@300mT}$) (Liu et al., 2007). The L-ratio is used to determine if there are significant changes in the hard coercivity component. If the L-ratio and HIRM show a linear relationship, changes in the S-ratio are likely driven by changes in mineralogy (i.e. type of mineral and provenance), whereas if the L-ratio is more constant and shows no relationship with HIRM, changes in the S-ratio are more likely driven by concentration variations of the same mineral type from the same source (Liu et al., 2007).

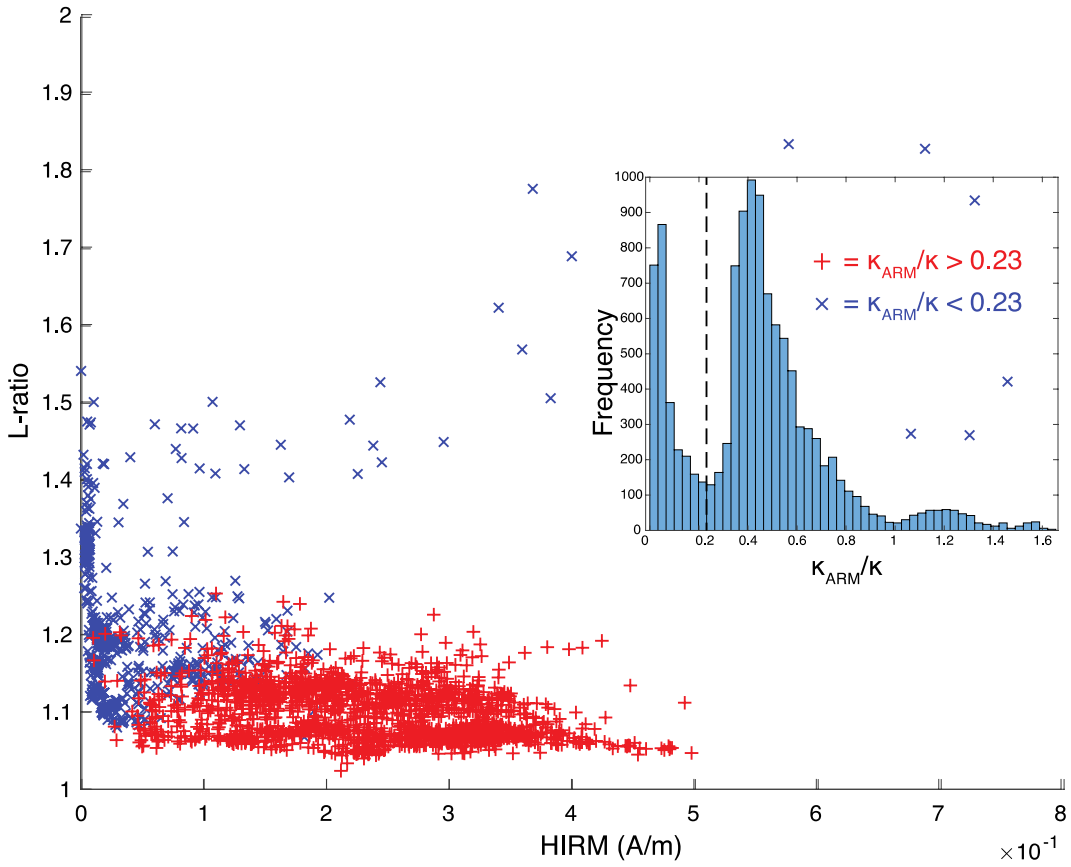

Figure 3.8. Scatter plot of L-ratio vs HIRM for Site U1391 with histogram of κ_{ARM}/κ values. Colours in scatter plot are chosen according to high (red) or low (blue) κ_{ARM}/κ value. Much greater scatter in L-ratio values is observed for low κ_{ARM}/κ values.

Figure 3.8 shows that for finer magnetic sediments, the L-ratio values do not vary greatly with changing HIRM. This suggests variations in the S-ratio are likely caused by concentration variations of higher coercivity minerals from one source, as opposed to varying quantities of different high coercivity minerals from multiple sources. Back to ~130 ka we suggest this source may be North African dust, as this region is known to have become more arid at cold intervals, producing more dust which is known to contain high quantities of haematite (Larrasoaña et al., 2003).

The S-ratio does not track SST variability before ~130 ka (Figure 3.1). It is in this deeper interval that the lowest κ_{ARM}/κ values are observed, which are thought to be caused by reductive diagenesis (Section 3.3.3). For these low values of κ_{ARM}/κ there is a different relationship between HIRM and the L-ratio (Figure 3.8) indicating a link between reductive diagenesis and the lack of relationship between S-ratio and SST in this interval. The S-ratio will be altered by diagenetic effects because haematite is also sensitive to changes in redox state, in sulphidic environments it will react with dissolved sulphide (Canfield, 1989; Roberts, 2015)

Site U1391 HIRM values (Figure 3.1) tend to peak at millennial scale cold events throughout the record indicating an influx of high coercivity material at these times, likely aeolian haematite potentially sourced from North Africa.

3.4 Conclusions

The magnetic phases in Site U1391 sediments back to ~130 ka are dominated by detrital magnetite and a fine magnetite phase that is likely biogenic in origin. The grain size and concentration of these phases were strongly controlled by northern high latitude climate variability through the action of temperature-controlled production of biogenic magnetite and sea level controlled detrital input. At stadials an additional high coercivity component is present, possibly representing haematite derived from North African dust.

Before ~130 ka, relatively lower sedimentation rates and high levels of organic matter, particularly at interglacials MIS 7e, 9 and 11, led to enhanced reductive dissolution of fine-grained magnetite and the weakening of the primary magnetic signal. An increase in sedimentation rates, possibly linked with migration of MOW, during MIS 5 meant magnetic minerals in this interglacial were relatively less affected by reductive diagenesis.

Chapter 4 Forcing and phasing of grain size variabilities in Pleistocene sediments from the west Iberian Margin

4.1 Introduction

Grain size variability (i.e. sortable silt mean (SS)) has been used successfully in the Atlantic as a current speed indicator giving insight into the activity of deep-water masses (Bianchi & McCave, 1999; Spooner et al., 2018; Thornalley et al., 2013). The mean weight percent of the 150-63 μm fraction has been used as a grain size proxy for the strength of MOW in the Gulf of Cadiz (Kaboth et al., 2017; Voelker et al., 2006). Magnetic grain size variability can give insight into palaeoceanographic changes. For example, it also has been used in the North Atlantic to trace deep water circulation (Kissel et al., 2009) and could be used on the west Iberian Margin to indicate a combination of sea level and the productivity of magnetotactic bacteria (Chapter 3 and in Channell et al. (2013)).

In this Chapter, the existing (low-resolution) physical grain size data at Site U1391 is updated to create a high-resolution record and is compared with SS% data. This is used to further constrain which grain size fractions the core-scanning grain size proxies, ln(Zr/Rb) and κ_{ARM}/κ, represent. Once understood, these high-resolution core-scanning records, together with the strong age model constructed in Chapter 2, are used to characterise the phase at precession periodicities between MOW variability and insolation forcing. This MOW analysis is only possible with this combination and it may not have been possible to investigate before with existing records.

4.1.1 Orbital forcing of MOW strength variability

As described in chapter 2, Levantine Intermediate Water (LIW) formation rate is known to affect the strength of MOW. Therefore, to understand the underlying causes of Mediterranean outflow strength variability, the long-term forcing of changes in LIW formation must be understood.

Annually, the direct driver of LIW formation is cool, dry and strong winter and spring winds from the north that cause strong mixing and evaporation of surface waters enhancing vertical convection. African hydroclimate modulates surface water salinity in the eastern Mediterranean via the rate of freshwater runoff (Rohling et al., 2015).

Over orbital timescales, interpretations of palaeoclimate records have proposed summer processes strongly influence Mediterranean salinity and deep-water formation, particularly in the Levantine basin. Wet and dry phases in North African hydroclimate are strongly associated with peak northern hemisphere summer insolation (e.g. Bosmans et al., 2015; Rossignol-Strick, 1985). These wet phases cause enhanced freshwater run-off into the eastern Mediterranean, decreasing the density of surface waters, resulting in distinct reductions in deep water ventilation. This is the process of sapropel formation. Alongside the dry phases, where there is a resultant increase in deep-water formation, these processes have also been linked to changes in the rate of Mediterranean outflow into the North Atlantic, by way of altering the density contrast between the two water masses (Bahr et al., 2015; Kaboth et al., 2017). However, this mechanism does not take into account long term variations in winter-time factors involved in the forcing of LIW formation.

Grant et al. (2016) determined that winter precipitation over the eastern Mediterranean is likely sourced from within the basin. The significance of this inference is that if the source of winter moisture is local (or internal to the Mediterranean), the precipitation-evaporation (P-E) balance in the basin would not be significantly affected. However, if an external source were transporting moisture to the eastern Mediterranean, P-E and net buoyancy would change, with potential implications for the driving mechanisms behind deep-water formation.

Studies noting the importance of winter processes appear to be limited to modelling studies, and are often not discussed in palaeoclimate records. Over orbital timescales there are precession induced precipitation – evaporation (P-E) differences across the Mediterranean Sea (Bosmans et al., 2020; Kutzbach et al., 2013; Orland et al., 2019). At precession minima, greater winter precipitation and year-round lower evaporation over the eastern Mediterranean have been modelled. While at precession maxima, where a faster MOW is interpreted in chapter 2, there are higher rates of winter evaporation.

The mechanism behind these moisture sources is debated however may be significant in why winter P-E variability has not previously been considered too important in data studies, as internal sources theoretically do not significantly impact P-E (Grant et al 2016). Bosmans et al. (2020) find that during precession minima, in the winter half of the year, there are significant external (North Atlantic) sources of moisture and there is significantly increased precipitation relative to precession maxima. These remotes sources are attributed to transport from the subtropical Atlantic and reduced sea level pressure at the Azores High. Earlier modelling studies (Bosmans et al., 2015; Kutzbach et al., 2013; Orland et al., 2019) attributed increased winter precipitation to

enhanced activity of the North Atlantic Mediterranean storm tracks. Determining the exact mechanism is beyond the scope of this study.

Bosmans et al. (2015) point out that these precession paced winter-time changes may be more important than summer processes for deep water formation as they primarily occur over the Levantine and Adriatic/Ionean seas in the critical season for intermediate and deep-water formation. Further, they speculate that these salinity and mixed layer depth changes could have an effect on the exchange of water at the Strait of Gibraltar.

The question can then be asked, similar to one posed in Bosmans et al. (2020), which of these two potential driving mechanisms for LIW formation-rate change, winter P-E or monsoonal freshwater run-off, is the more important forcing for MOW strength variability over orbital timescales? Utilising the strong age-control, independent of orbital parameters, and high-resolution ln(Zr/Rb) record from Site U1391 (Chapter 2), the coherence and phasing of grain size data is tested against insolation components from different seasons. It would be expected that changes in ln(Zr/Rb) would lag behind the insolation forcing, depending on the length of time taken for the forcing to pass through the climate system. The length of this lag time is also investigated.

4.1.2 Grain size processes

The causes of mean grain size and magnetic grain size variability at Site U1391 have been discussed in chapters 2 and 3, respectively. Mean physical grain size is interpreted to be current controlled and responds to changes in the strength and position of the MOW. Magnetic grain size varies according to SST controlled growth and preservation of fine-grained biogenic magnetite and sea-level controlled dilution of this biogenic component by relatively coarser detrital magnetite. κ_{ARM}/κ is known to be sensitive to fine magnetic grain sizes (~< 1 - 15 μm) (Banerjee et al., 1981). Ln(Zr/Rb) is thought to be sensitive to coarser grain sizes than κ_{ARM}/κ because Zr is concentrated in resistate minerals while Rb is relatively dispersed and commonly found in mica, illite, and K-feldspar (Dypvik & Harris, 2001; Wu et al., 2020).

Moreno et al. (2002) noted the decoupling of magnetic and physical grain size parameters at MD95-2040 (~2665 metres below sea level (mbsl)) on the west Iberian Margin. At interstadials, κ_{ARM}/κ indicated magnetic material became finer whereas the silt/clay ratio increased (Hall & McCave, 2000).

Opposing behaviour of fractions above and below 10 μm in sediments has also been observed on the Nova Scotia Rise (McCave, 1985; McCave, et al., 1995). This pattern was attributed to the

cohesive behaviour of fine sediment grains <10 μm. The deposition of these fine grains is suppressed under fast currents because they tend to form aggregates which settle at slower current speeds (McCave, et al., 1995) Larger and faster settling aggregates, which might otherwise be deposited, are weaker and tend to break up. Therefore, one would expect the ratio of 10-63 μm material to the total fine fraction (<63 μm) to increase with current speed (McCave, et al., 1995). This ratio is known as the sortable silt percent (SS%).

In this chapter, the relationship between magnetic, XRF and physical grain size parameters is tested at Site U1391. Firstly, it is determined which grain size fractions the different proxies are sensitive to and, secondly, it is determined if the decoupling of parameters observed at MD95-2040 is also the case for shallower depths on the Iberian Margin under different hydrological conditions. High resolution ln(Zr/Rb) is then used to answer phase related questions outlined in section 4.1.1.

4.2 Methods

4.2.1 Physical Grain Size

A high-resolution physical grain size record was generated, consisting of 204 measurements covering the last ~416 kyr. The method was as described for the low-resolution record in Chapter 2 with one difference. Instead of sieving at 106 μm it was decided not to sieve the sediments at all for the remaining samples. The main reason for sieving the sediments initially was to prevent large grains from blocking the 200 μm aperture on the Coulter Counter. However, a very small proportion (~1.7 %) of material was found at sizes greater than 106 μm, and blocking of the aperture was deemed unlikely. Seven samples with a range of mean sizes were repeated between the different methods (i.e. sieved and not sieved) and no discrepancies were found between results. Therefore, the decision was made to not sieve the samples and streamline the whole process, saving significant amounts of time.

Grain size statistics, including geometric mean, sorting, skewness and kurtosis, were calculated using the GRADISTAT software (Blott & Pye, 2001).

Similar to the SS% method (McCave et al., 1995), the proportion of material greater than 10 μm is compared with the proportion less than 10 μm. As these Site U1391 samples are not sieved, the proportion of all material greater than 10 μm is measured, rather than that up to 63 μm. This is therefore not strictly SS% as described in McCave et al. (1995), however the method used here is thought to be a good approximation (Crowhurst, pers. comm.) as sand sized material (>63 μm) generally only forms a small proportion of the bulk composition.

The percentage of material greater than 10 μm was measured at the Godwin Laboratory for Palaeoclimate Research at the University of Cambridge using the following steps, based on the method originally described in Folk (1980) which uses the principle of Stokes' Law of settling velocity. Small (0.5 g, 75 x 85mm) polyethylene bags were carefully weighed on a Sartorius Quintix 125D-1S analytical balance to 100 thousandths of a gram/ 10 micrograms precision. Sediment samples in centrifuge tubes had 0.2% sodium hexametaphosphate in de-ionised water added to make a 100 ml total volume and were put on an end-over end shaker overnight to disaggregate. Any sediment still settled on the base of the centrifuge tube was put into suspension by shaking and 2 minutes of ultrasounds treatment. A 10 ml subsample of sediment slurry was withdrawn and added to 100 ml of 0.2% sodium hexametaphosphate in de-ionised water in a glass measuring cylinder and was well mixed by rotation. Immediately after mixing, a 5 ml subsample was withdrawn by pipette from 4 cm depth in the suspension and injected into one of the previously weighed small bags. Any remaining pipette contents was rinsed into the bag using de-ionised water. This bag was then placed open into a laboratory oven at 50 °C to dry. The sediment sample in the glass measuring cylinder was then re-mixed and a timer set for 7 minutes and 20 seconds following Stokes' law (Folk, 1980). After the elapse of the 7 minute 20 second interval, a second 5 ml subsample sample was withdrawn by pipette from 4 cm depth, put into another small bag and placed to dry in the same laboratory oven. After three days in the oven and after testing samples with successive weighing to ensure complete dryness, the samples and bags were weighed again using the Sartorius scales to determine the weight of each subsample. The ratio of the weights was used to establish the percentage of material greater than 10 microns.

Comparing the covariance of SS% and SS mean is useful for determining the cause of SS mean variability (McCave et al., 1995). Mean grain size can be affected by both transport mechanism and changing provenance of material. If there is a linear correlation between SS% and SS mean, sediments are likely only current sorted, if there is no clear relationship then other processes may have impacted deposition.

U1391 u-channels were continuously scanned at 0.5 cm resolution on an ITRAX XRF core scanner to acquire Zr and Rb counts. Magnetic grain size data were collected from the u-channels at 1 cm resolution, volume-susceptibility was measured by a Bartington MS3 meter and 42-mm diameter MS2C sensor loop and ARM by a 2G Enterprises liquid helium-cooled pass-through superconducting rock magnetometer. The methods for acquiring XRF and magnetic grain size proxies are described in detail in chapters 2 (also see Nichols et al., 2020) and 3, respectively.

4.2.2 Time-series analysis techniques

Many traditional methods of extracting periodicities from time-series data, e.g. Fourier analysis, make the assumption that frequency components are stationary throughout the record. In many geological time series however, this is not the case. Wavelet transforms circumvent this issue by displaying periodicities within a time series in time-frequency space. A continuous wavelet transform (CWT) allows the visualisation of power in time- and frequency-limited periodicities by expansion of a time into in time-frequency space. A cross-wavelet transform (XWT) compares two CWTs to reveal intervals of common frequencies and phasing in time-frequency space. Wavelet coherence (WTC) compares two CWTs to reveal intervals of significant coherence, even when common power is low (Grinsted et al., 2004). Wavelet coherence (WTC) and phasing analysis were performed using the cross wavelet and wavelet coherence toolbox for MATLAB (Grinsted et al., 2004). CWTs were calculated for our ln(Zr/Rb) grain size proxy record and different seasons of northern hemisphere insolation. A WTC was then calculated between grain size and insolation CWTs to reveal common power and relative phasing between two time series in time-frequency space.

4.3 Investigations into Grain Size Variability at Site U1391

The correlation between a lower resolution mean grain size (5 - 106 µm) record and ln(Zr/Rb) was discussed in Chapter 2. The higher temporal resolution data presented in Figure 4.1 corroborates this. Mean size correlates strongly with ln(Zr/Rb) showing strong precession cyclicity, particularly from MIS 10 to 5 inclusive, and millennial scale variability in MIS 11 and from MIS 4 to present. The linear trend between the two proxies is shown by the scatter plot in Figure 4.1.

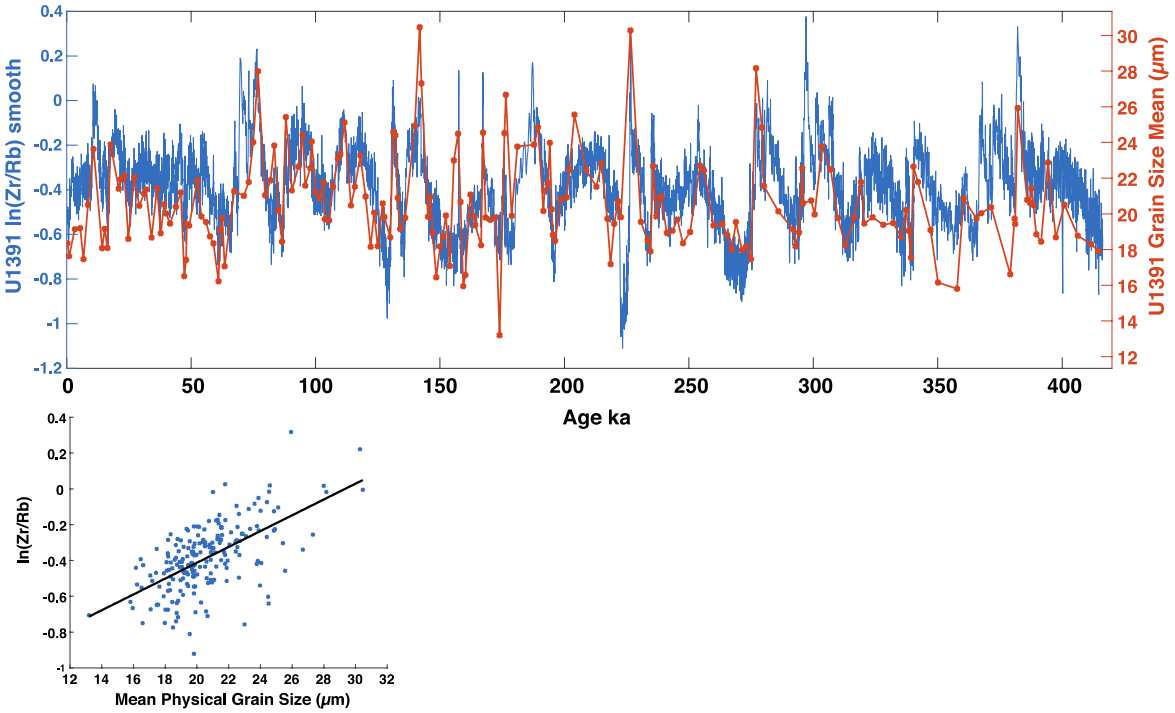

Figure 4.1. Time-series (top) and scatter (bottom) plot of U1391 ln(Zr/Rb) vs mean (geometric) physical grain size (5-106 μm).

Figure 4.2 compares SS% and mean grain size. The linear correlation coefficient across all samples is 0.3, indicating processes other than current speed may be affecting this relationship. Calculating the correlation coefficient using data from different time intervals reveals more information. SS mean and SS% from 130 ka to present have a stronger and more positive correlation compared with the data from 416 ka to 130 ka, with linear correlation coefficients of 0.62 and 0.14, respectively (Figure 4.2). The timing of this change in behaviour is present through much of the data in this thesis, similar to the MOW regime change interpreted in Chapter 2 and reduction in levels of diagenesis in Chapter 3.

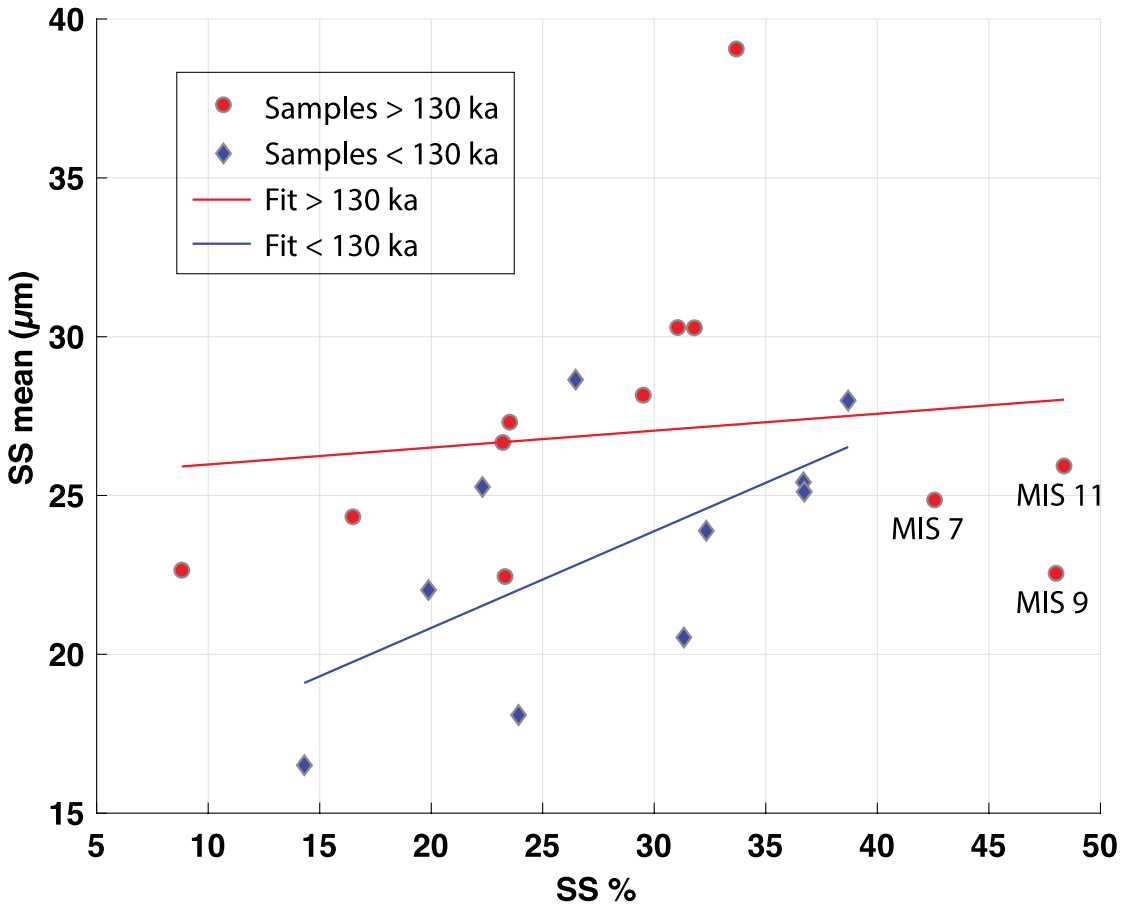

Figure 4.2. Sortable silt mean vs sortable silt %, 0-130 ka (dark) and 130 – 416 ka (red). Lines of fit are displayed for the interval after 130 ka (blue line) and before 130 ka (red line) with linear correlation coefficients of 0.62 and 0.14, respectively. Samples from MIS 7, 9 and 11 are highlighted.

The differing relationship of SS mean and SS% before and after 130 ka may have been caused by changes in the proportion of clay in the sediment or by differing diagenetic effects on the fine silt fraction in warm and cold intervals. The highest SS% values (highlighted in Figure 4.2) are from interglacials MIS 7, 9 and 11. It has been shown that the impact of diagenesis on the sediment magnetic records was greater at these warm intervals compared with the cold intervals (see Chapter 3). The greater degree of diagenesis at MIS 7, 9 and 11, likely impacted the fine fraction most significantly, as observed in the reduced ARM intensities and low κ_{ARM}/κ values. This may have had the effect of raising SS% at these times, as the proportion of material in the fine fraction is reduced. This would have impacted the relationship between SS mean - SS% independently of current speed, causing the relationship to be weaker before 130 ka. If the data points at MIS 7, 9 and 11 had mean SS% values closer to the average, then the correlation of SS % vs SS mean across the whole record would be higher.

The mean physical grain size was likely not affected by at these stages because the diagenesis would have most significantly affected fine grained material, and particles of less than 5 μm were not measured by the Multisizer 3 Coulter Counter.

The deposition of IRD is a common cause of low SS% - SS mean correlation, however this is not thought to be a significant factor here as the high SS% samples were deposited in warm intervals where IRD deposition is unlikely. The data being dealt with here is not strictly the SS range of 10 – 63 μm as defined by McCave et al. (1995). It is acknowledged that this may impact the reliability of the results, although the counts of material greater than 63 μm is relatively low (~2.4%).

The degree of sorting in the sediments was calculated from grain size distributions using Gradistat software (Blott & Pye, 2001). The sorting degree positively correlates with mean grain size (Figure 4.3), indicating that the sediments are from a current controlled depositional setting. The degree of sorting would not be negatively impacted by diagenesis as may have happened with the SS% vs SS mean size relationship; removal of the fine fraction would only act to increase the degree of sorting.

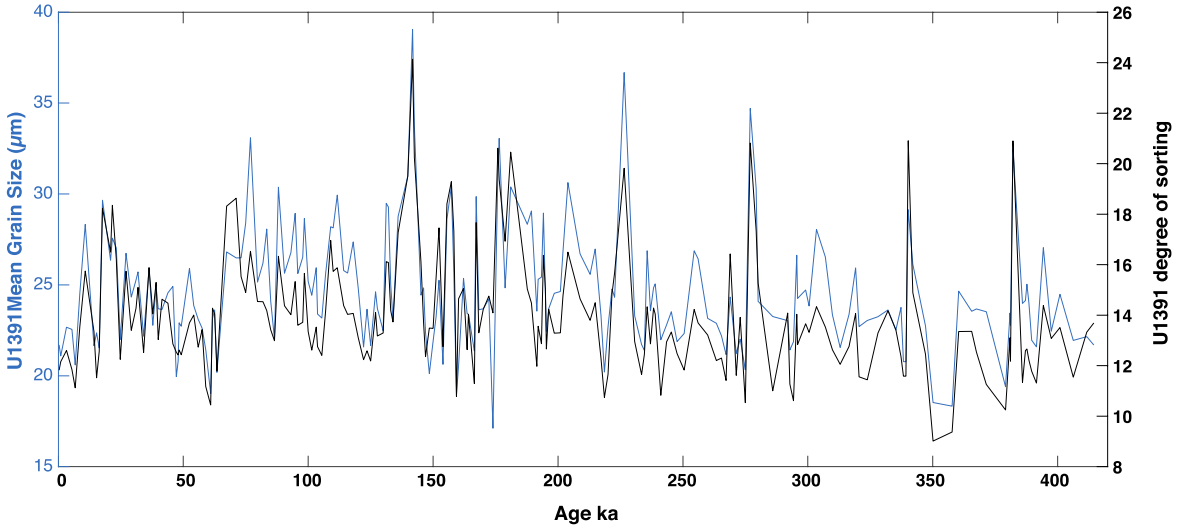

Figure 4.3. Degree of sorting calculated from grain size distributions and mean grain size at Site U1391.

The mean weight percent of the 150-63 μm fraction has been commonly used as a grain size proxy for the strength of MOW in the Gulf of Cadiz (Kaboth et al., 2017; Voelker et al., 2006). This is a popular proxy because it is easily attainable as part of sample processing for picking foraminifera. This grain size data was measured as part of Guo et al. (2017) and is compared with the mean grain size measured in this study (Figure 4.4). Grain size peaks are similar for both records, but a significant amount of orbital-scale structure is missing from the mean weight percent of the 150-63 μm fraction. The loss of this structure could lead to significant

misinterpretation of bottom-current strength changes. At Site U1391, ln(Zr/Rb) appears to be a better representation of mean physical grain size than the mean weight percent of the 150-63 μm fraction. It is therefore recommended that mean weight percent data is used with much caution and understanding of its limitations, and, if possible, in tandem with grain size distribution measurements and/or XRF data.

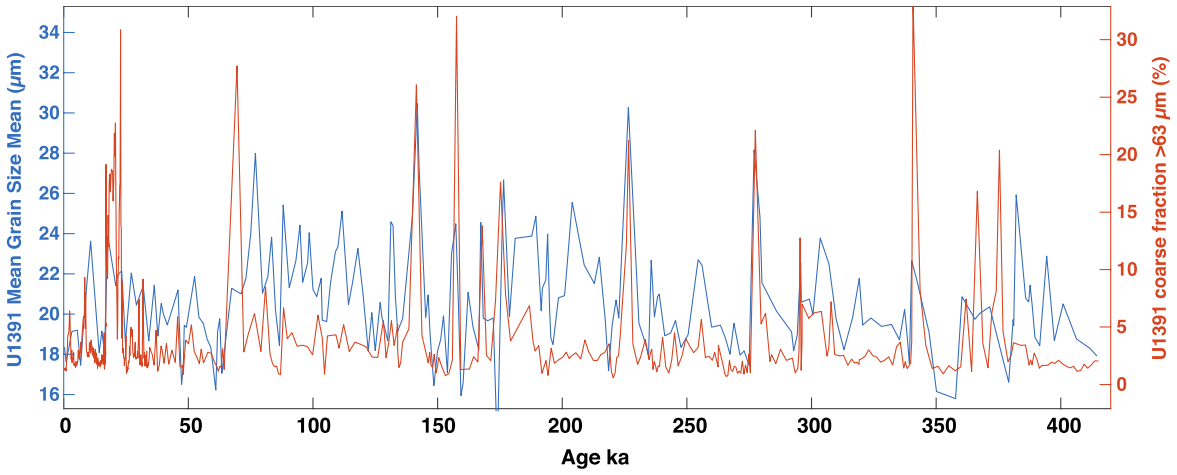

Figure 4.4. U1391 mean grain size (this study) vs mean weight percent of 63-150 μm fraction (Guo pers. comm.).

4.3.1 What do ln(Zr/Rb) and κ_{ARM}/κ physically represent?

The correlation coefficients between changes in each physical grain size bin and both ln(Zr/Rb) and magnetic grain size κ_{ARM}/κ) are shown in Figure 4.5. High values of κ_{ARM}/κ represent finer magnetic material, so a negative correlation coefficient with mean physical grain size indicates that the two proxies are showing the same direction of change. For this reason, the κ_{ARM}/κ axis is reversed in Figure 4.5. Over the range of grain sizes 5 – 100 μm, ln(Zr/Rb) and κ_{ARM}/κ show opposing patterns of correlation. Note, however, the different scales of the axes, ln(Zr/Rb) show stronger correlation with the physical grain size bins, with correlation coefficients up to ~0.6 compared with ~0.2 for κ_{ARM}/κ. Between the size fractions 8 - 19 μm, the correlation coefficients between κ_{ARM}/κ and physical grain size are all below -0.1, with a pronounced low between 14 – 16 μm, demonstrating that κ_{ARM}/κ is mostly sensitive to finer material. Over a similar interval, ln(Zr/Rb) shows the opposite pattern, showing the lowest correlation with physical grain size bins at ~11 μm. From 22 – 100 μm the two proxies switch and show the opposite behaviour to the finer fraction. Ln(Zr/Rb) has a positive correlation with physical grain size, peaking at 33 – 43 μm with correlation coefficients up to 0.6, while κ_{ARM}/κ shows positive correlation with highs also around 34 – 40 μm. From 40 to 100 μm both proxies trend steadily toward a correlation

coefficient of 0. Due to the relationship described here, we can use κ_{ARM}/κ as a finer fraction (< ~20 μm) indicator and ln(Zr/Rb) as a coarser material (> ~25 μm) indicator.

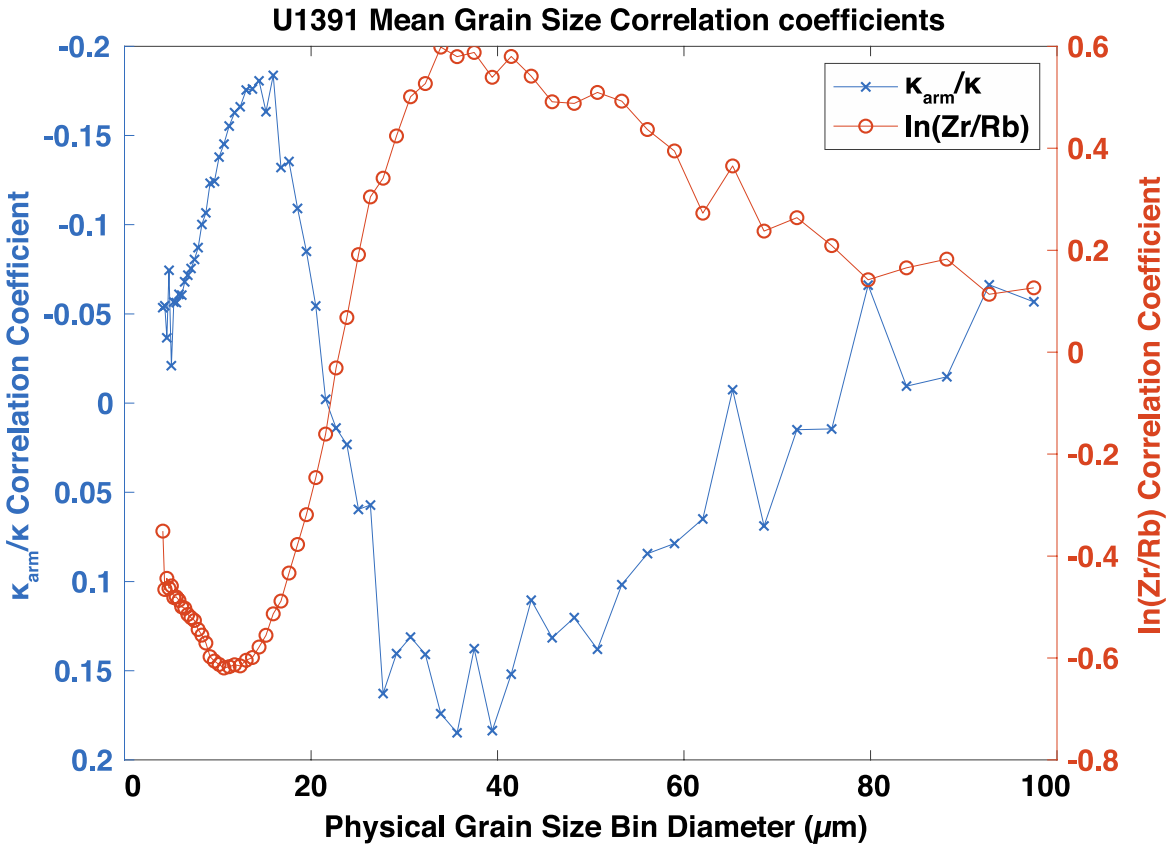

Figure 4.5. Grain size proxies, κ_{ARM}/κ (blue) and ln(Zr/Rb) (orange), linear correlation coefficients with physical grain size bins. Karm/K y-axis is reversed as higher values indicate finer magnetic grain sizes, so that direction of coarser grains is the same as ln(Zr/Rb).

4.3.2 Divergent behaviour of the coarse and fine grain size fractions

It has been interpreted in Chapters 2 and 3 that MOW speed is controlling the coarser grain sizes, while SST is primarily in control of the fine, magnetic fraction from 130 ka to present and diagenesis significantly affected fine magnetic grains before ~130 ka.

The variability of κ_{ARM}/κ and ln(Zr/Rb) are compared through time in Figure 4.6 where, because higher values of κ_{ARM}/κ indicate finer magnetic grain size but higher values of ln(Zr/Rb) indicate coarser grain size, similarities between the two curves indicate opposing behaviour of the coarse and fine fractions. Figure 4.6a shows the latest ~90 ka, where the two proxies generally display opposite behaviour. Notably, there is an apparent lag between the two proxies, κ_{ARM}/κ appears to lead ln(Zr/Rb) by a few kyrs, most clearly seen between ~135 and ~70 ka (Figure 4.6). From this

lag it can be inferred that the coarse and fine fractions could be driven by different processes that are acting according to different forcings, rather than both being driven by the same forcing (a current) that has opposite effect on different size fractions. It can also be inferred that κ_{ARM}/κ is unlikely to be sea level driven (as determined in chapter 3) because it would be expected that sea level forcing would be slower than the insolation forcing of MOW. κ_{ARM}/κ appears more SST dependent which would react more quickly to forcing (Figure 3.1 and Figure 3.7 in Chapter 3).

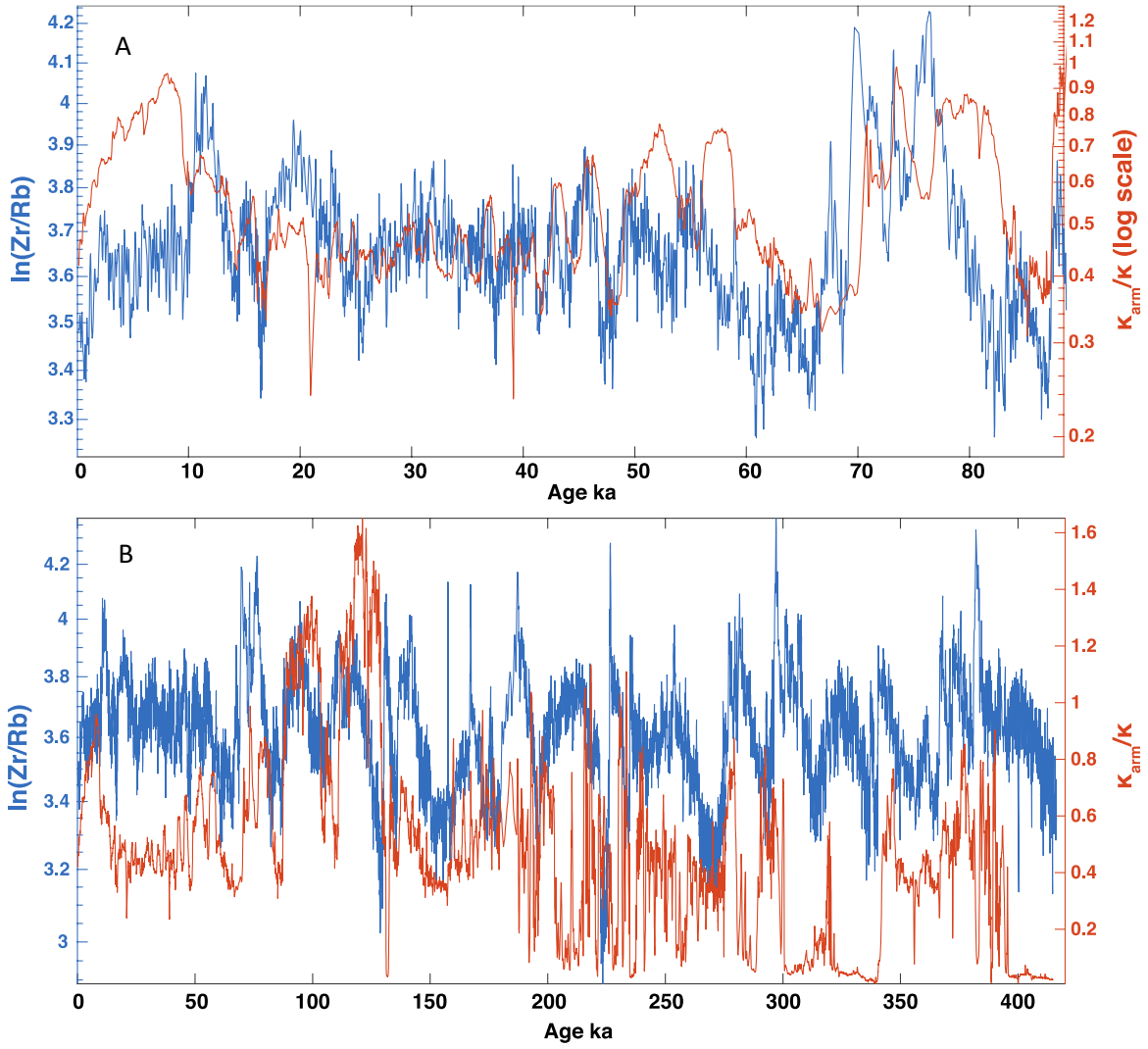

Figure 4.6. U1391 ln(Zr/Rb) (coarse up, fine down) vs κ_{ARM}/κ (fine up, coarse down). A) 0- 90ka B) 0 – 416 ka.

The pattern of opposite behaviour of the coarse and fine proxies is not so closely followed in the longer time series back to ~416 ka, shown in Figure 4.6b. However, this is likely due to the magnetic grain size proxy being more significantly affected by diagenesis (discussed in Chapter 3) than the XRF proxy, due to finer grains being more susceptible to reductive diagenesis and dissolution.

Establishing that ln(Zr/Rb) is an indicator of current sorted material allows us to more confidently interpret its variability in the context of MOW changes.

4.4 Spectral and phasing analysis of grain size records

The CWT of ln(Zr/Rb) (Figure 4.7) shows strong precession paced (19 to 23 kyr) cyclicity between ~60 and ~360 ka. This is an expected result as the cycles can also be clearly observed in the time domain signal and has been discussed in Chapter 2.

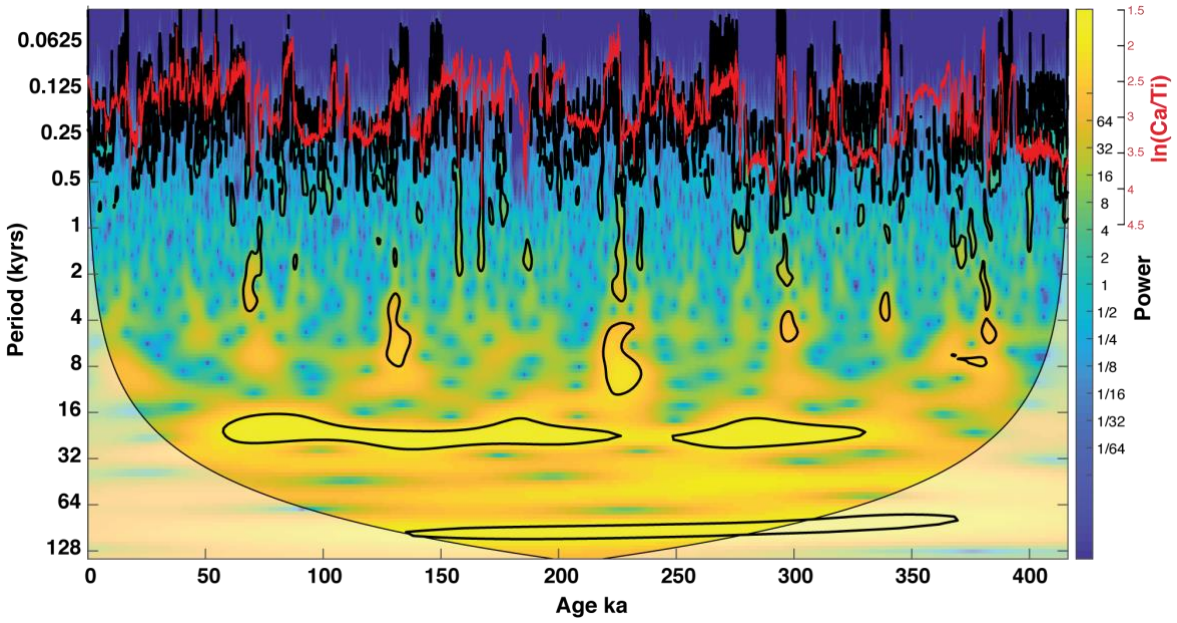

Figure 4.7. Continuous wavelet transform of ln(Zr/Rb) with ln(Ca/Ti) (reversed) overlaid (red line). Regions of significant power (0.9) are outlined in black.

In the high frequency regions of the ln(Zr/Rb) CWT, shifts between cycles with significant power at ~125 and ~250 years are observed to have similar temporal variability to ln(Ca/Ti) (superimposed in red on Figure 4.7). At times of lower ln(Ca/Ti) there is greater power in the higher frequency cycles of ln(Zr/Rb), ~125 years, whereas greater power is seen in frequencies of ~250 years when ln(Ca/Ti) is higher. As the age model has been constructed using ln(Ca/Ti) tie points, it is possible this observation is an artefact of relative stretching and compressing of cycles due to shifts in sedimentation rate between times of high and low Ca/Ti, respectively. However, there are no clear associated shifts in sedimentation rate (Figure 2.2 in Chapter 2). It appears that intervals of low ln(Ca/Ti), higher frequency (i.e. short-term) variability, are associated with higher levels of detrital input on the west Iberian Margin (Hodell et al., 2013). This may be indicating that the size of detrital material input is variable on short timescales.

4.4.1 Which component of insolation is forcing MOW?

Both summer and winter processes are known to affect Mediterranean salinity and intermediate and deep-water formation (Rohling et al., 2015). MOW flow strength is interpreted to increase at precession maxima (insolation minima) due to increased rates of intermediate water formation as a result of orbitally forced changes in these seasonal processes. To compare the phasing of MOW variability with seasonal insolation changes, a band-pass filter was applied to U1391 ln(Zr/Rb) record to extract precession-band (19-23 kyr) variabilities (Figure 4.8). Lows in summer insolation consistently occur after peaks in ln(Zr/Rb) at Site U1391, meaning summer insolation-forced processes are unlikely to be the major forcing on MOW variability. Spring insolation is a better fit, with lows consistently occurring just before peaks in ln(Zr/Rb). Phase angles presented in Figure 4.10a demonstrate this clearly, showing a consistent lag of summer insolation behind ln(Zr/Rb), distinct from the behaviour compared to spring insolation (Figure 4.10b). Wavelet coherence analysis confirms a strong phase relationship on precession cycles between ln(Zr/Rb) and spring insolation at 35°N between ~60 and 360 ka (Figure 4.9). The mean phase lag at 19 kyr periodicities between 60 and 360 ka is ~1.6 kyrs.

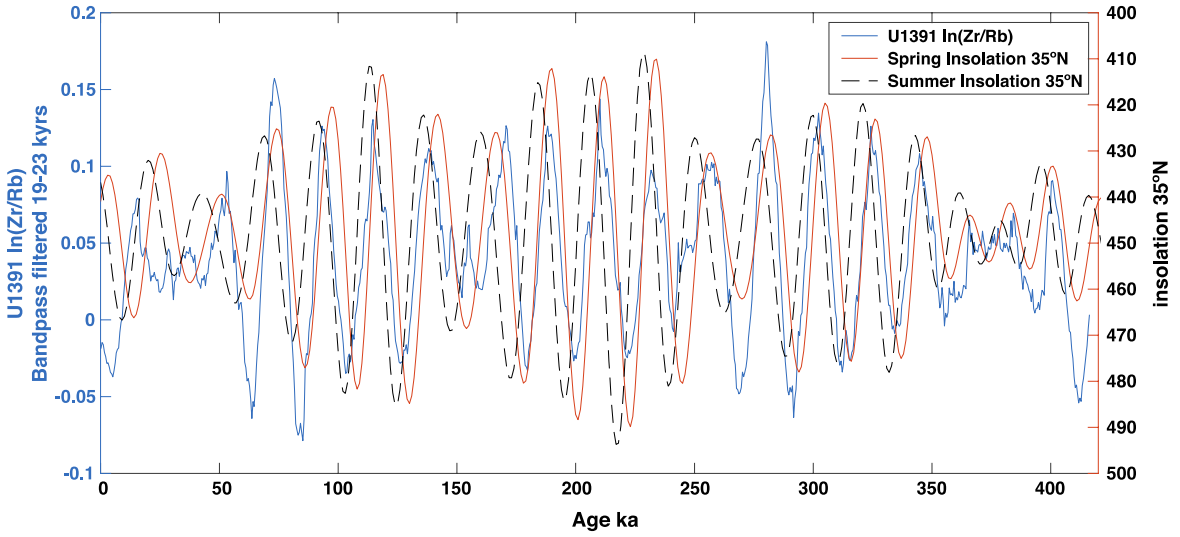

Figure 4.8. U1391 ln(Zr/Rb) compared with insolation at spring 35°N (orange) and summer 35°N (black dashed).

At precession minima, it is suggested that eastern Mediterranean winter precipitation is increased (Bosmans et al., 2020). At these precession minima, where we observe weaker MOW at Site U1391 (lower ln(Zr/Rb)), MOW variations lag behind spring insolation, whereas it leads summer insolation. This implies that precession paced winter/spring P-E changes over the eastern Mediterranean are more important for MOW strength variability, and intermediate and deep-water formation in the Mediterranean, compared with summer insolation-forced African monsoon freshwater run-off.

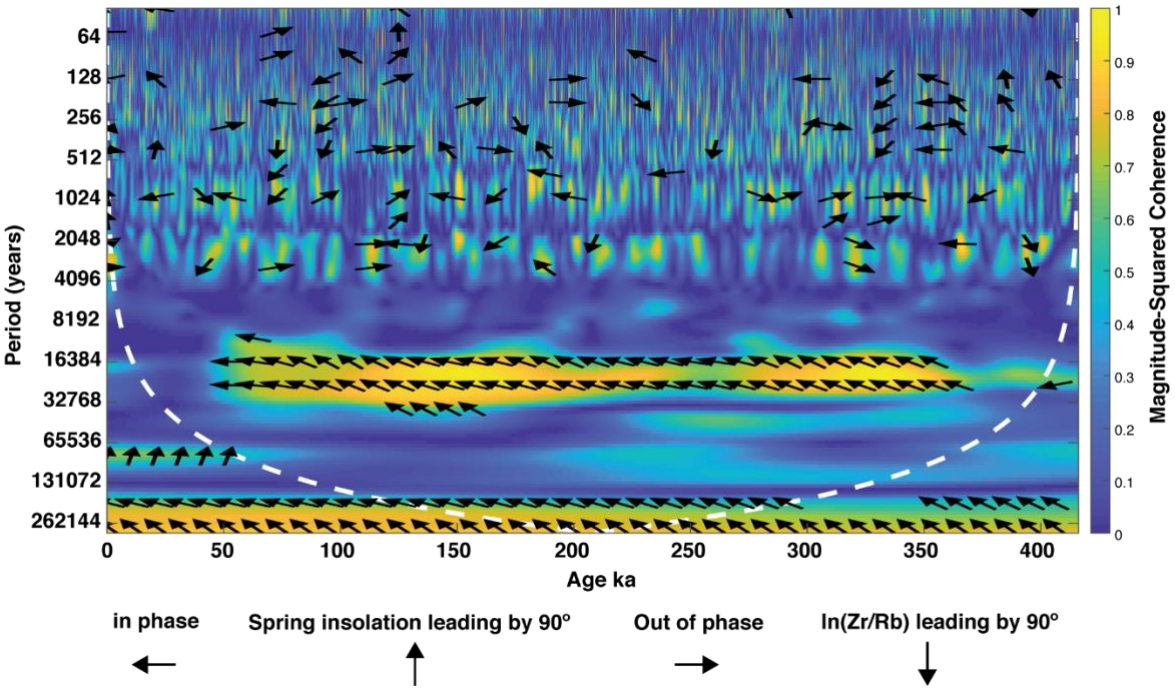

Figure 4.9. Wavelet coherence between spring insolation at 60N (x) and ln(Zr/Rb) (y). Phase arrows in black. As lower insolation values have been shown to correlate with higher ln(Zr/Rb) values, arrows pointing to the left indicate that they are in phase, pointing right out of phase, pointing up x leading y by 90 degrees and pointing down y leading x by 90 degrees. Strong coherence is observed in precession periods between 60 and 360 ka. Arrows pointing NW across this region show lows in spring insolation leads highs in ln(Zr/Rb).

Given the turnover time of the modern Mediterranean is in the order of a few hundred years (e.g. Rohling et al., 2015), other mechanisms must be invoked to fully explain this lag time. The mean lag time we calculate (~1.6 kyrs) is possibly analogous to the finding of the ~3 kyr lag between the mid-point of many Sapropels and peak summer insolation (Grant et al., 2016; Lourens et al., 1996). Modelling studies, however, find an instant response of summer monsoon to peak summer insolation. Ziegler et al. (2010) hypothesised that this discrepancy in findings could be due to suppression of boreal summer monsoon by North Atlantic cold events, which regularly occur just before insolation maxima. The cold events amplify wintertime forcing of deep-water formation in the eastern Mediterranean. Grant et al., (2016) found Sapropels S1 and S5 supported this hypothesis, however Sapropels S3 and S4 did not, implying cold events do not necessarily induce a lag between African monsoon and sapropel deposition, and that some other mechanism is likely significant. Instead, they put forward the hypothesis that the duration of meltwater addition into the North Atlantic disrupts the precession-pacing of the African monsoon.

It is conceivable that these meltwater pulses also affect winter precipitation in the Mediterranean, causing a, similarly timed, ~2 to 3 kyr delay in the increased activity of Atlantic

storm tracks. This would have the effect of delaying the timing of reduction in LIW formation rates and subsequently MOW strength.

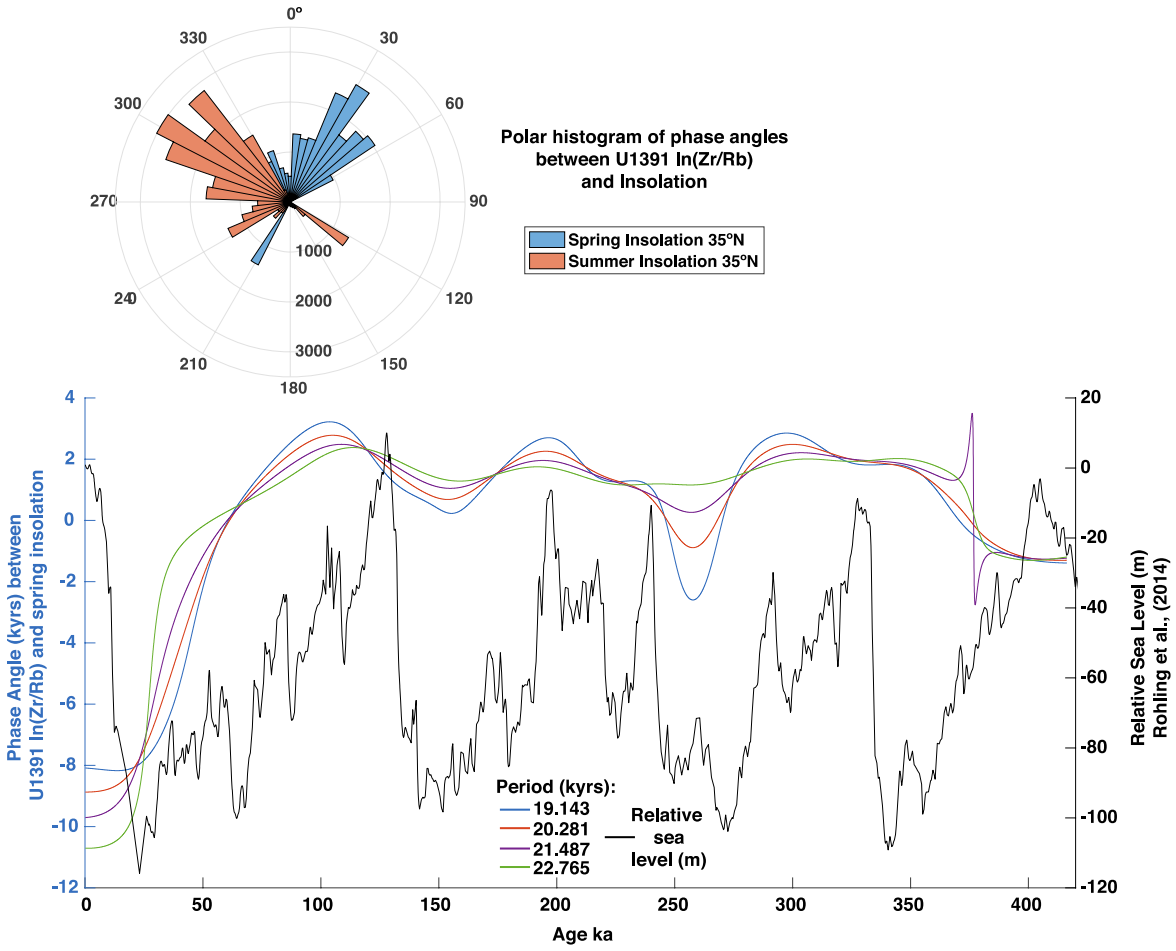

Figure 4.10. A) Polar histogram of phase angles between U1391 ln(Zr/Rb) and both spring and summer insolation at 35N. B) Phase angles (converted to years) between U1391 ln(Zr/Rb) and spring insolation at 35N at precession periodicities through time. Positive years indicates spring insolation is leading U1391 ln(Zr/Rb). Relative sea level at Gibraltar (Rohling et al., 2014) for climate reference.

Notably, the phase angle between ln(Zr/Rb) and spring insolation is variable through time (Figure 4.10). The first and last ~20 kyrs of the record lie outside the cone of influence for precession phase angles and so will be subject to edge effects. During the latest ~60 ka and between 416 and ~370 ka there is a significant shift in phase angles. This is likely due to the lack of precession power in these intervals and the prevalence of millennial scale variability. Between ~360 and ~60 ka, the phase angle appears to display a glacial-interglacial cyclicity, with greater phase lag at interglacials and decreasing phase at glacial stages, closer to ~3 kyrs and ~0 kyrs respectively (Figure 4.10). This may suggest that the potential process of storm track intensification delay by meltwater pulses became less significant at glacial intervals.

Over the latest ~130 kyrs, ln(Zr/Rb) at U1391 matches the Ehrmann et al. (2017) clay minerology (kaolinite/chlorite ratio) record of African hydroclimate (Figure 2.3 in Chapter 2). Intriguingly this suggests a shift from winter insolation forced precipitation to summer insolation forced African hydroclimate control of MOW across MIS 5. This is possibly linked to the role of the 400 kyr eccentricity cycle which reduced precession amplitude and increased North African aridity (Trauth et al., 2009).

4.5 Conclusions

XRF (i.e. ln(Zr/Rb)) and magnetic grain size (i.e. κ_{ARM}/κ) proxy records from IODP Site U1391 sediments have been identified as best representing different physical size fractions of sediment, 33 – 43 μm and 8 - 19 μm (and likely sizes below 5 μm), respectively. Divergent behaviour of different grain size fractions is observed through time at Site U1391; however this is likely not due to the currents affecting coarse and fine fractions in opposite ways. The observation appears to result from different climatic processes (MOW and biogenic magnetite production) causing opposing behaviour at warm and cold intervals.

The weight percent of the 63 – 150 μm fraction is demonstrated to be inefficient at capturing MOW changes. This proxy appears to only record some of the major grain size changes but could not reveal precession paced variability. Caution is therefore advised when using this as a current speed indicator, as had been done in the literature, because significant amounts of information may be missing.

Evidence is presented of spring insolation forcing of MOW strength variability at Site U1391, as opposed to the commonly inferred summer insolation forced African hydroclimate. External sources of moisture, likely late winter storm tracks from the North Atlantic, increased late winter P-E across the eastern Mediterranean at precession minima, reducing the exchange at the Strait of Gibraltar and MOW strength at Site U1391. A phase lag of ~2-3 kyr between spring insolation and ln(Zr/Rb) is present at precession periods, implying a mechanism of delay that may be similar to the lag between summer insolation sapropel deposition in the eastern Mediterranean. Meltwater pulses into the North Atlantic may delay both the northward incursion of the African summer monsoon and the intensification of winter storm activity in the Mediterranean.

Chapter 5 Conclusions and Future Work

5.1 Chapter 2 Summary

A new high-resolution age model was constructed for IODP Site U1391 sediments covering the last ~416 kyr. This provided the basis for interpretation for all the work in this thesis and is fundamental for future work on the upper ~120 m of U1391 sediments.

Different MOW regimes were inferred based on modes of variability of strength and depth changes. This was determined from a combination of AMS and grain size proxies at IODP Sites U1391 and U1385. During MIS 10 to 5 MOW was on average shallower. Its isopycnal equilibration depth varied between glacial (present at Site U1391) and interglacial (above Site U1391) intervals. MOW Strength changes reconstructed using grain size proxies were strongly modulated by precession. Through MIS 5, MOW began to transition to a millennial scale dominated mode of variability and the equilibration depth deepened. From MIS 4 to present MOW switched between being present at U1391 during stadials and below at interstadials. As the eccentricity node reduced the amplitude of precession cycles, strength changes also exhibited millennial scale variability. These results likely have implications for the impact of MOW on North Atlantic circulation before MIS 5, as MOW exhibited an as yet undiscovered variability regime and was injected at shallower depths compared to the last glacial cycle.

5.2 Chapter 3 Summary

The third chapter uses environmental magnetic proxies at Site U1391 to document a range of environmental processes on the west Iberian Margin. The magnetic phases in Site U1391 sediments of the last ~130 kyr are dominated by detrital magnetite and a fine magnetite phase that is possibly biogenic in origin. The grain size and concentration of these phases were strongly controlled by northern high latitude climate variability through the action of temperature-controlled production of biogenic magnetite and sea level controlled detrital input. At some stadials an additional high coercivity component is present, possibly representing haematite derived from North African dust.

Before ~130 ka, relatively lower sedimentation rates and high levels of organic matter, particularly at interglacials MIS 7e, 9 and 11, led to enhanced reductive dissolution of fine-grained magnetite and the weakening of the primary magnetic signal. An increase in sedimentation rates, possibly

linked with the migration of MOW, during MIS 5 meant magnetic minerals in this interglacial were relatively less affected by reductive diagenesis.

Magnetic susceptibility and ln(Si/Sr) peaks at Site U1391 can be correlated with IRD events recorded in sediments across the North Atlantic, while other IRD events cannot be identified in these proxies at U1391. This further improves understanding of ice-rafting distribution and the polar front at these times.

5.3 Chapter 4 Summary

In Chapter 4, using an updated higher resolution physical grain size record, the relationship between magnetic (i.e. κ_{ARM}/κ) and XRF (i.e. ln(Zr/Rb)), and physical grain size proxies are explored in detail. Ln(Zr/Rb) is identified as best representing the 33 – 43 μm fraction. The weight percent of the 63 – 150 μm fraction, often used in the literature as a quick and convenient grain size proxy, is demonstrated to be inefficient at capturing precession paced changes in MOW.

Analysis of the phasing between MOW grain size records and insolation reveals information about forcings and phase lags within the climate system. U1391 grain size variability leads northern hemisphere summer insolation but lags behind spring insolation between ~370 and ~60 ka. This indicates that precession paced changes in late-winter precipitation and North Atlantic storm track activity may be the major factor forcing MOW changes rather than African monsoon during these time intervals. Additionally, the nature of the phase lag implies that these late winter processes are affected by a process analogous to the ~3 kyr phase lag between summer insolation and deposition of some sapropels due to meltwater pulses into the North Atlantic (Grant et al., 2016).

5.4 Future Work

5.4.1 Mediterranean outflow studies

The unique position the west Iberian Margin has in palaeoceanographic studies (e.g., the correlation of features from deep-sites with ice core variability from both poles) means there are many potential investigations that could be conducted using Site U1391 sediments. As shown in Chapter 2, Site U1391 can be closely tied to Site U1385. The relatively shallow position of Site U1391 could be exploited to compare intermediate water mass behaviour with millennial scale ice sheet and deep-water mass variability through the late Pleistocene. The most elusive aspect of

MOW research remains what its exact effects are on Atlantic circulation. Studying this was beyond the scope of this thesis, however it is plausible that some answers may be found in exploiting the direct links in west Iberian Margin sediments between MOW, AMOC and ice-core proxies.

Recent studies based on sediments from IODP Expedition 339 have enhanced our understanding of MOW behaviour and variability, however many gaps remain. To build a more complete picture of MOW variability through the late Pleistocene, it may be a fruitful exercise to compare MOW records from the Gulf of Cadiz and those from the west Iberian Margin, particularly from the IODP Expedition 339 Sites.

IODP Site U1390 is located in the Gulf of Cadiz, under the influence of the MOW. The Site has exceptionally high sedimentation rates, ~75 cm/kyr (Expedition 339 Scientists, 2013b). Three samples (and one background) were selected and had C14 dates produced to improve the age model in the upper section of the core. Studies on these sediments could allow one to constrain MOW variability on very short timescales (~ hundreds of years) over the last glacial cycle. Comparison of MOW records to Site U1391 and others in the Gulf of Cadiz could help reconstruct MOW variability spatially on these short timescales.

Construction of deeper records at Site U1391 could be used to test MOW migration across multiple 400 kyr eccentricity cycles to examine whether we see a deeper MOW through MIS 11 and 12, similar to the eccentricity node of the last glacial cycle. This could be investigated via further XRF scanning and comparison to U1385, and analysis of the deeper AMS record based on shipboard cube samples. However, due to suspected reductive diagenesis and a lack of u-channel samples at these depths, declination corrections for AMS data produced from these samples will be of lower reliability.

To further constrain MOW vertical migration through the late Pleistocene, the recovery of long sediment sequences from deeper (1500 – 2000 mbsl) and shallower (500 – 1000 mbsl) sites on the west Iberian Margin would be useful. This would allow the collection of data with direct MOW influence at times of different Atlantic injection depths. AMS data from these deeper and shallower sites, creating a depth transect, would confirm the conclusions regarding MOW vertical migration in Chapter 2. A pilot study could be conducted on the short sediment cores recovered from IODP site survey cruise JC089 (Hodell et al., 2014) which cover a range of water depths on the west Iberian Margin.

To lend weight to the conclusions drawn in Chapter 4, that MOW is not primarily driven by African hydroclimate changes, one could directly compare the phasing of U1391 grain size records with

an African hydroclimate record of similar length. One prerequisite is that the comparison records must have a strong chronology to resolve the timing of precession paced cycles. Some initial analysis has been completed comparing U1391 ln(Zr/Rb) to a dust record (ln(Zr/Al) at ODP Site 658 on the west African Margin. This site has a long record (>500 ka) and shows clear summer insolation paced dust cycles. However, the age model is constructed from only several tie points between benthic oxygen isotopes and the LR04 stack (Lisiecki & Raymo, 2005). It is therefore deemed not robust enough to make conclusions about the phasing with precession paced insolation cycles. Future work will try to strengthen this age model to make phasing analysis possible.

In order to independently test for the presence or absence of MOW at certain water depths on the west Iberian Margin, it has been hypothesised that the Mediterranean sourced water could be identified by a carbonate ion concentration that is distinct from North Atlantic water masses. This would be recorded by the ratio of B/Ca in benthic foraminifera. The feasibility of such a study was briefly explored, with the main potential limiting factors being twofold: i) Would there be a significant enough distinction in omega calcite between ambient Atlantic water and MOW on the west Iberian Margin to be detected by B/Ca of benthic foraminifera? And ii) Would the mass of available monospecific benthic foraminifera be high enough to acquire reliable measurements? Based on preliminary estimations, in principle, MOW presence should be detectable at Site U1391 through measurement of B/Ca in benthic foraminifera. Assemblage counts from Guo et al. (2017) show that approximately 20 cm^3 of bulk sediment would be required for 8 – 12 benthic foraminifera specimens, depending on species, which should be enough mass for the measurement (Foster per. comm. 2018). A pilot study would be proposed to compare B/Ca from Site U1391 with both shallower and deeper Iberian Margin sites as controls. A record covering the Holocene, LGM and stadial–interstadial behaviour would be recommended to capture intervals of vertical MOW migration.

5.4.2 Environmental magnetic studies

Several additional types of analysis could be undertaken to support the conclusions of Chapter 3. Direct identification of IRD in samples (for example, under a microscope) could confirm the observations from magnetic and XRF proxies. Scanning electron microscopy (SEM) and transmission electron microscopy (TEM) analysis could be used to identify magnetic minerals and confirm the presence of the inferred biogenic magnetite.

Reflectance spectroscopy can be used to infer downcore changes in haematite concentration. Collecting this data from U1391 cores could contribute to the discussion around the source of Haematite and provide interesting comparisons for other haematite proxies, the S-Ratio for example. The use of existing IODP shipboard reflectance data was explored but the curves were deemed not reliable enough due to a, now, known machine deficiency on board at the time.

In addition to the environmental magnetic studies, natural remanent magnetisation records have been produced for Site U1391. These will be analysed to produce a high-resolution relative palaeointensity record for the Site, shedding light on the detailed variation of Earth's magnetic field (Xuan and Nichols, in prep).

5.4.3 West African Margin

ODP Site 659 on the west African Margin sits beneath the Saharan summer dust plume, which is known to contain high quantities of haematite and/or goethite. Both of these minerals have high coercivities. Some preliminary rock magnetic measurements (hysteresis loops, IRM acquisition and high temperature susceptibility; (Appendix B) were completed on samples at selected intervals through the last 10 Ma, with the aim of characterising haematite and goethite variations in the marine sediments.

Results hint at the presence of hematite, but the signal proved challenging to disentangle from other magnetic minerals, likely because haematite carries a relatively weak magnetisation compared to other magnetic minerals such as magnetite (Frank & Nowaczyk, 2008; Roberts et al., 2020). It was difficult to correlate the results with existing dust proxies such as log(Ca/Fe) or results from previously published environmental magnetic studies (Bloemendal et al., 1986).

Future analysis could use alternate rock magnetic techniques to more effectively isolate the high coercivity signal, such as low temperature susceptibility experiments, FORCs and SEM imaging.

5.4.4 XRF Core Scanner Comparison

The top 20 u-channel sections of U1391, comprising the latest ~63 ka, have been scanned on both an ITRAX and an Avaatech XRF core scanner. This work was undertaken to ensure comparisons with other XRF records scanned on different machines were reliable. These two datasets present an opportunity to further characterise the differences in results between the ITRAX and Avaatech

machines. Initial comparisons suggest there is strong correspondence in measurements of major element ratios such as Ca/Ti, however for lighter elements, nearer detection limits, there is more variation between the two machines (Figure S8 in Appendix D). To take the work further X-ray diffraction (XRD) analysis could be undertaken at selected intervals at the top of Site U1391 sediments to test each core-scanner's results against.

Appendix A Age Model Tie Points

Table 1. Age model tie points for IODP Site U1391. Category refers to the level of confidence associated with each tie point, from A, at very confident, to C, at lower confidence. All tie points were used as this provided the best correlation between the ln(Ca/Ti) records of IODP Sites U1391 and U1385.

CCSF (m)	Age (ka)	Category
0	0	C
0.257	1.09	C
0.3687	1.86	B
1.0071	4.23	B
1.8078	7.38	A
1.9528	8.27	B
2.1923	9.34	C
2.8602	11.65	C
3.2402	13.16	C
4.7457	16.17	A
5.798	16.99	A
6.575	21.37	A
8.8897	27.29	B
9.6371	30.32	B
10.22	31.49	B
10.34	32.07	B
11.21	35.05	B
12.087	36.81	A
13.45	39.11	B
13.95	39.62	A
15.14	42.47	A
15.2906	43.05	B
15.6856	44.49	C
16.89	47.41	C
17.9222	47.98	B

CCSF (m)	Age (ka)	Category
18.17	48.97	A
19.92	54.05	A
20.13	54.43	A
20.35	54.72	A
20.65	55.44	B
20.94	56.11	B
21.1974	57.37	C
21.51	58.69	B
21.97	60.08	A
22.27	61	A
22.39	61.2	B
22.54	61.53	A
24.9115	64.91	C
25.1865	66.82	C
25.3665	70.73	C
25.89	73.01	A
26.16	74.42	B
26.52	76.68	A
26.73	78.33	B
27.71	82.93	A
28.48	84.62	B
29.8	87.28	A
30.21	88.7	C
30.86	91.65	B
33.0917	103.47	A
33.2017	103.69	A
33.25	103.8	A
33.92	105.4	A
34.1	106.2	A
34.4	109.2	A
34.95	110.9	A

CCSF (m)	Age (ka)	Category
36.79	121.4	B
37.95	128.2	A
39.57	132.6	B
41.56	136.1	A
42.0965	140.69	B
42.8915	145.07	C
43.2066	145.82	C
46.0614	150.5	C
47.7917	156.5	C
51.3166	171.56	B
52.9864	179.82	C
53.2614	186.75	C
54.1667	190.05	C
54.74	192	A
54.98	193.31	A
55.49	194.3	A
56.47	197.4	A
57.1	200.3	B
57.91	202.9	A
58.82	207.5	C
59.85	211.6	C
61.89	219.3	A
64.2561	223.44	B
64.45	226.3	A
64.82	227.75	B
66.227	234.59	A
69.51	239	A
70.3065	241.63	A
71.57	245.3	A
72.4	248.4	A
74.8	258.1	A

CCSF (m)	Age (ka)	Category
75.37	260	A
76.09	262.2	A
76.49	264.4	A
83.3767	275.71	A
83.57	277.2	A
83.95	279.3	A
86.19	292.6	A
86.3	292.8	A
88.6527	295.68	A
89.3258	296.23	A
89.4658	297.77	B
89.7094	299.95	B
89.99	300.8	A
90.64	305.89	A
91.51	307.8	A
91.86	309	A
92.22	310.9	B
93.15	315	A
93.43	316	B
93.64	316.9	A
93.92	317.4	A
94.24	318.2	A
95.234	320.5	A
99.1768	336.16	A
99.5163	337.28	B
100.5108	338.25	B
102.5557	340.57	B
102.6707	340.81	B
102.8357	342.53	C
103.1791	344.32	C
103.2441	345.4	A

CCSF (m)	Age (ka)	Category
103.4741	345.9	A
103.6854	347.77	A
103.8354	348.5	B
107.8262	370.5	B
108.1512	371.7	B
108.2112	372.04	C
108.3423	372.38	B
109.7013	379.24	B
109.8707	379.69	A
110.4607	381.12	A
110.7	383.34	B
110.9207	384.42	C
111.5238	387.1	A
112.5696	388.7	A
113.6446	391.48	B
114.477	392.52	B
114.67	394.4	A
120.3603	414.78	B
120.64032	416.31	C

Appendix B Chapter 2 Supplementary Material

Table 2. AMS parameters, formulas and meanings.

Parameter	**Term**	**Formula**	**Contextual Meaning**
Corrected Degree of Anisotropy	P_j	$\exp\left(\sqrt{2\left(\begin{pmatrix}\ln(k1-k)^2+\\ \ln(k2-k)^2+\\ \ln(k3-k)^2\end{pmatrix}\right)}\right)$	Intensity of the preferred orientation of the magnetic minerals
Shape	T	$\frac{(2\ln(k2))-\ln(k1)-\ln(k3)}{\ln(k1)-\ln(k3)}$	Symmetry, and therefore shape, of the AMS ellipsoid
Lineation	L	$\frac{k1}{k2}$	Commonly generated by the shear stress acting tangentially on the bed, e.g., a current
Foliation	F	$\frac{k2}{k3}$	Produced mostly by gravitational settling of particles in quiet water
Magnetic Fabric	q	$\frac{k1-k2}{\left(\frac{k1+k2}{2}-k3\right)}$	Compares the intensity of alignment in the lineation direction (L) with that on the foliation plane (F) giving a quantitative description of the magnetic fabric and depositional regime
Beta	β	$90-k3inc$	Imbrication of foliation along the bedding plane

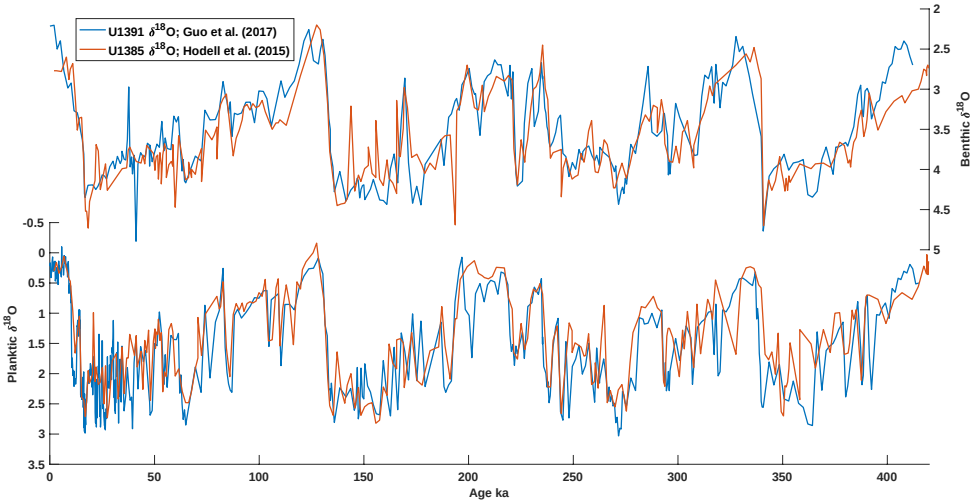

Figure S1. Benthic (top panel) and planktic (bottom panel) $\delta^{18}O$ records from Site U1391 (Guo et al., 2017) plotted on the constructed age model and compared with $\delta^{18}O$ records from Site U1385 (Hodell et al., 2015).

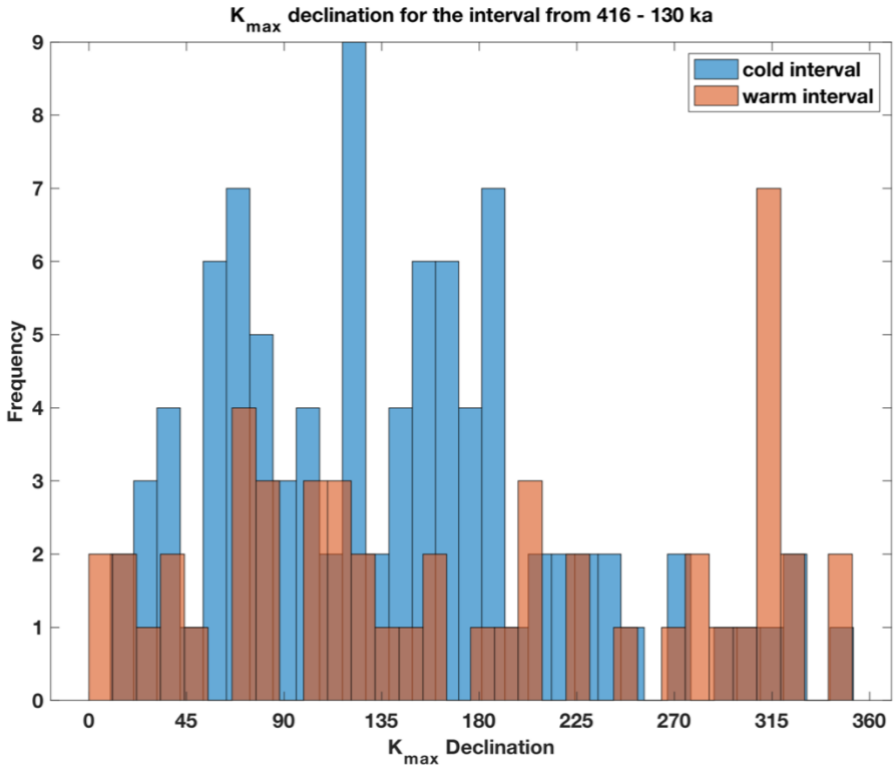

Figure S2. Histogram of κ_{max} declination data from ~416-130 ka. Orange bars represent warm intervals and blue bars represent cold intervals.

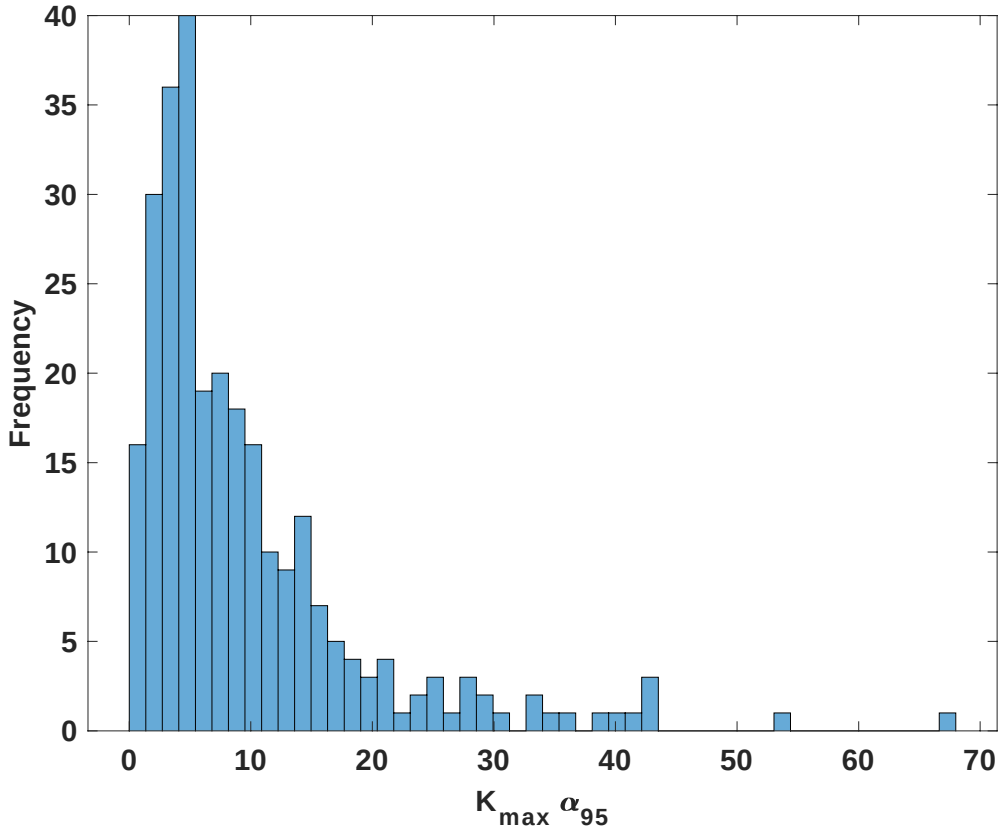

Figure S3. Histogram of α_{95} values associated with κ_{max} directional data of all studied Site U1391 cube samples.

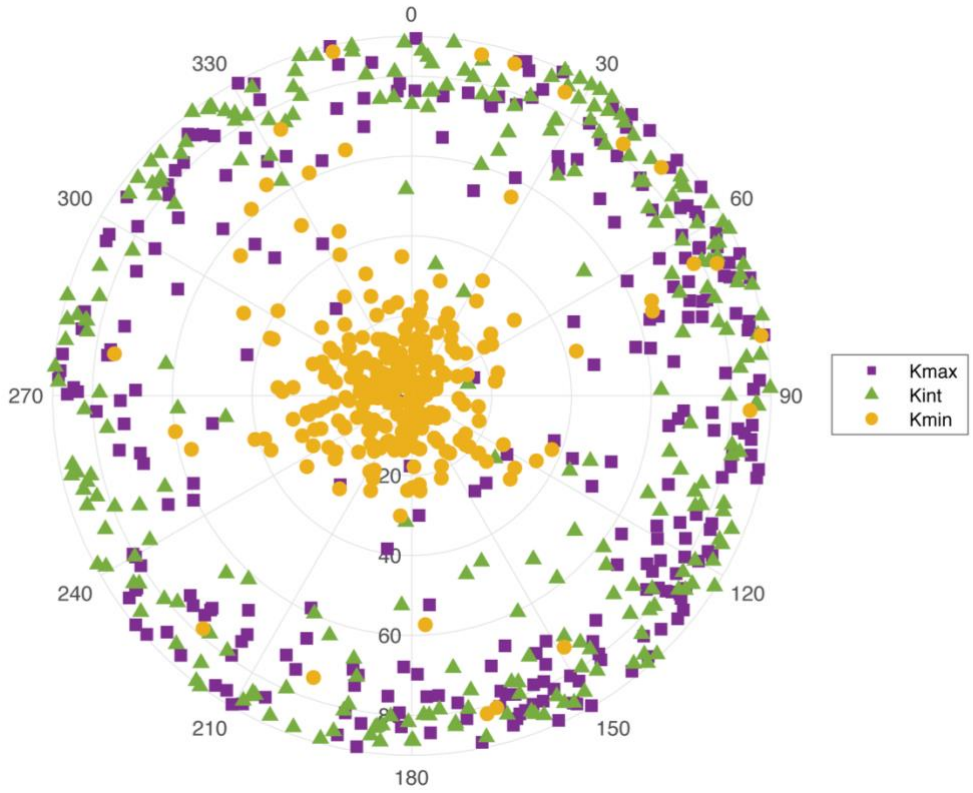

Figure S4. Lower hemisphere projection of κ_{max}, κ_{int} and κ_{min} declination and inclination values from Site U1391 cube samples.

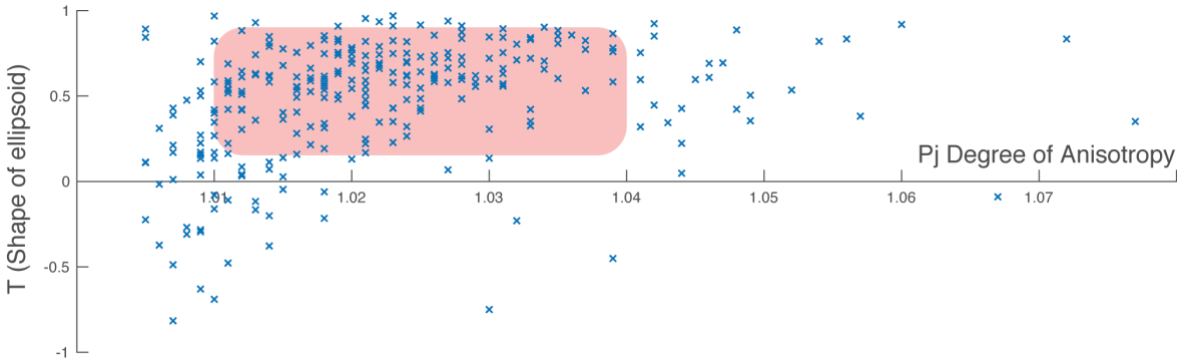

Figure S5. Pj vs T scatter plot for U1391 cube samples. Values approximately falling in the highlighted field indicate the influence of a current (Joseph et al., 1998).

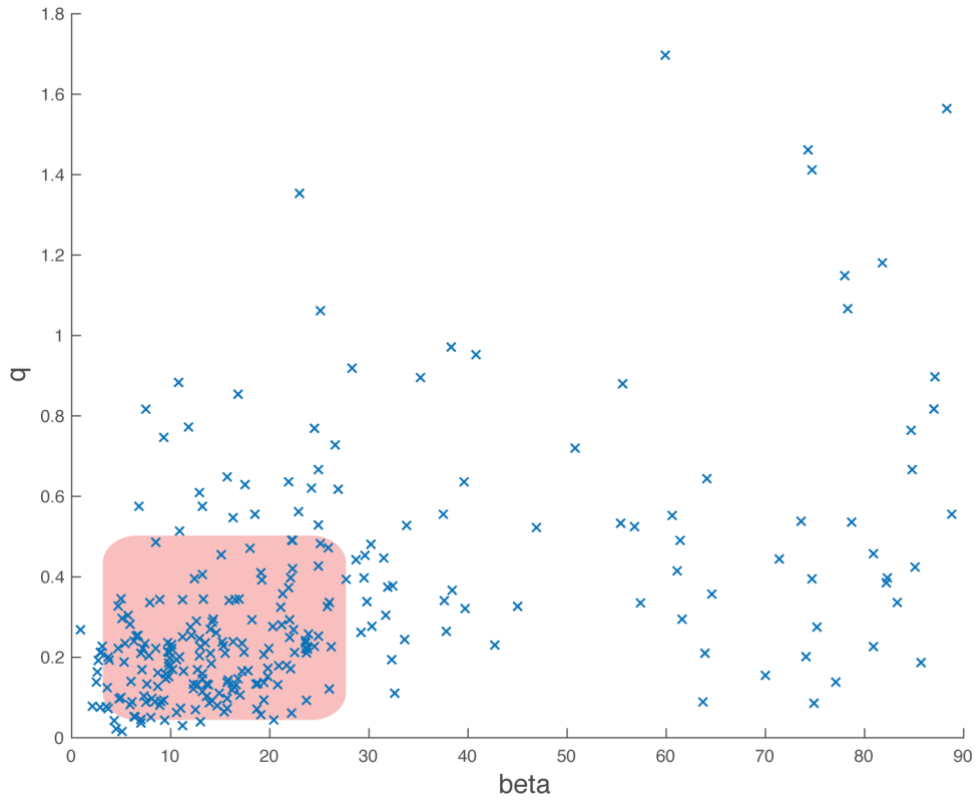

Figure S6. q vs beta scatter plot for U1391 cube samples. Values approximately falling in the highlighted field indicate the influence of a current (Novak et al., 2014; Taira, 1989).

Appendix C Environmental Magnetic Results from ODP Site 659

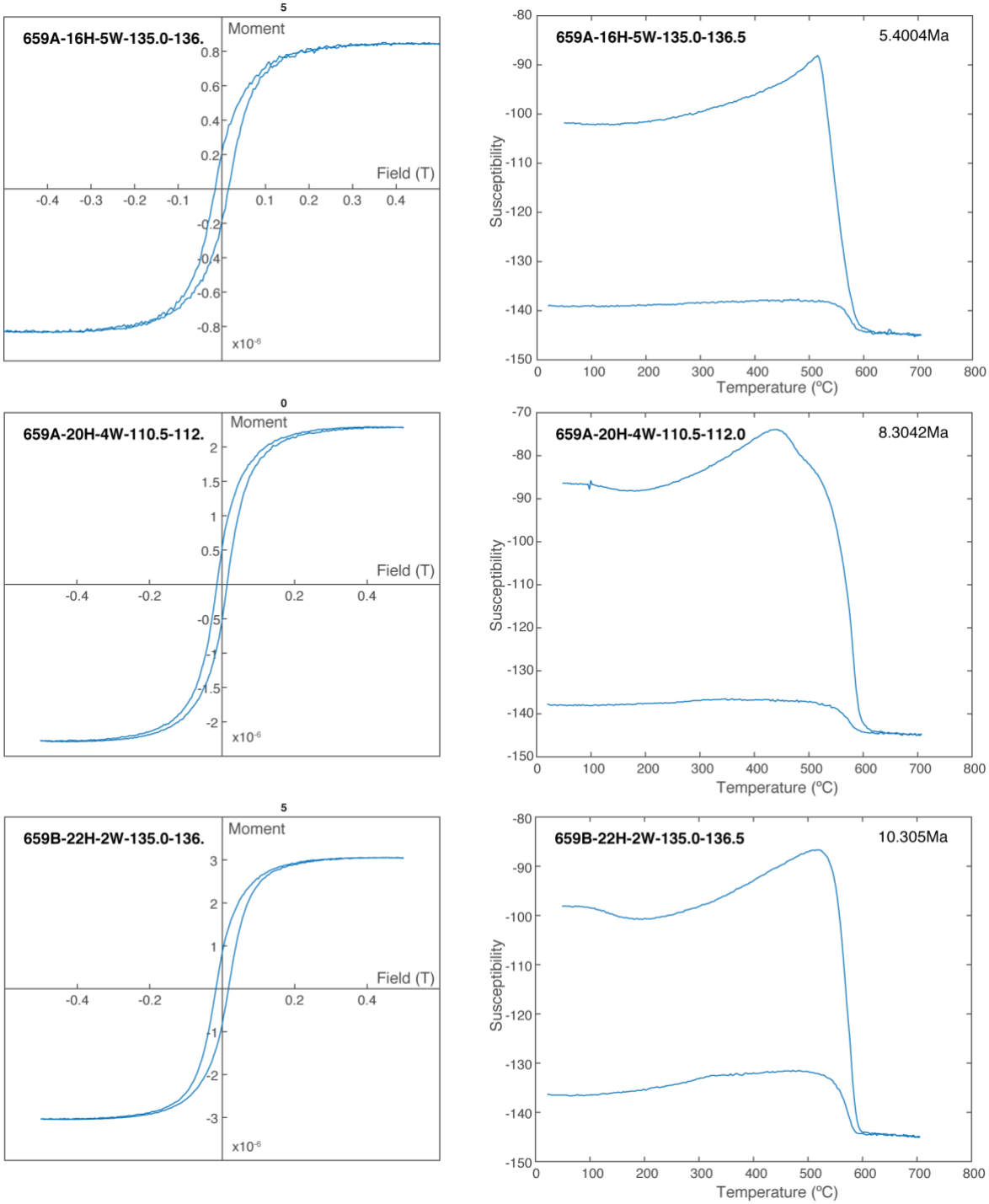

Figure S7. Selected environmental results magnetic results from ODP Site 659 on the west African Margin.

Appendix D ITRAX vs Avaatech Comparison

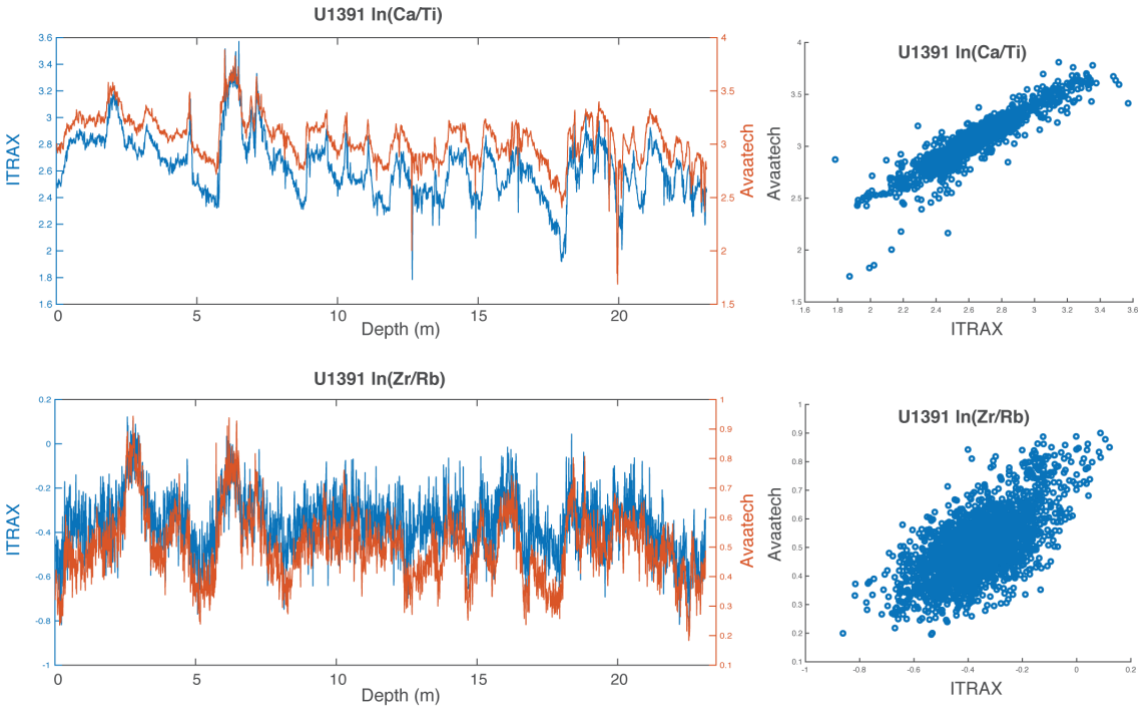

Figure S8. Avaatech vs ITRAX comparison of ln(Ca/Ti) and ln(Zr/Rb) for the top ~23 m of U1391 sediments.

List of References

Arístegui, J., Alvarez-Salgado, X. A., Barton, E. D., Figueiras, F. G., Hernandez-Leon, S., Roy, C., & Santos, A. (2006). Oceanography and fisheries of the canary current/Iberian region of the eastern North Atlantic (18a, E). In The Global Coastal Ocean: Interdisciplinary Regional Studies and Syntheses (Vol. 14, pp. 879–931). Cambridge, MA, USA: Harvard University Press.

Bahr, A., Jiménez-Espejo, F. J., Kolasinac, N., Grunert, P., Hernández-Molina, F. J., Röhl, U., et al. (2014). Deciphering bottom current velocity and paleoclimate signals from contourite deposits in the Gulf of Cádiz during the last 140 kyr: An inorganic geochemical approach. Geochemistry, Geophysics, Geosystems, 15, 3145–3160. https://doi.org/10.1002/2014gc005356

Bahr, A., Kaboth, S., Hodell, D., Zeeden, C., Fiebig, J., & Friedrich, O. (2018). Oceanic heat pulses fuelling moisture transport towards continental Europe across the mid-Pleistocene transition. Quaternary Science Reviews, 179, 48–58. https://doi.org/10.1016/j. quascirev.2017.11.009

Bahr, A., Kaboth, S., Jiménez-Espejo, F. J., Sierro, F. J., Voelker, A. H. L., Lourens, L., et al. (2015). Persistent monsoonal forcing of Mediterranean Outflow Water dynamics during the late Pleistocene. Geology, 43(11), 951–954. https://doi.org/10.1130/G37013.1

Banerjee, S. K., King, J. W., & Marvin, J. (1981). A rapid method for magnetic granulometry with applications to environmental studies. Geophysical Research Letters, 8(4), 333-336.

Barker, S., Chen, J., Gong, X., Jonkers, L., Knorr, G., & Thornalley, D. (2015). Icebergs not the trigger for North Atlantic cold events. Nature, 520(7547), 333-336. doi:10.1038/nature14330

Barker, S., Knorr, G., Edwards, R. L., Parrenin, F., Putnam, A. E., Skinner, L. C., et al. (2011). 800,000 years of abrupt climate variability. Science, 334(6054), 347–351. https://doi.org/10.1126/science.1203580

Becker, K. (2014). Chapter 1 - Major Scientific Achievements of the Integrated Ocean Drilling Program: Overview and Highlights. In R. Stein, D. K. Blackman, F. Inagaki, & H.-C. Larsen (Eds.), Developments in Marine Geology (Vol. 7, pp. 1-36): Elsevier.

Berner, R. A. (1981). A new geochemical classification of sedimentary environments. Journal of Sedimentary Research, 51(2), 359-365.

Bianchi, G. G., & McCave, I. N. (1999). Holocene periodicity in North Atlantic climate and deep-ocean flow south of Iceland. Nature, 397(6719), 515-517.

Bloemendal, J., King, J. W., Hall, F. R., & Doh, S. J. (1992). Rock magnetism of Late Neogene and Pleistocene deep-sea sediments: Relationship to sediment source, diagenetic processes, and sediment lithology. Journal of Geophysical Research, 97(B4). doi:10.1029/91jb03068

Bloemendal, J., King, J., Tauxe, L., & Valet, J. (1986). 25. ROCK-MAGNETIC STRATIGRAPHY OF LEG 108 SITES 658, 659, 661, AND 665, EASTERN TROPICAL ATLANTIC. Paper presented at the Proceedings of the Ocean Drilling Program: Scientific results.

Blott, S. J., & Pye, K. (2001). GRADISTAT: a grain size distribution and statistics package for the analysis of unconsolidated sediments. Earth Surface Processes and Landforms, 26(11), 1237-1248. doi:10.1002/esp.261

Bond, G. C., Showers, W., Elliot, M., Evans, M., Lotti, R., Hajdas, I., . . . Johnson, S. (1999). The North Atlantic's 1-2 kyr climate rhythm: relation to Heinrich events, Dansgaard/Oeschger cycles and the Little Ice Age. Geophysical Monograph-American Geophysical Union, 112, 35-58.

Böning, P., Bard, E., & Rose, J. (2007). Toward direct, micron-scale XRF elemental maps and quantitative profiles of wet marine sediments.pdf. Geochem Geophys Geosyst, 8(Q05004). doi:10.1029/2006GC001480

Bosmans, J. H. C., Drijfhout, S. S., Tuenter, E., Hilgen, F. J., Lourens, L. J., & Rohling, E. J. (2015). Precession and obliquity forcing of the freshwater budget over the Mediterranean. Quaternary Science Reviews, 123, 16–30. https://doi.org/10.1016/j.quascirev.2015.06.008

Bosmans, J. H. C., van der Ent, R. J., Haarsma, R. J., Drijfhout, S. S., & Hilgen, F. J. (2020). Precession- and obliquity-induced changes in moisture sources for enhanced precipitation over the Mediterranean Sea. Paleoceanography and Paleoclimatology, 36. e2019PA003655 https://doi.org/10.1029/2019PA003655

Buurman, P., Pape, T., Reijneveld, J. A., de Jong, F., & van Gelder, E. (2001). Laser-diffraction and pipette-method grain sizing of Dutch sediments: correlations for fine fractions of marine, fluvial, and loess samples. Netherlands Journal of Geosciences - Geologie en Mijnbouw, 80(2), 49-57. doi:10.1017/s0016774600022319

Canfield, D. E. (1989). Reactive iron in marine sediments. Geochimica et Cosmochimica Acta, 53(3), 619-632.

Canfield, D. E., & Thamdrup, B. (2009). Towards a consistent classification scheme for geochemical environments, or, why we wish the term ‘suboxic’would go away. Geobiology, 7(4), 385-392.

Channell, J. E. T., Hodell, D. A., Margari, V., Skinner, L. C., Tzedakis, P. C., & Kesler, M. S. (2013). Biogenic magnetite, detrital hematite, and relative paleointensity in Quaternary sediments from the Southwest Iberian Margin. Earth and Planetary Science Letters, 376, 99-109. doi:10.1016/j.epsl.2013.06.026

Channell, J. E. T., Hodell, D. A., Romero, O., Hillaire-Marcel, C., de Vernal, A., Stoner, J. S., . . . Röhl, U. (2012). A 750-kyr detrital-layer stratigraphy for the North Atlantic (IODP Sites U1302–U1303, Orphan Knoll, Labrador Sea). Earth and Planetary Science Letters, 317-318, 218-230. doi:10.1016/j.epsl.2011.11.029

Croudace, I. W., Löwemark, L., Tjallingii, R., & Zolitschka, B. (2019). Current perspectives on the capabilities of high resolution XRF core scanners. Quaternary International, 514, 5-15. doi:10.1016/j.quaint.2019.04.002

Datema, M., Sangiorgi, F., de Vernal, A., Reichart, G.J., Lourens, L.J., Sluijs, A. (2017). Comparison of qualitative and quantitative dinoflagellate cyst approaches in reconstructing glacial-interglacial climate variability at West Iberian Margin IODP 'Shackleton' Site U1385. Marine Micropaleontology, 136, 14-29. https://doi.org/10.1016/j.marmicro.2017.08.003

Day, R., Fuller, M., & Schmidt, V. A. (1977). Hysteresis properties of titanomagnetites: grain-size and compositional dependence. Physics of the Earth and Planetary Interiors, 13, 260-267.

Dunlop, D. J. (2002). Theory and application of the Day plot (Mrs/MsversusHcr/Hc) 2. Application to data for rocks, sediments, and soils. Journal of Geophysical Research, 107(B3). doi:10.1029/2001jb000487

Dypvik, H., & Harris, N. B. (2001). Geochemical facies analysis of fine-grained siliciclastics using Th/U, Zr/Rb and (Zr+ Rb)/Sr ratios. Chemical Geology, 181(1-4), 131-146.

Egli, R. (2004). Characterization of individual rock magnetic components by analysis of remanence curves, 1. Unmixing natural sediments. Studia Geophysica et Geodaetica, 48, 391-446.

Egli, R. (2004). Characterization of individual rock magnetic components by analysis of remanence curves, 1. Unmixing natural sediments. Studia Geophysica et Geodaetica, 48, 391-446.

Egli, R. (2013). VARIFORC: An optimized protocol for calculating non-regular first-order reversal curve (FORC) diagrams. Global and Planetary Change, 110, 302-320. doi:10.1016/j.gloplacha.2013.08.003

Ehrmann, W., Schmiedl, G., Beuscher, S., & Krüger, S. (2017). Intensity of African humid periods estimated from Saharan dust fluxes. PLoS ONE, 12(1). https://doi.org/10.1371/journal.pone.0170989

Expedition 339 Scientists (2012). Mediterranean outflow—Environmental significance of the Mediterranean outflow water and its global implications (IODP Prel. Rept., 339). Tokyo: Integrated Ocean Drilling Program Management International, Inc.

Expedition 339 Scientists (2013a). Site U1385. In D. Stow, F. J. Hernandez-Molina, C. A. A. Zarikian, & E. Scientists (Eds.), Proc. IODP (Vol. 339). Tokyo: Integrated Ocean Drilling Program Management International, Inc. https://doi.org/10.2204/iodp.proc.339.103.2013

Expedition 339 Scientists. (2013b). Site U1390. In D. Stow, F. J. Hernández-Molina, C. A. A. Zarikian, & E. Scientists (Eds.), Proc. IODP (Vol. 339). Tokyo: Integrated Ocean Drilling Program Management International, Inc.

Expedition 339 Scientists (2013c). Site U1391. In D. Stow, F. J. Hernandez-Molina, C. A. A. Zarikian, & E. Scientists (Eds.), Proc. IODP (Vol. 339). Tokyo: Integrated Ocean Drilling Program Management International, Inc.

Folk, R. L. (1980). Petrology of Sedimentary Rocks. Austin, Texas: Hemphill Publishing Co.

Frank, U., & Nowaczyk, N. R. (2008). Mineral magnetic properties of artificial samples systematically mixed from haematite and magnetite. Geophysical Journal International, 175(2), 449-461.

Froelich, P. N., Klinkhammer, G., Bender, M. L., Luedtke, N., Heath, G. R., Cullen, D., . . . Maynard, V. (1979). Early oxidation of organic matter in pelagic sediments of the eastern equatorial Atlantic: suboxic diagenesis. Geochimica et Cosmochimica Acta, 43(7), 1075-1090.

Funk, J. A., von Dobeneck, T., & Reitz, A. (2003a). Integrated Rock Magnetic and Geochemical Quantification of Redoxmorphic Iron Mineral Diagenesis in Late Quaternary Sediments from the Equatorial Atlantic. In G. Wefer, S. Mulitza, & V. Ratmeyer (Eds.), The South Atlantic in the Late Quaternary: Reconstruction of Material Budgets and Current Systems. Berlin, Heidelberg: Springer.

Funk, J. A., von Dobeneck, T., Wagner, T., & Kasten, S. (2003b). Late Quaternary Sedimentation and Early Diagenesis in the Equatorial Atlantic Ocean: Patterns, Trends and Processes Deduced from Rock Magnetic and Geochemical Records. In G. Wefer, S. Mulitza, & V. Ratmeyer (Eds.), The

South Atlantic in the Late Quaternary: Reconstruction ofMaterial Budgets and Current Systems (pp. 461-497). Berlin Heidelberg New York Tokyo: Springer.

García-Gallardo, Á., Grunert, P., & Piller, W. E. (2017a). Variations of Mediterranean-Atlantic exchange across the late Pliocene climate transition. Climate of the Past Discussions, 1–25. https://doi.org/10.5194/cp-2017-134

García-Gallardo, Á., Grunert, P., Voelker, A. H. L., Mendes, I., & Piller, W. E. (2017b). Re-evaluation of the "elevated epifauna" as indicator of Mediterranean Outflow Water in the Gulf of Cadiz using stable isotopes ($\delta^{13}C$, $\delta^{18}O$). Global and Planetary Change, 155, 78–97. https://doi.org/10.1016/j.gloplacha.2017.06.005

Grant, K. M., Grimm, R., Mikolajewicz, U., Marino, G., Ziegler, M., & Rohling, E. J. (2016). The timing of Mediterranean sapropel deposition relative to insolation, sea-level and African monsoon changes. Quaternary Science Reviews, 140, 125-141. doi:10.1016/j.quascirev.2016.03.026

Grant, K. M., Rohling, E. J., Westerhold, T., Zabel, M., Heslop, D., Konijnendijk, T., & Lourens, L. (2017). A 3 million year index for North African humidity/aridity and the implication of potential pan-African Humid periods. Quaternary Science Reviews, 171, 100-118. doi:10.1016/j.quascirev.2017.07.005

GRID-Arendal (2013), In State of the Mediterranean Marine and Coastal Environment. 2013. URL: https://www.grida.no/resources/5885

Grinsted, A., Moore, J. C., & Jevrejeva, S. (2004). Application of the cross wavelet transform and wavelet coherence to geophysical time series. Nonlinear Processes in Geophysics, 11, 561-566.

Guo, Q., Li, B., & Kim, J.-K. (2017). Benthic foraminiferal assemblages and bottom water evolution off the Portuguese margin since the Middle Pleistocene. Global and Planetary Change, 150, 94–108. https://doi.org/10.1016/j.gloplacha.2016.11.004

Hall, I. R., & McCave, I. N. (2000). Palaeocurrent reconstruction, sediment and thorium focussing on the Iberian margin over the last 140 ka. Earth and Planetary Science Letters, 178(1–2), 151–164. https://doi.org/10.1016/S0012-821X(00)00068-6

Hanesch, M., Stanjek, H., & Petersen, N. (2006). Thermomagnetic measurements of soil iron minerals: the role of organic carbon. Geophysical Journal International, 165(1), 53-61. doi:10.1111/j.1365-246X.2006.02933.x

Harrison, R. J., & Feinberg, J. M. (2008). FORCinel: An improved algorithm for calculating first-order reversal curve distributions using locally weighted regression smoothing. Geochemistry, Geophysics, Geosystems, 9(5), n/a-n/a. doi:10.1029/2008gc001987

He, K., & Pan, Y. (2020). Magnetofossil Abundance and Diversity as Paleoenvironmental Proxies: A Case Study From Southwest Iberian Margin Sediments. Geophysical Research Letters, 47(8). doi:10.1029/2020gl087165

Heinrich, H. (1988). Origin and consequences of cyclic ice rafting in the northeast Atlantic Ocean during the past 130,000 years. Quaternary Research, 29(2), 142-152.

Hernández-Molina, F. J., Llave, E., Preu, B., Ercilla, G., Fontan, A., Bruno, M., . . . Arnaiz, A. (2014). Contourite processes associated with the Mediterranean Outflow Water after its exit from the Strait of Gibraltar: Global and conceptual implications. Geology, 42(3), 227-230. doi:10.1130/g35083.1

Hernandez-Molina, F. J., Stow, D. A., Alvarez-Zarikian, C. A., Acton, G., Bahr, A., Balestra, B., . . . Xuan, C. (2014). Paleoceanography. Onset of Mediterranean outflow into the North Atlantic. Science, 344(6189), 1244-1250. doi:10.1126/science.1251306

Hernandez-Molina, F. J., Stow, D. A., Alvarez-Zarikian, C. A., Acton, G., Bahr, A., Balestra, B., et al. (2014). Onset of Mediterranean outflow into the North Atlantic. Science, 344(6189), 1244–1250. https://doi.org/10.1126/science.1251306

Heslop, D., & Roberts, A. P. (2012). A method for unmixing magnetic hysteresis loops. Journal of Geophysical Research: Solid Earth, 117(B3). doi:10.1029/2011jb008859

Heslop, D., Dekkers, M. J., Kruiver, P. P., & van Oorschot, I. H. M. (2002). Analysis of isothermal remanent magnetization acquisition curves using the expectation-maximization algorithm. Geophysical Journal International, 148, 58-64.

Hirt, A. M., Banin, A., & Gehring, B. (1993). Thermal generation of ferromagnetic minerals from iron-enriched smectites. Geophysical Journal International, 115, 1161-1168.

Hodell, D. A., Channell, J. E. T., Curtis, J. H., Romero, O. E., & Röhl, U. (2008). Onset of “Hudson Strait” Heinrich Events in the Eastern North Atlantic at the end of the Middle Pleistocene Transition (~640 ka)? Paleoceanography, 23(PA4218).

Hodell, D. A., Crowhurst, S., Skinner, L., Tzedakis, P. C., Margari, V., Channell, J. E. T., et al. (2013). Response of Iberian Margin sediments to orbital and suborbital forcing over the past 420 ka. Paleoceanography, 28, 185–199. https://doi.org/10.1002/palo.20017

Hodell, D. A., Lourens, L., Crowhurst, S., Konijnendijk, T., Tjallingii, R., Jiménez-Espejo, F., et al. (2015). A reference time scale for Site U1385 (Shackleton Site) on the SW Iberian Margin. Global and Planetary Change, 133, 49–64. https://doi.org/10.1016/j. gloplacha.2015.07.002

Hodell, D., Elderfield, H., Greaves, M., Mccave, I. N., Skinner, L., Thomas, A., . . . JC089 Scientific Party. (2014). JC089 Cruise Report, IODP Site Survey of the Shackleton Sites, SW Iberian Margin. Retrieved from Cambridge:

Hrouda, F. (1982). Magnetic anisotropy of rocks and its application in geology and geophysics. Geophysical Surveys, 5(1), 37–82. https://doi. org/10.1007/BF01450244

Iorga, M. C., & Lozier, M. S. (1999). Signatures of the Mediterranean outflow from a North Atlantic climatology: 1. Salinity and density fields. Journal of Geophysical Research, 104(C11), 25,985–26,009. https://doi.org/10.1029/1999JC900115

Itambi, A. C., von Dobeneck, T., Mulitza, S., Bickert, T., & Heslop, D. (2009). Millennial-scale northwest African droughts related to Heinrich events and Dansgaard-Oeschger cycles: Evidence in marine sediments from offshore Senegal. Paleoceanography, 24(1), n/a-n/a. doi:10.1029/2007pa001570

Ivanovic, R. F., Valdes, P. J., Flecker, R., Gregoire, L. J., & Gutjahr, M. (2013). The parameterisation of Mediterranean–Atlantic water exchange in the Hadley Centre model HadCM3, and its effect on modelled North Atlantic climate. Ocean Modelling, 62, 11–16. https:// doi.org/10.1016/j.ocemod.2012.11.002

Ivanovic, R. F., Valdes, P. J., Gregoire, L., Flecker, R., & Gutjahr, M. (2013). Sensitivity of modern climate to the presence, strength and salinity of Mediterranean-Atlantic exchange in a global general circulation model. Climate Dynamics, 42(3–4), 859–877. https://doi.org/ 10.1007/s00382-013-1680-5

Jackson, M., & Solheid, P. (2010). On the quantitative analysis and evaluation of magnetic hysteresis data. Geochemistry, Geophysics, Geosystems, 11(4), n/a-n/a. doi:10.1029/2009gc002932

Jordanova, D., & Jordanova, N. (2016). Thermomagnetic Behavior of Magnetic Susceptibility—Heating Rate and Sample Size Effects. Frontiers in Earth Science, 3. doi:10.3389/feart.2015.00090

Joseph, L. H., Rea, D. K., & Van der Pluijm, B. A. (1998). Use of grain size and magnetic fabric analyses to distinguish among depositional environments. Paleoceanography, 13(5), 491–501. https://doi.org/10.1029/98pa01939

Kaboth-Bahr, S., Bahr, A., Zeeden, C., Toucanne, S., Eynaud, F., Jiménez-Espejo, F., et al. (2018). Monsoonal forcing of European ice-sheet dynamics during the Late Quaternary. Geophysical Research Letters, 45, 7066–7074. https://doi.org/10.1029/2018gl078751

Kaboth, S., de Boer, B., Bahr, A., Zeeden, C., & Lourens, L. J. (2017). Mediterranean Outflow Water dynamics during the past ~570 kyr: Regional and global implications. Paleoceanography, 32, 634–647. https://doi.org/10.1002/2016PA003063

Khelifi, N., Sarnthein, M., Andersen, N., Blanz, T., Frank, M., Garbe-Schonberg, D., . . . Weinelt, M. (2009). A major and long-term Pliocene intensification of the Mediterranean outflow, 3.5-3.3 Ma ago. Geology, 37(9), 811-814. doi:10.1130/g30058a.1

King, J. W., & Channell, J. E. T. (1991). Sedimentary Magnetism, Environmental Magnetism, And Magnetostratigraphy U.S. National Report to the International Union of Geodesy and Geophysics (Vol. 29, pp. 358-370). Washington D.C.: AGU.

King, R. F., & Rees, A. I. (1962). The measurement of the anisotropy of magnetic susceptibility of rocks by the torque method. Journal of Geophysical Research, 67(4), 1565–1572. https://doi.org/10.1029/JZ067i004p01565

Kissel, C. (2005). Magnetic signature of rapid climatic variations in glacial North Atlantic, a review. Comptes Rendus Geoscience, 337(10-11), 908-918.

Kissel, C., Laj, C., Mulder, T., Wandres, C., & Cremer, M. (2009). The magnetic fraction: A tracer of deep water circulation in the North Atlantic. Earth and Planetary Science Letters, 288(3-4), 444-454. doi:10.1016/j.epsl.2009.10.005

Konert, M., & Vandenberghe, J. (1997). Comparison of laser grain size analysis with pipette and sieve analysis- a solution for the underestimation of the clay fraction. Sedimentology, 44, 523-535.

Kruiver, P. P., Dekkers, M. J., & Heslop, D. (2001). Quantification of magnetic coercivity components by the analysis of acquisition curves of isothermal remanent magnetisation. Earth and Planetary Science Letters, 189, 269-276.

Kutzbach, J. E., Chen, G., Cheng, H., Edwards, R. L., & Liu, Z. (2014). Potential role of winter rainfall in explaining increased moisture in the Mediterranean and Middle East during periods of maximum orbitally-forced insolation seasonality. Climate Dynamics, 42(3–4), 1079–1095. https://doi.org/10.1007/s00382-013-1692-1

Lanci, L., Pares, J. M., Channell, J. E. T., & Kent, D. V. (2004). Miocene magnetostratigraphy from Equatorial Pacific sediments (ODP Site 1218, Leg 199). Earth and Planetary Science Letters, 226(1–2), 207–224. https://doi.org/10.1016/j.epsl.2004.07.025

Larrasoaña, J. C., Roberts, A. P., Rohling, E. J., Winklhofer, M., & Wehausen, R. (2003). Three million years of monsoon variability over the northern Sahara. Climate Dynamics, 21(7–8), 689–698. https://doi.org/10.1007/s00382-003-0355-z

Laskar, J., Robutel, P., Joutel, F., Gastineau, M., Correia, A. C. M., & Levrard, B. (2004). A long-term numerical solution for the insolation quantities of the Earth. Astronomy & Astrophysics, 428(1), 261–285. https://doi.org/10.1051/0004-6361:20041335

Lisiecki, L. E., & Raymo, M. E. (2005). A Pliocene-Pleistocene stack of 57 globally distributed benthic $\delta^{18}O$ records. Paleoceanography, 20(1), n/a-n/a. doi:10.1029/2004pa001071

Liu, Q., Roberts, A. P., Larrasoaña, J. C., Banerjee, S. K., Guyodo, Y., Tauxe, L., & Oldfield, F. (2012). Environmental magnetism: Principles and applications. Reviews of Geophysics, 50(4). doi:10.1029/2012rg000393

Liu, Q., Roberts, A. P., Torrent, J., Horng, C.-S., & Larrasoaña, J. C. (2007). What do the HIRM andS-ratio really measure in environmental magnetism? Geochemistry, Geophysics, Geosystems, 8(9), n/a-n/a. doi:10.1029/2007gc001717

Llave, E., Schönfeld, J., Hernández-Molina, F. J., Mulder, T., Somoza, L., Díaz del Río, V., & Sánchez-Almazo, I. (2006). High-resolution stratigraphy of the Mediterranean outflow contourite system in the Gulf of Cadiz during the late Pleistocene: The impact of Heinrich events. Marine Geology, 227(3–4), 241–262. https://doi.org/10.1016/j.margeo.2005.11.015

Lourens, L. J., Antonarakou, A., Hilgen, F., Van Hoof, A., Vergnaud-Grazzini, C., & Zachariasse, W. (1996). Evaluation of the Plio-Pleistocene astronomical timescale. Paleoceanography, 11(4), 391-413.

Lowrie, W., & Fichtner, A. (2020). Fundamentals of geophysics: Cambridge university press.

Lozier, M. S., & Stewart, N. M. (2008). On the temporally varying northward penetration of Mediterranean Overflow Water and eastward penetration of Labrador Sea Water. Journal of Physical Oceanography, 38(9), 2097–2103. https://doi.org/10.1175/2008jpo3908.1

Magill, C. R., Ausin, B., Wenk, P., McIntyre, C., Skinner, L., Martinez-Garcia, A., et al. (2018). Transient hydrodynamic effects influence organic carbon signatures in marine sediments. Nature Communications, 9(1), 4690. https://doi.org/10.1038/s41467-018-06973-w

Martrat, B., Grimalt, J. O., Shackleton, N. J., Abreu, L. d., Hutterli, M. A., & Stocker, T. F. (2007). Four climate cycles of recurring deep and surface water destabilizations on the Iberian margin. Science, 317(5837), 502–507. https://doi.org/10.1126/science.1139994

Maslin, M. A., Li, X. S., Loutre, M. F., & Berger, A. (1998). The Contribution of Orbital Forcing to the Progressive Intensification of Northern Hemisphere Glaciation. Quaternary Science Reviews, 17(4-5), 411-426. doi:10.1016/s0277-3791(97)00047-4

Maxbauer, D. P., Feinberg, J. M., & Fox, D. L. (2016). MAX UnMix: A web application for unmixing magnetic coercivity distributions. Computers & Geosciences, 95, 140-145.

McCave, I. N. (1985). Sedimentology and stratigraphy of box cores from the hebble site on the nova scotian continental rise. Marine Geology, 66, 59 - 89.

McCave, I. N., & Hall, I. R. (2006). Size sorting in marine muds: Processes, pitfalls, and prospects for paleoflow-speed proxies. Geochemistry, Geophysics, Geosystems, 7(10), n/a-n/a. doi:10.1029/2006gc001284

McCave, I. N., Hall, I. R., & Bianchi, G. G. (2006). Laser vs. settling velocity differences in silt grainsize measurements: estimation of palaeocurrent vigour. Sedimentology, 53(4), 919-928. doi:10.1111/j.1365-3091.2006.00783.x

McCave, I. N., Manighetti, B., & Robinson, S. G. (1995). Sortable silt and fine sediment size/composition slicing: Parameters for palaeocurrent speed and palaeoceanography. Paleoceanography, 10(3), 593–610. https://doi.org/10.1029/94PA03039

McCave, I. N., Thornalley, D. J. R., & Hall, I. R. (2017). Relation of sortable silt grain-size to deep-sea current speeds: Calibration of the 'Mud Current Meter'. Deep Sea Research Part I: Oceanographic Research Papers, 127, 1–12. https://doi.org/10.1016/j.dsr.2017.07.003

Millot, C. (2009). Another description of the Mediterranean Sea outflow. Progress in Oceanography, 82(2), 101–124. https://doi.org/10.1016/ j.pocean.2009.04.016

Moreno, E., Thouveny, N., Delanghe, D., McCave, I. N., & Shackleton, N. J. (2002). Climatic and oceanographic changes in the Northeast Atlantic reflected by magnetic properties of sediments deposited on the Portuguese Margin during the last 340 ka. Earth and Planetary Science Letters, 202, 465-480.

Novak, B., Housen, B., Kitamura, Y., Kanamatsu, T., & Kawamura, K. (2014). Magnetic fabric analyses as a method for determining sediment transport and deposition in deep sea sediments. Marine Geology, 356, 19–30. https://doi.org/10.1016/j.margeo.2013.12.001

O'Neill-Baringer, M., & Price, J. F. (1999). A review of the physical oceanography of the Mediterranean outflow. Marine Geology, 155(1–2), 63–82. https://doi.org/10.1016/S0025-3227(98)00141-8

Oda, H., & Xuan, C. (2014). Deconvolution of continuous paleomagnetic data from pass-through magnetometer: A new algorithm to restore geomagnetic and environmental information based on realistic optimization. Geochemistry, Geophysics, Geosystems, 15(10), 3907-3924. doi:10.1002/2014gc005513

Orland, I. J., He, F., Bar-Matthews, M., Chen, G., Ayalon, A., & Kutzbach, J. E. (2019). Resolving seasonal rainfall changes in the Middle East during the last interglacial period. Proc Natl Acad Sci U S A, 116(50), 24985-24990. doi:10.1073/pnas.1903139116

Park, M. E., Cho, H., Son, M., & Sohn, Y. K. (2013). Depositional processes, paleoflow patterns, and evolution of a Miocene gravelly fan-delta system in SE Korea constrained by anisotropy of magnetic susceptibility analysis of interbedded mudrocks. Marine and Petroleum Geology, 48, 206–223. https://doi.org/10.1016/j.marpetgeo.2013.08.015

Paterson, G. A., & Heslop, D. (2015). New methods for unmixing sediment grain size data. Geochem Geophys Geosyst, 16. doi:10.1002/

Paterson, G. A., Zhao, X., Jackson, M., & Heslop, D. (2018). Measuring, Processing, and Analyzing Hysteresis Data. Geochemistry, Geophysics, Geosystems, 19(7), 1925-1945. doi:10.1029/2018gc007620

Peters, C., & Dekkers, M. J. (2003). Selected room temperature magnetic parameters as a function of mineralogy, concentration and grain size. Physics and Chemistry of the Earth, Parts A/B/C, 28(16-19), 659-667. doi:10.1016/s1474-7065(03)00120-7

Pike, C. R., Roberts, A. P., & Verosub, K. L. (1999). Characterizing interactions in fine magnetic particle systems using first order reversal curves. Journal of Applied Physics, 85(9), 6660-6667. doi:10.1063/1.370176

Relvas, P., Barton, E. D., Dubert, J., Oliveira, P. B., Peliz, Á., da Silva, J. C. B., & Santos, A. M. P. (2007). Physical oceanography of the western Iberia ecosystem: Latest views and challenges. Progress in Oceanography, 74(2–3), 149–173. https://doi.org/10.1016/j. pocean.2007.04.021

Richter, T. O., van der Gaast, S., Koster, B., Vaars, A., Gieles, R., de Stigter, H. C., . . . van Weering, T. C. E. (2006). The Avaatech XRF Core Scanner: technical description and applications to NE

Atlantic sediments. In G. Rothwell (Ed.), New Techniques in Sediment Core Analysis (Vol. 267, pp. 39-50). London: The Geological Society of London.

Roberts, A. P. (1995). Magnetic properties of sedimentary greigite (Fe3S4). Earth and Planetary Science Letters, 134, 227-236.

Roberts, A. P. (2015). Magnetic mineral diagenesis. Earth-Science Reviews, 151, 1-47. doi:10.1016/j.earscirev.2015.09.010

Roberts, A. P. (2015). Magnetic mineral diagenesis. Earth-Science Reviews, 151, 1-47. doi:10.1016/j.earscirev.2015.09.010

Roberts, A. P., Heslop, D., Zhao, X., & Pike, C. R. (2014). Understanding fine magnetic particle systems through use of first-order reversal curve diagrams. Reviews of Geophysics, 52, 557-602. doi:10.1002/

Roberts, A. P., Pike, C. R., & Verosub, K. L. (2000). First-order reversal curve diagrams: A new tool for characterizing the magnetic properties of natural samples. Journal of Geophysical Research: Solid Earth, 105(B12), 28461-28475. doi:10.1029/2000jb900326

Roberts, A. P., Tauxe, L., Heslop, D., Zhao, X., & Jiang, Z. (2018). A critical appraisal of the “Day” diagram. Journal of Geophysical Research: Solid Earth, 123(4), 2618-2644.

Roberts, A. P., Zhao, X., Heslop, D., Abrajevitch, A., Chen, Y.-H., Hu, P., . . . Pillans, B. J. (2020). Hematite (α-Fe 2 O 3) quantification in sedimentary magnetism: limitations of existing proxies and ways forward. Geoscience Letters, 7(1), 1-11.

Robertson, D. J., & France, D. E. (1994). Discrimination of remanence-carrying minerals in mixtures, using isothermal remanent magnetisation acquisition curves. Physics of the Earth and Planetary Interiors, 82, 223-234.

Rogerson, M., Colmenero-Hidalgo, E., Levine, R. C., Rohling, E. J., Voelker, A. H. L., Bigg, G. R., et al. (2010). Enhanced Mediterranean-Atlantic exchange during Atlantic freshening phases. Geochemistry, Geophysics, Geosystems, 11, Q08013. https://doi.org/ 10.1029/2009gc002931

Rogerson, M., Rohling, E. J., Bigg, G. R., & Ramirez, J. (2012). Paleoceanography of the Atlantic-Mediterranean exchange: Overview and first quantitative assessment of climatic forcing. Reviews of Geophysics, 50, RG2003. https://doi.org/10.1029/2011RG000376

Rogerson, M., Rohling, E. J., Weaver, P. P. E., & Murray, J. W. (2005). Glacial to interglacial changes in the settling depth of the Mediterranean outflow plume. Paleoceanography, 20, PA3007. https://doi.org/10.1029/2004PA001106

Rohling, E. J., Foster G. L., Grant K. M., Marino G., Roberts A. P., Tamisiea M. E., & Williams, F. (2014). Sea-level and deep-sea temperature variability over the past 5.3 million years. Nature, 508(7497), 477–482. https://doi.org/10.1038/nature13230

Rohling, E. J., Marino, G., & Grant, K. M. (2015). Mediterranean climate and oceanography, and the periodic development of anoxic events (sapropels). Earth-Science Reviews, 143, 62–97. https://doi.org/10.1016/j.earscirev.2015.01.008

Rossignol-Strick, M. (1985). Mediterranean Quaternary sapropels, an immediate response of the African monsoon to variation of insolation. Palaeogeography, Palaeoclimatology, Palaeoecology, 49(3-4), 237-263.

Rothwell, G., Hoogakker, B. A. A., Thomson, J., Croudace, I. W., & Frenz, M. (2006). Turbidite emplacement on the southern Balearic Abyssal Plain (western Mediterranean Sea) during Marine Isotope Stages 1–3: An application of ITRAX XRF scanning of sediment cores to lithostratigraphic analysis. In G. Rothwell (Ed.), New techniques in sediment core analysis (Vol. 267, pp. 79–98). London: Geological Society of London.

Sánchez Goñi, M. F., Eynaud, F., Turon, J. L., & Shackleton, N. J. (1999). High resolution palynological record off the Iberian margin: direct land-sea correlation for the Last Interglacial complex. Earth and Planetary Science Letters, 171(1), 123-137. doi:https://doi.org/10.1016/S0012-821X(99)00141-7

Shackleton, N. J., Fairbanks, R. G., Chiu, T.-c., & Parrenin, F. (2004). Absolute calibration of the Greenland time scale: implications for Antarctic time scales and for Δ14C. Quaternary Science Reviews, 23(14), 1513-1522. doi:https://doi.org/10.1016/j.quascirev.2004.03.006

Shackleton, N. J., Hall, M. A., & Vincent, E. (2000). Phase relationships between millennial-scale events 64,000-24,000 years ago. Paleoceanography, 15(6), 565-569. doi:10.1029/2000pa000513

Sluijs, A., Schouten, S., Donders, T. H., Schoon, P. L., Röhl, U., Reichart, G.-J., . . . Brinkhuis, H. (2009). Warm and wet conditions in the Arctic region during Eocene Thermal Maximum 2. Nature Geoscience, 2(11), 777-780. doi:10.1038/ngeo668

Spooner, P. T., Thornalley, D. J. R., & Ellis, P. (2018). Grain Size Constraints on Glacial Circulation in the Southwest Atlantic. Paleoceanography and Paleoclimatology, 33(1), 21-30. doi:10.1002/2017pa003232

Stommel, H., Bryden, H. L., & Mangelsdorf, P. (1973). Does some of the Mediterranean outflow come from great depth? Pure and Applied Geophysics, 105, 879–889. https://doi.org/10.1007/bf00875837

Stoner, J. S., Channell, J. E., & Hillaire-Marcel, C. (1996). The magnetic signature of rapidly deposited detrital layers from the deep Labrador Sea: Relationship to North Atlantic Heinrich layers. Paleoceanography, 11(3), 309-325.

Stow, D. A., Faugères, J. C., Howe, J. A., Pudsey, C. J., & Viana, A. R. (2002). Bottom currents, contourites and deep-sea sediment drifts: current state-of-the-art. In D. A. Stow, J. C. Faugères, J. A. Howe, C. J. Pudsey, & A. R. Viana (Eds.), Deep-Water Contourite Systems: Modern Drifts and Ancient Series, Seismic and Sedimentary Characteristics (Vol. 22, pp. 7-20). London: Geological Society.

Stow, D. A., Hunter, S., Wilkinson, D. and Hernández-Molina, F.J. (2008). The nature of contourite deposition. In Rebesco, M. and Camerlenghi, A. (Eds.) Developments in Sedimentology (Vol. 60, pp 1-663). Oxford: Elsevier.

Swingedouw, D., Colin, C., Eynaud, F., Ayache, M., & Zaragosi, S. (2019). Impact of freshwater release in the Mediterranean Sea on the North Atlantic climate. Climate Dynamics, 53(7–8), 3893–3915. https://doi.org/10.1007/s00382-019-04758-5

Taira, A. (1989). Magnetic fabrics and depositional processes. In A. Taira, & F. Masuda (Eds.), Sedimentary facies in the active plate margin (pp. 43–47). Tokyo: Terra Scientific Publishing Company.

Tauxe, L. (2010). Essentials of palaeomagnetism. Berkeley, California: University of California Press.

Tauxe, L., Banerjee, S., Butler, R., & Van der Voo, R. (2018). Essentials of Paleomagnetism: 5th Web Edition: https://earthref. org/MagIC/books/Tauxe: Essentials.

Tauxe, L., Gee, J. S., & Staudigel, H. (1998). Flow directions in dikes from anisotropy of magnetic susceptibility data: The bootstrap way. Journal of Geophysical Research, 103(B8), 17,775–17,790. https://doi.org/10.1029/98JB01077

Tauxe, L., LaBrecque, J. L., Dodson, R., & Fuller, M. (1983). U-channels - a new technique for paleomagnetic analysis of hydraulic piston cores. Eos, Transactions, American Geophysical Union, 64, 219.

Thomson, J., Nixon, S., Summerhayes, C. P., Schönfeld, J., Zahn, R., & Grootes, P. (1999). Implications for sedimentation changes on the Iberian margin over the last two glacial/interglacial transitions from (230Thexcess)0 systematics. Earth and Planetary Science Letters, 165(3–4), 255–270. https://doi.org/10.1016/S0012-821X(98)00265-9

Thornalley, D. J. R., Blaschek, M., Davies, F. J., Praetorius, S., Oppo, D. W., McManus, J. F., . . . McCave, I. N. (2013). Long-term variations in Iceland–Scotland overflow strength during the Holocene. Climate of the Past, 9(5), 2073-2084. doi:10.5194/cp-9-2073-2013

Thouveny, N., Moreno, E., Delanghe, D., Candon, L., Lancelot, Y., & Shackleton, N. J. (2000). Rock magnetic detection of distal ice-rafted debries: clue for the identification of Heinrich layers on the Portuguese margin. Earth and Planetary Science Letters, 180(1-2), 61-75. doi:10.1016/s0012-821x(00)00155-2

Tjallingii, R., Röhl, U., Kölling, M., & Bickert, T. (2007). Influence of the water content on X-ray fluorescence core-scanning measurements in soft marine sediments. Geochem Geophys Geosyst, 8(Q02004). doi:10.1029/2006GC001393

Toucanne, S., Jouet, G., Ducassou, E., Bassetti, M.-A., Dennielou, B., Angue Minto'o, C. M., et al. (2012). A 130,000-year record of Levantine Intermediate Water flow variability in the Corsica Trough, western Mediterranean Sea. Quaternary Science Reviews, 33, 55–73. https://doi.org/10.1016/j.quascirev.2011.11.020

Trauth, M. H., Larrasoaña, J. C., & Mudelsee, M. (2009). Trends, rhythms and events in Plio-Pleistocene African climate. Quaternary Science Reviews, 28(5–6), 399–411. https://doi.org/10.1016/j.quascirev.20

Tsimplis, M. N., & Bryden, H. L. (2000). Estimation of the transports through the Strait of Gibraltar. Deep Sea Research Part I: Oceanographic Research Papers, 47(12), 2219–2242. https://doi.org/10.1016/S0967-0637(00)00024-8

Tzedakis, P. C., Margari, V., & Hodell, D. A. (2015). Coupled ocean–land millennial-scale changes 1.26 million years ago, recorded at Site U1385 off Portugal. Global and Planetary Change, 135, 83–88. https://doi.org/10.1016/j.gloplacha.2015.10.008

Tzedakis, P. C., Pälike, H., Roucoux, K. H., & de Abreu, L. (2009). Atmospheric methane, southern European vegetation and low-mid latitude links on orbital and millennial timescales. Earth and Planetary Science Letters, 277(3–4), 307–317. https://doi.org/10.1016/j. epsl.2008.10.027

Voelker, A., & de Abreu, L. (2011). A Review of Abrupt Climate Change Events in the Northeastern Atlantic Ocean (Iberian margin): Latitudinal, Longitudinal and Vertical Gradients Abrupt Climate Change: Mechanisms, Patterns, and Impacts (Vol. Geophysical Monograph Series 193, pp. 15-37). Washington D.C.: American Geophysical Union.

Voelker, A., Lebreiro, S., Schonfeld, J., Cacho, I., Erlenkeuser, H., & Abrantes, F. (2006). Mediterranean outflow strengthening during northern hemisphere coolings: A salt source for the glacial Atlantic? Earth and Planetary Science Letters, 245(1–2), 39–55. https://doi. org/10.1016/j.epsl.2006.03.014

Weltje, G. J., & Tjallingii, R. (2008). Calibration of XRF core scanners for quantitative geochemical logging of sediment cores: Theory and application. Earth and Planetary Science Letters, 274(3–4), 423–438. https://doi.org/10.1016/j.epsl.2008.07.054

Wu, L., Wilson, D. J., Wang, R., Yin, X., Chen, Z., Xiao, W., & Huang, M. (2020). Evaluating Zr/Rb ratio from XRF scanning as an indicator of grain-size variations of glaciomarine sediments in the Southern Ocean. Geochemistry, Geophysics, Geosystems, e2020GC009350.

Xu, R. (2000). Particle size and shape analysis using laser scattering and image analysis. Revista Latinoamericana de Metalurgia y Materiales, 20(2), 80-84.

Xuan, C., & Channell, J. E. T. (2009). UPmag: MATLAB software for viewing and processing u channel or other pass-through paleomagnetic data. Geochemistry, Geophysics, Geosystems, 10(10), n/a-n/a. doi:10.1029/2009gc002584

Xuan, C., & Oda, H. (2015). UDECON: deconvolution optimization software for restoring high-resolution records from pass-through paleomagnetic measurements. Earth, Planets and Space, 67(1). doi:10.1186/s40623-015-0332-x

Xuan, C., Channell, J. E. T., Polyak, L., & Darby, D. A. (2012). Paleomagnetism of Quaternary sediments from Lomonosov Ridge and Yermak Plateau: implications for age models in the Arctic Ocean. Quaternary Science Reviews, 32, 48-63. doi:10.1016/j.quascirev.2011.11.015

Yokokawa, M., & Franz, S.-O. (2002). Changes in grain size and magnetic fabric at Blake–Bahama Outer Ridge during the late Pleistocene (marine isotope stages 8–10). Marine Geology, 189(1-2), 123–144. https://doi.org/10.1016/s0025-3227(02)00326-2

Zavattarelli, M., & Mellor, G.L. (1994). A Numerical Study of the Mediterranean Sea Circulation. Journal of Physical Oceanography, 25, 1384-1414.

Ziegler, M., Jilbert, T., de Lange, G. J., Lourens, L. J., & Reichart, G.-J. (2008). Bromine counts from XRF scanning as an estimate of the marine organic carbon content of sediment cores. Geochemistry, Geophysics, Geosystems, 9(5), n/a-n/a. doi:10.1029/2007gc001932